

TECHNICAL UNIVERSITY OF CRETE

DEPT. OF ELECTRONICS AND COMPUTER ENGINEERING



Development of a fast, high throughput hyper spectral hysteroscope

Technical and Clinical Evaluation

Nikolaos Georgiou

Master Thesis

Supervising committee: Constantinos Balas (Supervisor),
Zervakis Michalis
Potamianos Alexandros

Chania, 2010

Table of Contents

Acknowledgements	3
Abstract	5
Summary	6
Chapter 1	8
<i>Endoscopy</i>	8
<i>Types of Endoscopy</i>	9
<i>History of Endoscopy</i>	10
Endoscopy in Ancient times	10
Light guides	10
Endoscopy with telescopes	12
Upper gastrointestinal endoscopy	13
Documentation	14
The latter half of the 20 th century and the revolution in endoscopic procedures	15
Illumination	16
Television	16
<i>Hysteroscopy</i>	17
Benefits of Hysteroscopy	18
Chapter 2	20
<i>Fundamentals of Tissue Optics</i>	20
<i>Optical properties of tissue</i>	20
Absorption	21
Scattering	22
Optical properties of various tissue types	24
<i>Modeling of photon transport in tissue</i>	28
The Radiative Transfer Equation	29
Deterministic models	30
Numerical solutions	32
Stochastic Models	34
Chapter 3	37
Tunable Filters	37

Electronically tunable filter examples	38
<i>Liquid crystal tunable filters (LCTFs)</i>	38
Holographically – formed, polymer dispersed liquid crystal (H-PDLC)	39
<i>Acousto – optical tunable filters (AOTFs)</i>	40
<i>Interferometers</i>	47
<i>Linear Variable Filters (LVFs)</i>	51
Tunable filters commercial applications	52
<i>VariSpec</i>	52
<i>Gooch & Housego</i>	53
<i>SpectralView^R</i>	54
Chapter 4	55
<i>Introduction to image enhanced endoscopy</i>	55
<i>Novel diagnostic Advances in Endoscopy</i>	55
Chromoendoscopy	56
Auto fluorescence Imaging (AFI) Endoscopy	56
Narrow band Imaging (NBI) Endoscopy	59
Fujinon intelligent color enhancement (FICE) and i-Scan endoscopic systems	60
Confocal laser endomicroscopy (CLE)	62
<i>Clinical Applications</i>	63
Early cancer of the colon	64
Early diagnosis and detection of Barrett’s esophagus	66
Human tongue	67
Lung cancer –Bronchoscopy	67
Intestinal cancer	69
Cervical cancer –Colposcopy	69
Chapter 5	71
<i>Material and Methods</i>	71
The use of LVF	71
Electronics	74
Hardware – Parts	74
Hardware – Design	81

Firmware	83
PC software	83
Chapter 6	87
<i>Characterization and Clinical Validation</i>	87
Spectral bands and calibration	87
Clinical Evaluation	93
<i>Results – Future work</i>	106
References	108
Appendix A	115
Appendix B	133

Acknowledgements

This Master Thesis will not have been completed if I wasn't the presence of many people to support me all the way.

Firstly, I am very grateful for the cooperation and interest of my supervisor, Professor Constantinos Balas, whose guidance was invaluable. His unique way of thought and his deep knowledge in the area of spectral imaging and medical device design have guided me throughout my Master.

I would also like to thank my fellow students in the Optoelectronics Laboratory of Electronics and Computer Engineering who have always been there for me.

Thanks also to Mr. Harris Triadafilidis for his advice on medical specification PCB design and to Mr. Dimitris Pelekoudas for his programming wisdom.

Finally I am most indebted to my friends who have supported me and encouraged me in times of crisis.

To my loving parents,

Vasilis and Argyroula.

Abstract

Endoscopy has evolved greatly through the last 25 years, but still there many areas of improvement, areas yet unexplored. Combining spectral imagining and endoscopy, novel technologies have provided powerful tools to the hands of the physicians. Unfortunately, these technologies are sub optimal for use in thin endoscopes as the hysteroscope. In this thesis we present the development of a new fast, high-throughput, hyper-spectral hysteroscope endoscopic system, its technical evaluation and an initial feasibility study in clinical environment.

Summary

After several decades of technology and application development, endoscopy has been established as an indispensable diagnostic tool to a variety of internal medicine fields. However it has been widely recognized that there is significant room for improvement mainly through the merging of endoscopy with novel and advanced optical imaging methods and technologies. These include confocal imaging (CI), optical coherence tomography (OCT) and spectral imaging (SI). CI and OCT with or without contrast enhancing agents, provide histological information *in vivo* for the very small tissue area. Spectral imaging provide in principle information for a much larger tissue area which is essential in the clinical practice. Integrated to endoscopy, this imaging modality provides enhanced visualization of features of diagnostic importance such as neovascularization. It holds also the promise to provide spectral signatures of tissue lesions for enabling their *in vivo* identification and spectral mapping and grading for guiding treatment.

There has been a considerable effort towards the integration of general purpose tunable filter technologies for enabling endoscopic spectral imaging. These include trivial 3-discrete filter arrangements known as NBI, LCTFs AOTFs and Michelson interferometers (look for refs). Although the last three approaches can provide complete spectrum, they suffer from several limitations, which make them suboptimal solutions for endoscopy.

Particularly, LCTFs are polarization dependent which determines their poor light throughput at approximately 30% (look for ref). AOTFs produce blurry images due to second order harmonics from the acoustic driver (need ref). The operating wavelength range of both AOTFs and LCTFs is limited to either the visible or to the NIR spectral range, requiring the interchange of different modules if one wants to cover the entire spectrum sensitivity range of the silicon based imaging sensor (CCD and CMOS). Additionally, the FW/HM of these tunable filters varies significantly together with the light throughput across the operational wavelength range which makes their calibration problematic.

Interferometric approaches do not provide real time imaging, something essential for endoscopic aiming, and as such are not suitable for endoscopic applications. For facilitating aiming and target tissue, selection multiple camera solutions have been adopted including both color and black and white cameras. However this results to bulky imaging head modules which are clearly impractical for endoscopy. The above mentioning shortcomings of the existing general purpose tunable light filter technologies become for profound in fields where thin endoscopes are employed. In that case, the light filtering and the combined poor throughput of both tunable filters and thin endoscope, set very high power requirements for the light source, or,

alternatively requirements for intensified sensors. In the former case however, the power requirements are often exceeding the damage threshold of the optical components due to overheating, while the use of intensified CCDs or EMCCDs is in several cases unacceptable due to their considerable weight and volume.

The aforementioned technological deficiencies comprise a barrier for expanding spectral imaging and analysis to a number of medical specialties. Referring particularly to hysteroscopy employing a thin tip size endoscope, imaging spectroscopy would provide a valuable tool for assisting the diagnosis of endometrial neoplasias and cancers for intensifying tissue abnormalities that would be causal factors for infertility. But, to best of our knowledge, spectral analysis of the endometrium tissue has not reported so far.

In this thesis we report a multimodal spectral imaging endoscopic systems (SIES) capable of acquiring and real time displaying both color and spectral images. From the acquired spectral images a full spectrum can be calculated for every image pixel, spanning both visible and NIR spectral ranges. The developed system has been used for performing spectral analysis and spectral mapping of the endometrium and first clinical findings are presented and discussed.

Chapter 1

Endoscopy

Endoscopy allows physicians to peer through the body's passageways. Endoscopy is the examination and inspection of the interior of body organs, joints or cavities through an endoscope. An endoscope is a device that uses fiber optics and powerful lens systems to provide lighting and visualization of the interior of a joint. The portion of the endoscope inserted into the body may be rigid or flexible, depending upon the medical procedure.

An endoscope uses two fiber optic lines. A "light fiber" carries light into the body cavity and an "image fiber" carries the image of the body cavity back to the physician's viewing lens. There is also a separate port to allow for administration of drugs, suction, and irrigation. This port may also be used to introduce small folding instruments such as forceps, scissors, brushes, snares and baskets for tissue excision (removal), sampling, or other diagnostic and therapeutic work. Endoscopes may be used in conjunction with a camera or video recorder to document images of the inside of the joint or chronicle an endoscopic procedure. New endoscopes have digital capabilities for manipulating and enhancing the video images.

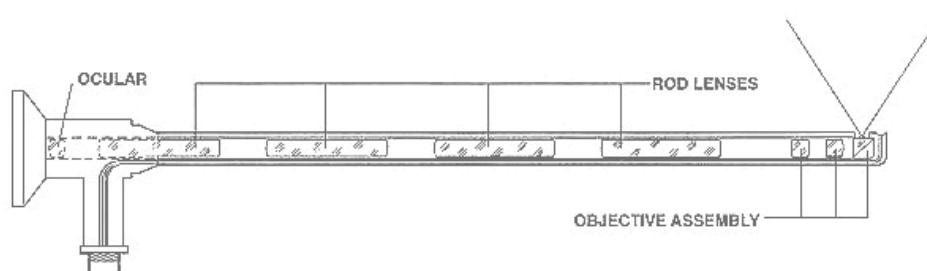


Figure 1. This figure shows a rigid endoscope used for arthroscopy. The "image fiber" leads from the ocular (eye piece) to the inserted end of the scope. The "light fiber" is below and leads from the light source to the working end of the endoscope.

Endoscopy can be used to diagnose various conditions by close examination of internal organ and body structures. Endoscopy can also guide therapy and repair, such as the removal of torn cartilage from the bearing surfaces of a joint. Biopsy (tissue sampling for pathologic testing) may also be performed under endoscopic guidance. Local or general anesthetic may be used during endoscopy, depending upon the type of procedure being performed.

Internal abnormalities revealed through endoscopy include: abscesses, biliary (liver) cirrhosis, bleeding, bronchitis, cancer, cysts, degenerative disease, gallbladder stones, hernia, inflammation, metastatic cancer, polyps, tumors, ulcers, and other diseases and conditions.

Endoscopy is a minimally invasive procedure and carries with it certain minor risks depending upon the type of procedure being performed. However, these risks are typically far outweighed by the diagnostic and therapeutic potential of the procedure.

Prior to the widespread use of endoscopy and diagnostic imaging, most internal conditions could only be diagnosed or treated with open surgery. Until the last several decades, exploratory surgery was routinely performed only when a patient was critically ill and the source of illness was not known. For example, in certain dire cases, the patient's thorax or abdomen were surgically opened and examined to try to determine the source of illness.

Endoscopy can often be done on an outpatient basis. "Outpatient" means that the procedure does not require hospital admission and acute care and observation and may be performed outside the premises of a hospital. Outpatient procedures performed at hospitals or ambulatory centers allow the patient to go home or return to work within a short while after their procedure.

Types of Endoscopy

Fiber optic endoscopes now have widespread use in medicine and guide a myriad of diagnostic and therapeutic procedures including:

- **Arthroscopy:** examination of joints for diagnosis and treatment (arthroscopic surgery)
- **Bronchoscopy:** examination of the trachea and lung's bronchial trees to reveal abscesses, bronchitis, carcinoma, tumors, tuberculosis, alveolitis, infection, inflammation
- **Colonoscopy:** examination of the inside of the colon and large intestine to detect polyps, tumors, ulceration, inflammation, colitis diverticula, Crohn's disease, and discovery and removal of foreign bodies.
- **Colposcopy:** direct visualization of the vagina and cervix to detect cancer, inflammation, and other conditions.
- **Cystoscopy:** examination of the bladder, urethra, urinary tract, uterine orifices, and prostate (men) with insertion of the endoscope through the urethra.
- **ERCP (endoscopic retrograde cholangio-pancreatography)** uses endoscopic guidance to place a catheter for x-ray fluoroscopy with contrast enhancement. This technique is used to examine the liver's biliary tree, the gallbladder, the pancreatic duct and other anatomy to check for stones, other obstructions and disease. X-ray contrast is introduced into these ducts via catheter and fluoroscopic x-ray images are taken to show any abnormality or blockage. If disease is detected, it can sometimes be treated at the same time

or biopsy can be performed to test for cancer or other pathology. ERCP can detect biliary cirrhosis, cancer of the bile ducts, pancreatic cysts, pseudocysts, pancreatic tumors, chronic pancreatitis and other conditions such as gallbladder stones.

- **EGD (Esophagealgastroduodendoscopy):** visual examination of the upper gastro-intestinal (GI) tract. (also referred to as gastroscopy) to reveal hemorrhage, hiatal hernia, inflammation of the esophagus, gastric ulcers.
- **Endoscopic biopsy** is the removal of tissue specimens for pathologic examination and analysis.
- **Gastroscopy:** examination of the lining of the esophagus, stomach, and duodenum. Gastroscopy is often used to diagnose ulcers and other sources of bleeding and to guide biopsy of suspect GI cancers.
- **Laparoscopy:** visualization of the stomach, liver and other abdominal organs including the female reproductive organs, for example, the fallopian tubes.
- **Laryngoscopy:** examination of the larynx (voice box).
- **Proctoscopy, sigmoidoscopy, proctosigmoidoscopy:** examination of the rectum and sigmoid colon.
- **Thoracoscopy:** examination of the pleura (sac that covers the lungs), pleural spaces, mediastinum, and pericardium.

History of Endoscopy

Endoscopy in Ancient times

The first instrument developed to look into deeper cavities was probably the rectal speculum; the earliest mention is found in Hippocrates' treaty on fistula. Galen's *Levicom* refers to the catopter (now in the Naples Museum), an anal speculum. Although open tubes were later designed, several hundred years passed before they could be made useful.

Light guides

The ability to reflect light in deeply located organs was a central problem in designing open tubes to explore or retract tissues and allow the examiner to observe these structures. To address the problem, the light guide system was developed.

Philipp Bozzini, one of the critical workers in this field, was born in 1773 in Mainz, Germany, to an aristocratic Italian family. His father had been forced to flee his native country after coincidentally killing another aristocrat during a duel. In principle, Bozzini's light guide consisted of a housing in which a candle was placed. On one side, he attached open tubes in various sizes and configurations that could be introduced into orifices including the mouth and the rectum. He even devised one with a mirror to examine the vocal cords. On the opposite side of the housing was an

eyepiece. Bozzini was one of the first inventors to insert a reflecting mirror between the visual tract and the candle – light, so that the light would be reflected only toward the organ and not into the examiner's eye (Fig. 2).

Bozzini joined the Austrian army and became a medical officer following the French occupation of this part of Germany. He then moved to Frankfurt to avoid service under the French government. He became interested in mathematics, philosophy, and chemistry as well. He was also a gifted artist, creating an admirable self-portrait, and even designed an early type of airplane.

Bozzini's colleagues were extremely hostile toward his endoscopic ventures and scorned his lectures and publications. In 1807, when he recommended that the first prospective study of this device be performed in military hospitals, he received his first positive response. Gynecologists and ear, nose, and throat specialists expressed particular interest. However, he came under harsh criticism from the influential Dr. Stiff, who held a prominent position at the medical academy in Vienna. The medical faculty dismissed his endoscope as a "new toy," and opinion was sharply divided between the academy and the military hospitals about the usefulness of this so-called toy.

The resistance from his colleagues was so strong that Bozzini was asked to take a state examination on the grounds that he came from another city. When he took it in 1803, he failed the first round. But thanks to his outstanding performance as an army doctor and after political pressure from the Austrian government, he passed a repeat examination and obtained permission to practice.

During an epidemic of typhus, he, as a conscientious doctor, made house calls. He became infected and died from the disease at age 35 after an extremely hard life. He left his widow such poor financial conditions that she was unable to support their three children, who were later adopted. Bozzini's ideas were, however, his vindication. The candle produced heat and sometimes black smoke, but there was a ventilation port on the top of the housing. Despite the limitation of his inventions, he is remembered as the first to illuminate and examine deeply located organs.

A large number of similar experimental tools were developed by Pierre Segalas, who used candles and cone shaped silver cube with a mirror to examine the urinary bladder. Needless to say, his primary selected patients were women.

Some years later, in 1853, Antonin Jean Desormeaux described an open tube for the examination of the genitourinary passages. He used a mixture of alcohol and turpentine as a light source. The beam was reflected into the tube by means of mirrors. Desormeaux was the first to employ condenser lenses to increase the intensity of the illumination.

Subsequently, innumerable open tube systems were developed with a variety of head mirrors to reflect light in various orifices, but they were not well accepted. This, practically speaking, was the end of the open tube system.

Another improvement is attributed to Julius Bruck (1860), a dentist who placed a glowing platinum wire in a water jacket to produce the first distal illumination system. Thus, he created the first galvanic endoscope. This device was one of the predecessors of Edison's filament globe.

In the mid to late 19th century, there were sporadic reports of open tube endoscopy procedures. For example, a famous surgeon named Kussmaul used reflected sunlight to perform removal of a foreign body from the esophagus in 1870. Bevan (1868) extracted foreign bodies and described strictures of the esophagus using the reflected light of a candle. Waldenburg (1870) designed an esophagoscope in which two or three tubes telescoped into each other for easier introduction. For illumination, he used reflected sunlight. Stoerk (1887), who used a right-angled open tube to examine the esophagus, employed the same idea (Fig. 3). Killian (1898), who is known as the father of bronchoscopy, employed an open tube with illumination and a head mirror with topical anesthesia (cocaine). Chevalier Jackson, the father of American bronchoesophagology, was particularly impressed by Killian's work.

Endoscopy with telescopes

There was no question that the examination of a deeply located organ with poor illumination and keyhole vision had great limitations. The breakthrough was achieved by Max Nitze; a general practitioner who realized that in order to be able to introduce an instrument with ease, minimal pain, and relative safety, the examiner had to keep an eye on the diameter of the instrument, which requires a small distal light source. The target area has to be brought up to the eye by some means of well-illuminated magnification. An idea came to Nitze during the process of cleaning a microscope and removing the objective lens, as he was holding the lens in his hand and looking through the window. He saw very sharply, in decreased size, the church located opposite his building. This insight led him to contact instrument makers and opticians (Fig. 4).

Nitze, who was mainly interested in the urinary bladder, developed the first cystoscope (1877). This early version used a platinum wire in a glass jacket with water cooling. The wire was heated and lit by a battery for illumination. Needless to say, this was a very clumsy and cumbersome approach, but it was modified after Edison's invention of the filament globe (1879). It is amazing that Nitze and his team were able to miniaturize the Edison-type globe to a size small enough to fit into the tip of a cystoscope.

Nitze worked with several leading instrument makers and a patent war developed among the various parties. A debate ensued over which took priority--the idea of the inventor or the person who actually built the instrument based on that idea. This debate has yet to be resolved.

Johann von Mikulicz, working with the instrument maker Leiter and using the Nitze telescopic system, which consisted of small lenses placed at certain air intervals, designed a rigid gastroscope that was 650 mm long and 13 mm in diameter, with an angulation at the distal end. It had a globe for illumination at the tip and a channel for air insufflation. The procedure was performed under morphine sedation (Fig. 5). We doubt that many patients underwent this examination because of the unpleasant positioning (head down, Trendelenburg) and the disturbing blind spots associated with this approach (Fig. 6).

Upper gastrointestinal endoscopy

There were several attempts to design a flexible esophagoscope. Kelling (1898) invented a gastroscope in which the lower third could be flexed to 45° and the objective window could be rotated a full 360°. This feature could be useful even today. He employed a miniature electric globe that was built together with prisms. The working tip could be bent in one plane on both sides to 135°. This masterpiece of optics and mechanics was manufactured by Albright before the turn of the century. He made a number of molds from cadaver stomachs before deciding on the final configuration of his instruments. In reading Kelling's original paper, one is amazed at how many details and refinements were included by the pioneers of gastroscopy and the earliest precision instrument makers.

Recognizing the need for flexibility in the field of gastroscopy, Lange and Meltzing (1898) designed a gastrocamera, which was attached to the tip of a rubber tube and used in 15 patients. The exposure time was 1/2-1 sec. The image size displayed on the film was 4 mm. The rigid head, which was only 60-mm long, was divided into three compartments – a film magazine with a small roll, a camera head, and an electric globe. The 5mm wide filmstrip was 400 – 500mm long. After each exposure, it was pulled out from the roll of the film into the rubber shaft. Fifty exposures were made per examination. The rest of the camera consisted of a rubber tube in which the electric wires, air insufflation, and the pulling mechanism of the film were incorporated into the handle [34]. In a modernized version, in principle the same, this blind gastrocamera was "reinvented" 62 years later.

In 1936, Schindler, one of the fathers of gastroscopy, introduced a semi-flexible gastroscope that had been designed by Wolf, an optical physicist. It was 77 cm long and incorporated a rubber finger on the working end for easier introduction. Its diameter was 12 mm at the flexible portion, which comprised the lower third of the

tool, and 8.5 mm in the rigid part. An electric globe was used for illumination. The system provided a lateral view and contained more than 48 lenses. The flexible portion consisted of a spiral with lenses that were kept in place by a special spring covered by two rubber tubes; between these interspaces, air could be insufflated into the stomach. Again, the system was an improvement over the previous models, but even with the greatest dexterity and finest technique, there were blind spots that could not be visualized (Figs. 7, 8).

In 1952, Fourestier et al. introduced a new means of light transmission--a rigid quartz rod, measuring 1.5 mm in diameter that was inserted into a highly polished stainless steel tube. This 2-ram light guide was placed inside a rigid endoscope. On the proximal end, a prism was attached with a 15-V globe and a condenser lens. The intensity of the light was brilliant (even superseding today's illumination in intensity and color temperature while producing less heat), but the system was clumsy, fragile, complicated, and difficult to maintain. Nevertheless, the quartz rod system contributed to the development of the first high-quality movie films (16 ram) that were produced for various endoscopic procedures in which a rigid system could be employed (Fig. 9) [16].

There were many other sporadic reports of the new rigid endoscopic procedures, but the limitations imposed by the Nitze lens system (which was slightly improved), the distal electric globe, the size of the instruments, and the lack of flexibility all represented a roadblock to further developments.

Documentation

Even Nitze recognized the importance of maintaining photographic records of interesting or unusual findings to share with his colleagues. At the turn of the century, he developed a cystoscope with a rotating drum at the end. It had a disc with 10 small holes, where he inserted small glass plates covered with light-sensitive material. The exposure times were long (3-5 sec). It is true that many of the pictures were useless, but he was able to publish an atlas based on the pathology of the urinary bladder (Fig. 10).

Using the Schindler gastroscope, in 1938 Henning and Keilhack produced the first color pictures from the stomach. A globe was over burned to create a flash. Due to efforts to reduce the exposure time, the globes burned out very frequently.

In 1941 in Chicago, Hollinger and Brubaker produced the first high-quality movie films from the bronchial tree, larynx, and esophagus. They employed a slightly larger caliber rigid open tube with a high-intensity light and a 16-ram camera (Fig. 11).

The latter half of the 20th century and the revolution in endoscopic procedures

To address the limitations of the Nitze optical system, H. H. Hopkins, a London physicist, devised the prototype of a new optical system in 1954. He replaced the previous lens and air interspaces optical relays using glass rods instead of interspersed air. He also cemented better lenses on both ends. Hopkins created a system that had the following distinct advantages over the Nitze system (Fig. 12):

1. The light transmission was significantly greater (or the absorption less). The consequent brighter image enabled the examiner to distinguish the features more easily and recognize slight changes more clearly. In general, perception was improved.
2. The viewing angle, which was small with the previous optics, was wider. Therefore, the examiner could see a larger part of the object in a single viewing field; thus, as soon as the telescope was introduced, orientation was faster.
3. The system included several improved optical parameters-- e.g., natural color reproduction, image quality at the edge, higher resolution, etc.
4. The system was smaller in diameter. Therefore, the instrument could be made smaller, resulting in easier and safer introduction. With further miniaturization, it was possible to produce telescopes measuring 2-3mm in diameter, including fiber light transmission. This improvement opened up a new chapter in pediatric bronchoesophagology, newborn and infant cystoscopes (Fig 6 and 7), and pediatric laparoscopes with a diameter of 4mm, leading to a whole new era in pediatric endoscopy.
5. Thanks to the brighter image and increased light transmission, the examiners were able to document their findings by attaching 35mm still cameras, 16mm movie cameras, and, later on, video systems.

Dr. Hopkins transferred this novel idea to an interested manufacturer (Karl Storz). The first sets of instruments were released in the early 1960s, leading to a new epoch in rigid instrumentation. If Hopkins had not invented the system, the pediatric endoscopic and laparoscopic revolution in endoscopy would never have occurred.

It is important to note that both Hopkins and a Dutch physicist named van Heel, publishing in the same scientific journal (*Nature*), described the first flexible optical system. This represented yet another breakthrough by creating the possibility of building instruments in which the optical image relay system could be bent. Hirschowitz invented the first flexible gastroscope in 1958, thus introducing a completely new diagnostic and therapeutic modality in the field of gastroenterology and for the biliary system.

Illumination

The problem of illumination has always plagued both the operators and the manufacturers. Lamm, a gynecologist, published a paper in a technical journal in 1930 that showed that when fiber threads of several microns in diameter are put together in a bunch and bent, light can still be transmitted through them, despite the flexure [33]. This idea was not developed until 1950 (Fig. 13).

Today, fiber threads are well-known standard parts of every flexible scope. If these fiber threads are not well assorted (i.e., incoherent), they can be used for light transmission only. But if they are appropriately assorted on both ends, an image can be transmitted. Hopkins, a few years after Lamm's report, demonstrated the flexible gastroscope at a meeting in Holland, but it was not accepted until Hirschowitz et al.'s historic article in 1958 (Fig. 14).

Television

Over the last 50 years, the invention and widespread acceptance of communication via television has altered all of our lives significantly. It has also had a considerable impact on endoscopy. There is no question that looking through the small, dim pupil of an eyepiece is a handicap that can produce substantial variations in the descriptions of findings of different examiners. It became obvious that the medium of television had great potential for endoscopy.

The advantages are obvious. The image can be seen immediately with *both eyes* from a *convenient distance*. The image is significantly *enlarged* therefore, it can be observed with ease, and small changes in anatomy and/or anomalies can be discovered. *Several team members* can see the image *simultaneously*, thereby, facilitating *coordinated assistance* in complex procedures. It can be *recorded* on videotape and analyzed at leisure without the patient being present. Thus, television has become an important tool for consultation, teaching, and lecturing.

The first televised bronchoscopy was reported in France by Soulas in 1956. The patient was, practically speaking, brought to a television studio, and a rigid bronchoscope was attached to a camera (Orthicon) weighing 100 lb [55]. This, of course, was in black and white. A few years later, although the cameras (Vidicon) were smaller, they were still too heavy and unwieldy (Fig. 15). One of the fundamentals of any endoscopic technique is that the operator has complete control for the passage and manipulation of the instrument. The operator is largely dependent on the sensation or resistance conveyed to the hand.

The first miniature endoscopic television camera (black and white) was developed in a surgical department in Melbourne, Australia, in 1960. It was 45 mm wide and 120

mm long and weighed only 350 g (Fig. 16). It could be quickly attached to the eyepiece of an endoscope. Because it had a monochrome display, it did not gain acceptance. However, we did not give up hope. We continued to experiment following the development of color cameras. Nevertheless, we had to ask ourselves a few questions:

1. Is there a video technique that can be adapted to endoscopy?
2. Is the image on the TV screen comparable to a normal visual image?
3. Are the advantages of television substantial?

The answer to each of these questions is a definite yes. We started with a 1 inch striped Vidicon color camera, but it proved to be too unwieldy. The breakthrough was achieved with the introduction of the charged-coupled device (CCD) image sensors (Fig. 17). The first report of a CCD chip camera attached to the choledochoscope during choledochotomy came in 1985 [6]. The camera and endoscope were sterilized together (Fig. 18).

In 1986, we published the first report of the routine use of television laparoscopy using a miniature camera [1]. Throughout its evolution, electronic imaging has improved, and today it is accepted as an important integral part of the endoscopic procedure.

Enormous changes have occurred in the field of flexible endoscopy. Miniature chips were inserted at the working tip of the endoscope, and the flexible fiber image bundle was replaced by a miniature camera inserted into the organ under investigation. The advantages to the system are obvious. The image quality is significantly better, and this system now represents the standard technology for larger flexible endoscopes (8-12mm). The addition of computerized data insertion has made the system even more valuable.

Hysteroscopy

Hysteroscopy is the examination of the internal cavity of the uterus (endometrium) with the use of a fine endoscope (hysteroscope) which is inserted into the uterus through the vagina and cervix. With hysteroscopy the endometrium is examined and treated more reliably than with any other method (transvaginal ultrasound, hysterosalpingogram, dilatation & Curettage, etc). Hysteroscopy is performed for a variety of gynecological problems such as abnormal uterine bleeding (menorrhagia), infertility, polyps, fibroids, endometrial adhesions, uterine diaphragm, endometrial hyperplasia, cancer etc. Diagnostic and micro-invasive hysteroscopy is performed under local anesthesia while invasive hysteroscopy is performed either under local, general or epidural anesthesia, depending on medical settings and patient's characteristics. Hospital stay ranges from a one hour to one day depending on the

case. As a diagnostic and therapeutic tool hysteroscopy is essential in modern gynecology and is performed with great safety and accuracy.

Benefits of Hysteroscopy

Dysfunctional uterine bleeding is one of the commonest gynecological problems and is expressed either as increased blood loss during menstruation and / or as irregular bleeding independent of the menstrual cycle. In the majority of cases, especially in women > 35 years old, the cause of bleeding is associated with pathology of the endometrium (polyps, hyperplasia, fibroids etc). The incidence of cancer is increased with advanced female age and its early and accurate diagnosis is of great importance. Hysteroscopy provides with accurate diagnosis of the cause of bleeding and at the same time treatment is applied in the majority of cases.

Endometrial polyps and submucosal fibroids may be commonly found in the endometrium. Patients often present with infertility and / or bleeding, but some of them are diagnosed incidentally during routine transvaginal ultrasound examination. These are mostly benign but malignancy can only be excluded after histological examination (biopsy) of the excised tissue.

Endometrial adhesions are the presence of fibrous tissue within the endometrium and are caused by trauma and / or infection (dilatation & curettage, miscarriage, endometritis, intrauterine surgery, post-natal infection, Chlamydia infection etc). Endometrial adhesions may be associated with infertility and miscarriages. Adhesions may be suspected by the reduction of menstrual blood loss but often they are diagnosed in patients with no symptoms. Past medical history and transvaginal ultrasound may raise the suspicion of adhesions; however hysteroscopy is the gold standard in diagnosis of endometrial adhesions and is recommended for the investigation of infertility and miscarriages. Treatment of adhesions may prove difficult even with hysteroscopic adhesiolysis due to missing of normal endometrial mucosa and may require repeat hysteroscopy depending on the severity of the condition.

Until recently, the standard method for the examination of the inner female organs was laparoscopy. Laparoscopy though, is unable to examine the endometrium, which is a significant organ in fertility. Currently, hysteroscopy is best performed at the same time as laparoscopy in all cases of Infertility. Hysteroscopy is also recommended in cases of unexplained infertility, unsuccessful IVF attempts and miscarriages. The crucial role of hysteroscopy in the management of infertility has been presented by many gynecological surgeons worldwide.

Dysfunctional uterine bleeding (menorrhagia, intermenstrual, postmenopausal bleeding) is one of the early signs of endometrial cancer and its incidence is

increased with advanced female age. Expert performance of transvaginal ultrasound may detect thickened endometrium or/and polyps and haematometra (blood within the endometrium) well before the onset of abnormal bleeding. Further investigation by Hysteroscopy and biopsy is then required for confirmation or exclusion of the diagnosis when there is suspicion of endometrial cancer. With the performance of D&C alone (Dilatation & Curettage), less than half of the endometrium is sampled and examined and as a result there is a significant number of cancer patients who are denied an accurate diagnosis and, hence, appropriate and timely treatment.

Women with history of breast cancer-Tamoxifen therapy, history of hyperplasia, thickened endometrial cavity, anovulatory polycystic ovaries, obesity-diabetes etc) etc. is considered high risk for developing endometrial polyps, hyperplasia or endometrial cancer. These women may benefit by periodic hysteroscopy and biopsy examination under local anesthesia.

Chapter 2

Fundamentals of Tissue Optics

In his review paper [Boulnois 1986] discusses the various interaction mechanisms between light and tissue. He identifies the following major categories of interactions that lead to alterations of the tissue structure or composition:

- *Photochemical*: absorption of light by molecules present in or added to tissue. Photochemical interactions form the basis for Photodynamic Therapy (PDT).
- *Thermal*: biological effects due to deposition of thermal energy in tissue. Thermal interactions are commonly used in laser surgery.
- *Photoablative*: in the ultra – violet wavelength range photons possess sufficient energy to cause photo – dissociation of biopolymers and subsequent desorption of the fragments.
- *Electromechanical*: occurs at very high fluence rates where dielectric breakdown of tissue is induced which can lead to the formation of plasma. The rapid expansion of such plasma generates a shock wave which can rupture the tissue.

In optical tomography the fluence rates are chosen to be sufficiently small so that these types of destructive changes do not occur in tissue. Instead, only linear and time-invariant absorption and scattering interactions of light are considered. The first section of this chapter introduces the physical principles of the interaction of photons with tissue, and the second section discusses mathematical models that describe the propagation of light through tissue. General textbooks on absorption and scattering have been written by [Ishimaru 1978] and [Bohren 1983].

Optical properties of tissue

Absorption and scattering, the two physical phenomena affecting light propagation in biological tissue, will be discussed in this section. Although both are important, scattering is the dominant mechanism [Cheong 1990]. Even for thin, sub-millimeter, sections of tissue, injected photons are likely to be scattered several times before they reach the boundary. As a consequence a coherent, collimated input laser beam will be effectively incoherent and isotropic after traversing a few millimeters of tissue. Absorption, and to a lesser extent scattering, are wavelength dependent. Moreover, the concentration of some of the absorbers (chromophores) varies in time, reflecting physiological changes in the tissue. Most importantly, hemoglobin, the oxygen-carrying molecule of the red blood cells, shows a strong oxygenation state dependent absorption profile. The refractive index varies very little on a

macroscopic scale and is typically around 1.40 for most tissue types [Bolin 1989]. The refractive indices of the individual tissue constituents vary from 1.33 for water to approximately 1.55 for fat and concentrated protein solution [Bennett 1951].

Unfortunately, investigators working in the field of biomedical optics use a variety of different units. In order to avoid confusion, the units used throughout this thesis are defined in this section.

Absorption

The *absorption coefficient*, μ_a (in units mm^{-1}), can be defined as:

$$dI = -\mu_a I dx$$

where dI is the differential change of the intensity I of a collimated light beam traversing an infinitesimal path dx through a homogeneous medium with absorption coefficient μ_a . Integration over a thickness x yields:

$$I = I_0 e^{-\mu_a x}$$

The absorption coefficient can also be expressed in terms of particle density ρ and absorption cross section σ_a as:

$$\mu_a = \rho \sigma_a$$

giving the *Beer – Lambert* law:

$$I = I_0 e^{-\rho \sigma_a x}$$

The reciprocal, $1/\mu_a$, is called the *absorption pathlength* and equals the mean free path a photon travels between consecutive absorption events. Another quantity that is commonly used is the *specific extinction coefficient* α , which represents the level of absorption per μmol of compound per liter of solution per cm (usually quoted in units $\mu\text{molar}^{-1} \text{cm}^{-1}$). It is defined using base 10 logarithm units, and can be related to the absorption coefficient via the following expression:

$$\alpha = \log_{10}(e) \cdot \frac{\mu_a}{c}$$

where c is the concentration of the compound (in units of μmolar). The *transmission*, T , is defined as the ratio of transmitted to incident intensity:

$$T = \frac{I}{I_0}$$

and the *attenuation*, or *optical density* (OD) of an attenuating medium is given by

$$\text{OD} = \log_{10}(1/T) = -\log_{10}\left(\frac{I}{I_0}\right)$$

Hence

$$\text{OD} = \log_{10}(e) \cdot \mu_a x = \alpha c x$$

Scattering

Refractive index mismatches on a *macroscopic* scale, e.g. between skin and skull, give rise to refraction, but are usually so small that they are ignored in most photon transport models. However, scattering of light in biological tissue is caused by refractive index mismatches at *microscopic* boundaries such as cell membranes, organelles, etc. In the same manner as for absorption, one can define a scattering coefficient, μ_s (in units mm^{-1}), for a collimated source, such that

$$I = I_0 e^{-\mu_s x}$$

where I is the non-scattered component of light after traversing a non-absorbing sample of thickness x . The scattering coefficient in terms of particle density ρ and scattering cross section σ_s is:

$$\mu_s = \rho \sigma_s$$

The scattering pathlength, $1/\mu_s$, is the average distance a photon travels between consecutive scattering events and the quantity $\mu_s x$ is the (dimensionless) *optical thickness* of a sample expressed in terms of scattering pathlengths.

When a photon that is incident along a direction described by the unit vector \mathbf{e}_s experiences a scattering event, the angular probability of it being scattered into direction \mathbf{e}_s' is given by the normalised *phase function* $f(\mathbf{e}_s, \mathbf{e}_s')$. For random, soft tissues it can be assumed that the probability distribution is a function of the angle between the incident and scattered photon only, and does not depend on the angle of incidence relative to the scatterer. Hence the phase function can be conveniently expressed as a function of the cosine of the scattering angle $\mathbf{e}_s \cdot \mathbf{e}_s' = \cos(\theta)$

$$f(\mathbf{e}_s, \mathbf{e}_s') = f(\cos \theta)$$

A theory developed by [Mie 1908] enables analytical solutions of the phase function to be derived for the scattering of a plane electromagnetic wave by isotropic spherical particles of any size. Note that in the limit where the size of the scatterer is much less than the wavelength of the incident photon, Mie theory can be approximated by Rayleigh's theory of scattering [Rayleigh 1871]. This, however, is of limited significance for scattering in biological tissues.

The anisotropy can be characterized in terms of the mean cosine of the scattering angle, called the *anisotropy factor* g :

$$g = \int_{-1}^1 \cos \theta f(\cos \theta) d \cos \theta$$

The limiting cases are $g=0$ for perfectly isotropic scattering, and $g=1$ for complete forward scattering of the incident wave. Biological tissues in the NIR wavelength range are strongly forward scattering with anisotropy factors typically in the range $0.69 \leq g \leq 0.99$ [Cheong 1990]. The *transport* (or *reduced*) *scattering coefficient*, μ_s' , is defined as:

$$\mu_s' = \mu_s (1 - g)$$

This quantity can be interpreted as representing the equivalent isotropic scattering coefficient and is a fundamental parameter in the diffusion theory of light propagation through random media. The mean path travelled by a collimated beam of light before it becomes effectively isotropic is given by $1/\mu_s'$.

Combining absorption and scattering, one can define a *total attenuation coefficient*:

$$\mu_t = \mu_s + \mu_a$$

where $1/\mu_t$ is commonly referred to as the *mean free path* between either a scattering or absorption event. By analogy, the *transport attenuation coefficient*, μ_{tr} , is defined as :

$$\mu_{tr} = \mu_a + \mu_s(1 - g) = \mu_a + \mu_s'$$

Optical properties of various tissue types

The main constituents of biological tissue which contribute towards absorption in the near infrared are water, fat and hemoglobin. While the former two remain fairly constant over short time-scales, the concentrations of oxygenated and deoxygenated hemoglobin change according to the function and metabolism of the tissue. Thus the corresponding changes in absorption can provide clinically useful physiological information. This section discusses the absorption properties of these tissue constituents as well as measurements of the absorption and scattering coefficients of a variety of specific tissues.

Water

The absorption spectrum of water [Cooper 1996] in the range 600-1050 nm is shown in Figure 2–1. Significant transmission through tissue is only possible from the UV (about 200 nm, not shown in spectrum) to the near infrared (about 935 nm). The absorption drops again beyond 1000 nm, but there are currently no efficient detectors available at such long wavelengths.

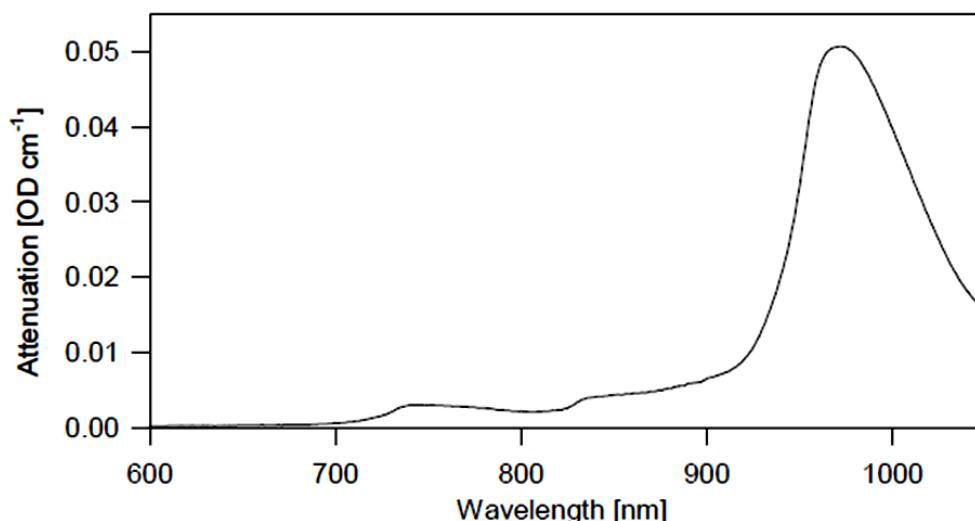


Figure 1 Absorption spectrum of water.

Note that although the absorption coefficient of water is rather low in this ‘water transmission window’, it is still a significant contributor to the overall attenuation as

its concentration is very high in biological tissue. The average content in the neonatal brain is 90% [Fillerup 1967], and 80% in the adult brain [Woodard 1986].

Lipids

Lipids, or fat, make up about 5% of the neonatal brain's weight. Figure 2–2 represents the absorption spectrum of pork fat [Conway 1984], which is thought to be largely identical to that of human lipids. The absorption coefficient, which is of the same order of magnitude as for water, is low at shorter wavelengths (down to about 600 nm, not shown in spectrum), with a strong peak at about 930 nm. However, because of the low content of lipids in the brain, the effect on the overall absorption is rather small.

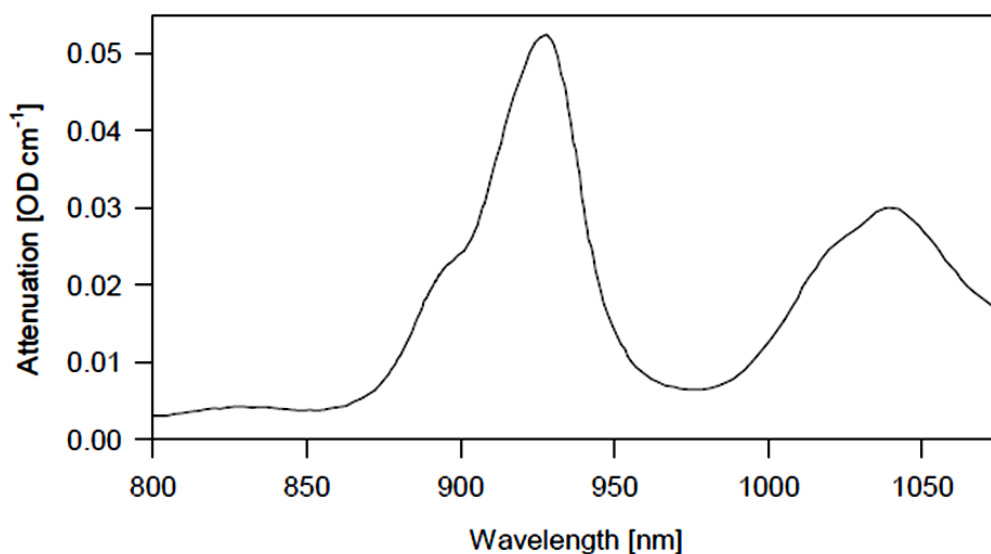


Figure 2 Absorption spectrum of fat.

Hemoglobin

Hemoglobin molecules within the red blood cells (Erythrocytes) carry 97% of the oxygen in the blood, while the remaining 3% is dissolved in the plasma. Each hemoglobin molecule consists of four iron-containing haeme groups as well as the protein globin. It is the iron to which the oxygen atoms easily bind, causing the hemoglobin molecule to assume a new three-dimensional shape. In the oxygenated state hemoglobin is referred to as *oxyhemoglobin* (HbO₂), and in the reduced state it is called *deoxyhemoglobin* (Hb). Figure 2–3 shows the oxygen-hemoglobin dissociation curve [Severinghaus 1979], which relates the percentage saturation of hemoglobin (SO₂) to the partial pressure of oxygen dissolved in blood (PO₂).

The spectra of oxy- and deoxyhemoglobin, expressed in terms of the specific extinction coefficient, can be seen in Figure 2–4. While both absorb strongly in the

blue and green regions of the visible spectrum, the absorption of deoxyhemoglobin is slightly stronger beyond about 690 nm. Hence venous blood appears in a darker red than the arterial blood. Note the isobestic point at about 800 nm, where the two curves intersect. If one is able to accurately determine the tissue absorption coefficients at, say, 20 nm, to either side of this wavelength it is then possible to determine both blood volume and oxygenation [Cope 1988]. The strong increase in absorption below 600 nm sets a lower limit for spectroscopic or imaging measurements. Optical properties of blood in the wavelength range 400-2500 nm are discussed in great detail by [Roggan 1999].

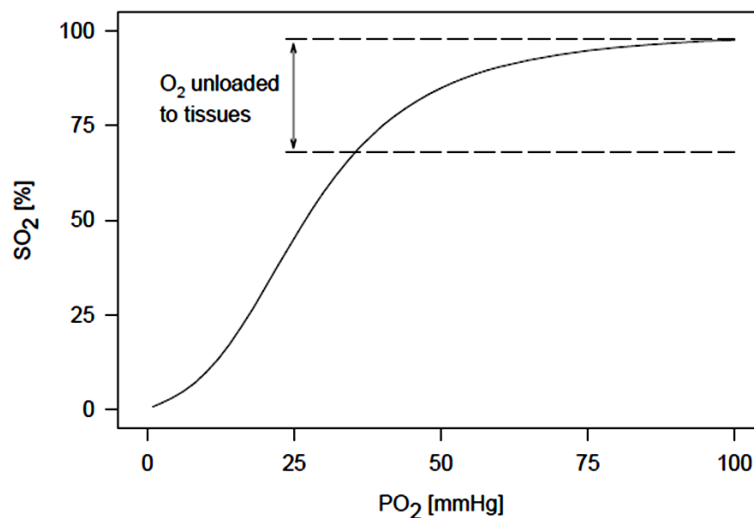


Figure 3 Oxygen – hemoglobin dissociation curve. Note that the oxygen saturation of blood leaving the lungs (the arterial saturation) is about 97%, while that of venous blood is still about 67%. Hence approximately 30% of the hemoglobin – bound oxygen is unloaded in the tissues during one cycle through the body.

Tissue type	Sample	λ [nm]	μ_a [mm ⁻¹]	μ_s' [mm ⁻¹]	Reference
neonatal grey matter	in vitro	650-900	0.04-0.08	0.4-0.9	[van der Zee 1993]
neonatal white matter	in vitro	650-900	0.04-0.07	0.5-1.2	[van der Zee 1993]
adult brain	in vitro	700-900	0.1-0.2	2-5	[Sterenborg 1989]
adult grey matter	in vivo	811	0.018-0.019	0.48-0.74	[Bevilacqua 1999]
adult grey matter	in vivo	849	0.018-0.019	0.45-0.74	[Bevilacqua 1999]
adult white matter	in vivo	849	0.013	0.98	[Bevilacqua 1999]
adult skull	in vivo	849	0.022	0.91	[Bevilacqua 1999]
adult grey matter	in vitro	650-900	0.04-0.06	1.9-2.2	[van der Zee 1993]
adult white matter	in vitro	650-900	0.02-0.03	8-10	[van der Zee 1993]
pig brain	in vitro	630	0.026	5.7	[Patterson 1987]
pig skull	in vitro	650-950	0.04-0.05	2.63-1.32	[Firbank 1992]
healthy breast tissue	in vitro	700-900	0.022-0.075	0.53-1.42	[Peters 1990]
breast carcinoma	in vitro	700-900	0.045-0.050	0.89-1.18	[Peters 1990]
healthy breast tissue	in vivo	800	0.002-0.003	0.72-1.22	[Mitic 1994]

Table 1 Optical properties of various tissue types

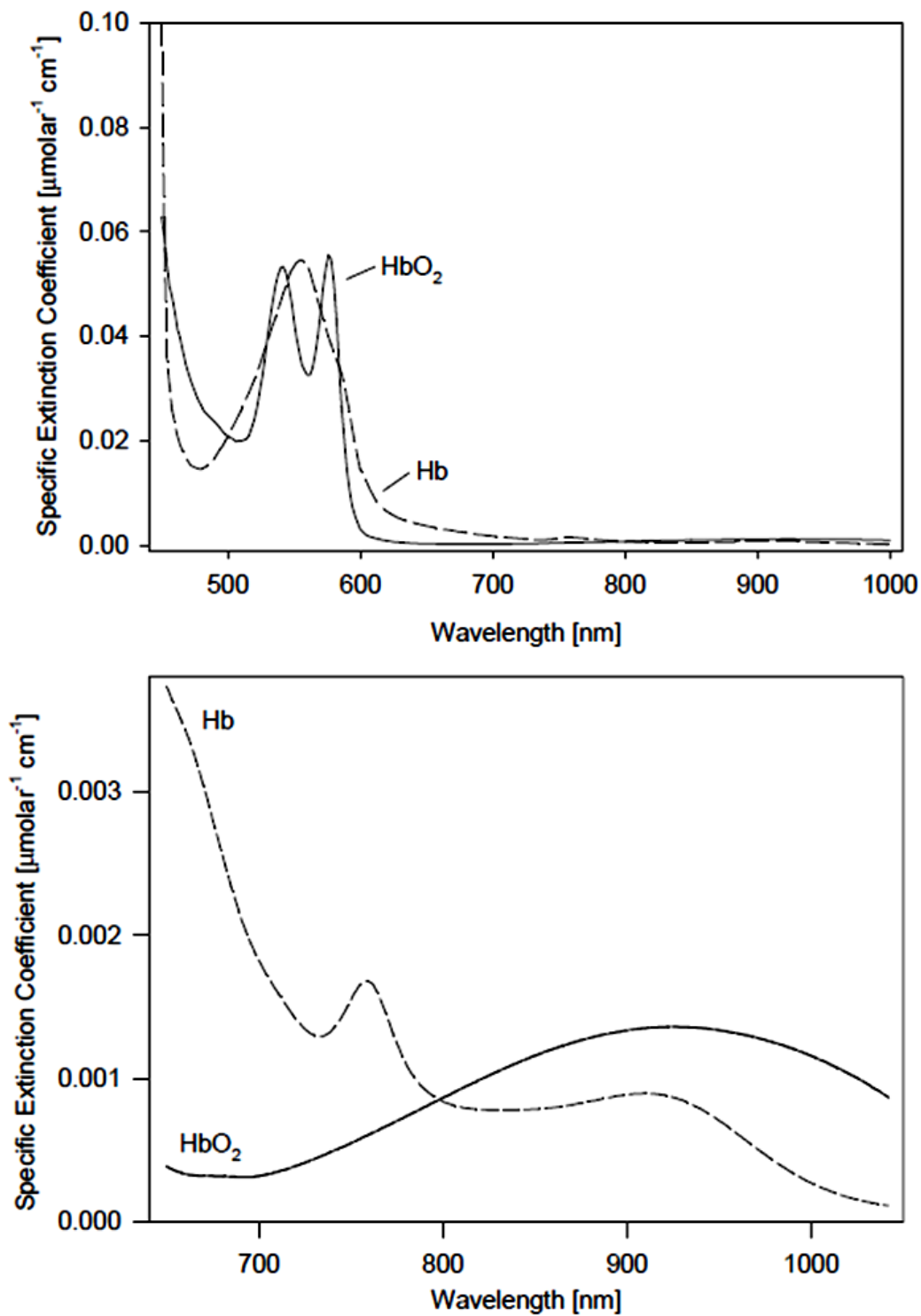


Figure 4 Absorption spectra of oxy- and deoxyhemoglobin in the ranges 450 – 1000 nm (top), and 650 – 1050 nm (bottom) [Cope 1991].

There is a number of other tissue chromophores, such as melanin, cytochrome c oxidase, myoglobin, etc. These can be largely ignored in the near infrared (but not in the visible!) regime, as they contribute little to the overall attenuation. The combined 'absorption window' lies in the range 600-900 nm. Taking into account the

increase in scattering at lower wavelengths and a rapid drop in quantum efficiency of practical detectors at longer wavelengths, the 'useful' range is approximately 650-900 nm. Table 2–1 above summarizes the absorption and scattering coefficients of various tissue types relevant to this project, together with the corresponding reference source for the data.

Note the low scattering of the neonatal as compared to the adult brain, as well the smaller differences between grey and white matter. These facts combined with the small neonatal head size (approximately 6-12 cm across), and the thinner clear CSF layer (see section 2.1) suggest that light is much more likely to penetrate deep into the neonatal, as compared to adult, white matter – thus supporting the feasibility of a neonatal brain imaging modality. The thickness of the CSF layer is relevant because it exhibits low absorption and almost no scattering, therefore acting as a light guide which can channel photons around the head without much penetration into the grey and white matter [Firbank 1995a, Okada 1995].

Finally, it has to be noted that most measurements presented in the table were made using *in vitro* tissue samples, which can yield very different results as compared with *in vivo* results. In addition, the measurement techniques currently available still contain many sources of error, and most published data have been obtained with only a small number of samples. The data must therefore only be taken as being approximate. Consequently it is important for the field that investigators continue to explore the optical properties of the human neonatal head.

Modeling of photon transport in tissue

In the previous section, the basic physical principles of the interaction of photons with tissue were outlined. The propagation of light through tissue is governed primarily by absorption and scattering interactions, the latter being the dominant mechanism.

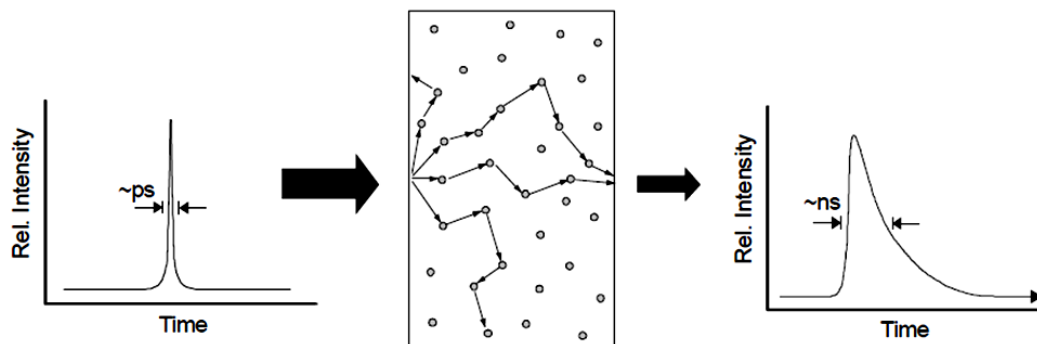


Figure 5 Diagram illustrating the diffuse propagation of light through a thick section of tissue. A narrow input beam of pulsed light is injected and becomes dispersed temporally and spatially through multiple scattering events.

As a consequence, a very short pulse of collimated light input into a highly scattering medium (such as tissue) will become effectively diffuse and disperse in time after only a few mm. Figure 2–5 schematically illustrates this effect.

This section introduces mathematical models that have been used to describe the propagation of light through tissue. Such *forward models* are required for solving the *inverse problem* in optical tomography. A more in-depth treatment of the subject is given in the review papers by [Patterson 1991] and [Arridge 1997, Arridge 1999].

The Radiative Transfer Equation

Propagation of light in tissue can, in principle, be described using fundamental electromagnetic theory. In this case tissue can be considered a random medium with a spatially varying permittivity $\epsilon(\mathbf{r})$, and variations of the electric field would be described using Maxwell's equations. However, such a treatment is currently not feasible because of the complexity of the problem and a lack of precise knowledge of $\epsilon(\mathbf{r})$. Instead the problem can be simplified by ignoring wave phenomena such as polarization and interference, and particle properties such as inelastic collisions. This is a very good approximation for large thicknesses (> several mm) of biological tissue in the near infrared. The basic assumption in radiative transfer theory is that only the flow of energy through the medium is considered. The *Radiative Transfer Equation* (RTE),

$$\frac{1}{c} \frac{\partial I(\mathbf{r}, t, \mathbf{e}_s)}{\partial t} + \mathbf{e}_s \cdot \nabla I(\mathbf{r}, t, \mathbf{e}_s) + (\mu_a + \mu_s) I(\mathbf{r}, t, \mathbf{e}_s) = \mu_s \int_{4\pi} f(\mathbf{e}_s, \mathbf{e}_s') I(\mathbf{r}, t, \mathbf{e}_s') d^2 \mathbf{e}_s' + q(\mathbf{r}, t, \mathbf{e}_s)$$

is an integro-differential equation and describes the change of *energy radiance* $I(\mathbf{r}, t, \mathbf{e}_s)$ at position \mathbf{r} into direction \mathbf{e}_s . The other parameters are:

- c speed of light in the medium;
- μ_a absorption coefficient;
- μ_s scattering coefficient;
- $f(\mathbf{e}_s, \mathbf{e}_s')$ scattering phase function;
- $q(\mathbf{r}, t, \mathbf{e}_s)$ radiation source.

The energy radiance $I(\mathbf{r}, t, \mathbf{e}_s)$ is the energy transfer per unit time per unit solid angle $d^2 \mathbf{e}_s$ through a unit area at position \mathbf{r} and time t . Thus integrating $I(\mathbf{r}, t, \mathbf{e}_s)$ over all angles gives the *flux* Γ through a unit area given by \mathbf{e}_n :

$$\Gamma(\mathbf{r}, t) = \int_{4\pi} I(\mathbf{r}, t, \mathbf{e}_s) \mathbf{e}_s \cdot \mathbf{e}_n d^2 \mathbf{e}_s$$

The RTE can be derived by considering the radiant energy balance in an arbitrary elemental volume of tissue. It is a balance equation relating the change of the energy radiance $I(\mathbf{r}, t, \mathbf{e}_s)$ in time (1st term) to a change in energy flow (2nd term), loss due to absorption and scattering (3rd term), gain due to scattering sources (4th term), and gain due to radiation sources (5th term). Although the wave nature of light is ignored in its derivation, polarization can be included by using Stokes parameters, and deriving four instead of one radiative transfer equations. While exact solutions for the RTE exist for simple cases such as isotropic scattering in simple geometries [Patterson 1991], there is no general solution. Therefore one needs to make further approximations or compute numerical solutions. The following sections will describe a number of deterministic and stochastic models of photon transport derived from the RTE.

Deterministic models

It is possible to derive deterministic approximations to the RTE that can be solved for a variety of geometries. Two commonly employed models, the diffusion approximation and Kubelka-Munk theory, will be introduced in this section.

The diffusion approximation to the Radiative Transfer Equation

By expanding the RTE in spherical harmonics one can derive a hierarchy of equations [Kaltenbach 1993], of which the simplest, the so-called P_1 approximation, is the *time dependent diffusion equation*:

$$\frac{1}{c} \frac{\partial \Phi(\mathbf{r}, t)}{\partial t} - \nabla \cdot \kappa(\mathbf{r}) \nabla \Phi(\mathbf{r}, t) + \mu_a(\mathbf{r}) \Phi(\mathbf{r}, t) = q_0(\mathbf{r}, t)$$

where Φ is the photon density

$$\Phi(\mathbf{r}, t) = \int_{4\pi} I(\mathbf{r}, t, \mathbf{e}_s) d^2 \mathbf{e}_s$$

and κ is the diffusion coefficient defined as

$$\kappa(\mathbf{r}) = \frac{1}{3[\mu_a(\mathbf{r}) + \mu'_s(\mathbf{r})]}$$

The q_0 term represents an isotropic source. The *flux* Γ along the normal e_n of the boundary at point ξ can then be shown to be

$$\Gamma(\xi, t) = -\kappa(\xi) \frac{\partial}{\partial n} \Phi(\xi, t)$$

Note that the following important approximations have been made:

- The P_1 approximation is valid only for $\mu_a \ll \mu_s$. Although this is true for most biological tissues in the near infrared, there are region of the body where the diffusion approximation does not strictly hold. One such region is the CSF filled clear layer of the head. It has yet to be established how severe the effect of this layer in on a diffusion model based image reconstruction scheme.
- Higher order source terms are ignored. This implies that non – isotropic sources cannot directly be incorporated into a diffusion based model.

Analytical Solutions

Analytical solutions to the time-dependent diffusion equation (4.18) exist for some simple geometries [Patterson 1989, Arridge 1992, Contini 1997]. The simplest case is that of an infinitely short pulse in an infinite homogeneous medium, such that the source $q(\mathbf{r}', t') = d(\mathbf{r}', t')$. The solution for the photon density Φ at position \mathbf{r} and time t , is the Green's function

$$\Phi(\mathbf{r}, t) = \frac{1}{(4\pi c\kappa(t-t'))^{3/2}} \exp\left(-\frac{(r-r')^2}{4c\kappa(t-t')} - \mu_a c(t-t')\right)$$

It is also possible to derive an analytical solution for the case of a semi-infinite slab, which extends beyond $z \geq 0$. An *effective* isotropic point source, which can be thought of as simulating a narrow collimated laser beam incident at $z_0=0$, is placed at depth $z_0=1/ms$. Together with the boundary condition $\Phi(z=0, t)=0$ this can be shown to give

$$\Phi(\mathbf{r}, t) = \frac{1}{(4\pi c\kappa(t-t'))^{3/2}} \exp\left(-\mu_a c(t-t') - \frac{\rho^2}{4c\kappa(t-t')}\right) \cdot \left[\exp\left(\frac{-(z-z_0)^2}{4c\kappa(t-t')}\right) - \exp\left(\frac{-(z+z_0)^2}{4c\kappa(t-t')}\right) \right]$$

where $\rho = [(x-x')^2 + (y-y')^2]^{-1/2}$ is the radial distance from the input position. The solution for an infinite slab with boundaries at $z=0$ and $z=d$, and the boundary condition $\Phi(z=0,t) = \Phi(z=d,t) = 0$ is

$$\Phi(\mathbf{r}, t) = \frac{1}{(4\pi c\kappa(t-t'))^{3/2}} \exp\left(-\mu_a c(t-t') - \frac{\rho^2}{4c\kappa(t-t')}\right) \cdot \sum_{N=-\infty}^{N=+\infty} \left[\exp\left(\frac{-(z-2Nd-z_0)^2}{4c\kappa(t-t')}\right) - \exp\left(\frac{-(z-2Nd+z_0)^2}{4c\kappa(t-t')}\right) \right]$$

The derivation of this expression involves employment of the so-called method of images [Patterson 1989]. As an example, the computed TPSF for an infinite slab of thickness $d = 50$ mm, and optical properties $\mu'_s = 1.0 \text{ mm}^{-1}$ and $\mu_a = 0.01 \text{ mm}^{-1}$ is shown in Figure 2–6. Analytical solutions for other simple geometries, such as spheres and cylinders, as well as the frequency-domain equivalents of the above equations, are provided by [Arridge 1992]. Although there are no general solutions for inhomogeneous media, analytical expressions have been derived, which are capable of incorporating a single point-like absorbing perturbation into an otherwise homogeneous medium [Feng 1995, Arridge 1995a].

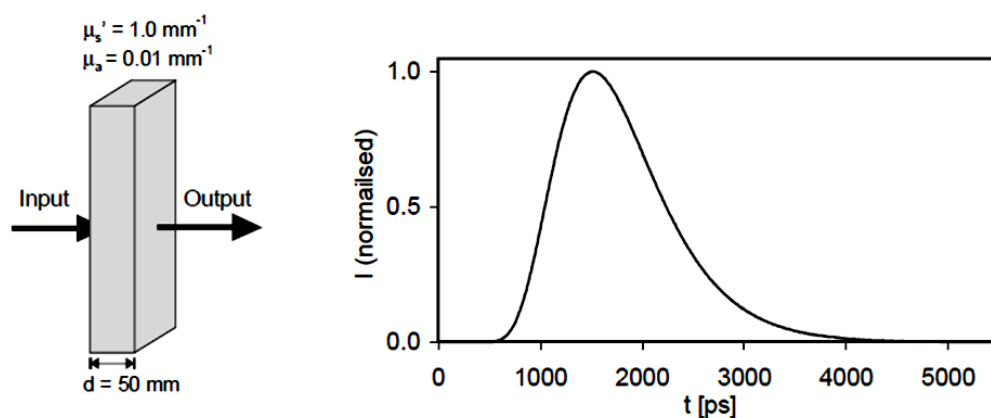


Figure 6 A TPSF (right) calculated from a Green's function for an infinite slab (left).

Numerical solutions

The most common methods for numerically solving the time-dependent diffusion equation for arbitrarily shaped inhomogeneous media are the *finite difference* and *finite element* methods. While the former is based on discretizing the diffusion equation, the finite element method (FEM) involves dividing the medium into a large number of volume or area elements, each of which has its individual set of optical properties, μ_a and μ'_s [Arridge 1993, Schweiger 1994]. Solutions are found simultaneously at all nodes of the finite element mesh by inverting the associated

matrix. Photon densities for the individual elements are then computed from the node values via an interpolation scheme which ensures that continuity of the overall solution, piecewise linearity across the elements and other properties are met.

Although FEM is fast compared to the highly versatile Monte Carlo method, it is still computationally expensive and also requires a large amount of computer memory. This is especially true in a full 3D treatment of the problem.

Kubelka - Munk theory

When considering a homogeneous, plane-parallel, infinite slab of thickness d that is illuminated by a normal plane wave, two (and higher) flux models can be derived. Kubelka and Munk [Kubelka 1931, Kubelka 1954] formulated a two-flux model which considered only the forward and backward flux propagating in an infinite slab of thickness d . The rate of change of these two fluxes is given by

$$\begin{aligned} d\Gamma_+ &= -(K + S)\Gamma_+ dz + S\Gamma_- dz \\ d\Gamma_- &= S\Gamma_+ (-dz) - (K + S)\Gamma_- (-dz) \end{aligned}$$

where K and S are the Kubelka-Munk absorption and scattering coefficients for diffuse light which, in the case of isotropic radiance, equal $K=2ma$ and $S=ms$. [Patterson 1991] discusses the relationship between K/S and ma/ms under more complex circumstances. The last two equations, combined with the boundary conditions $\Gamma_+(z=0)=\Gamma_0$ and $\Gamma_-(z=d)=0$, yield the solutions

$$\begin{aligned} \Gamma_+(z) &= \Gamma_0 \frac{\sinh(bSz)}{a \sinh(bSd) + b \cosh(bSd)} \\ \Gamma_-(z) &= \Gamma_0 \frac{a \sinh(bSz) + b \cosh(bSz)}{a \sinh(bSd) + b \cosh(bSd)} \end{aligned}$$

where

$$a = \frac{S + K}{S}$$

and

$$b = \sqrt{a^2 - 1}$$

Four-flux models which, in addition to the diffuse forward and backward fluxes, also take collimated forward and backward fluxes into account, give more accurate results. Higher order six- and eight-flux models have also been reported [Mudgett 1972, Welch 1987]. Multiple-flux models give good agreement with experimental data. Nonetheless, their usefulness is limited because they are generally restricted to simple slab geometries.

Stochastic Models

In stochastic models of photon transport through tissue (or any other highly scattering medium), individual photon paths are simulated by considering the probability of absorption and scattering interactions. The two most commonly used stochastic models, the Monte Carlo method and Random Walk theory, are briefly outlined in this section.

Monte Carlo

The term Monte Carlo method (MC) refers to numerical simulations based on random sampling from appropriate probability distributions [Wilson 1983, Hasegawa 1991, Hiraoka 1993a, and Hiraoka 1993b]. Light is considered as a stream of particles (photons) that are injected into the medium, and move in straight lines through tissue between successive interactions. The advantages of the Monte Carlo method include simple implementation, the ability to handle any complex geometries and inhomogeneities, as well as the possibility to incorporate time-dependency. It is even possible to model wave phenomena such as polarisation and interference. The main disadvantage is the inherently high computational cost. Given that photons are governed by Poisson statistics, the signal-to-noise ratio (SNR) of the sampled distribution only increases with the square root of the number of traced photons.

The parameters which are required to trace a photon path through some arbitrary random medium are the local absorption coefficient μ_a , scattering coefficient μ_s , and scattering phase function $f(\mathbf{e}_s, \mathbf{e}_s')$. Photons are emitted by a source and travel in straight lines until they are scattered. The probability for a photon to be scattered after a distance $d\tau$ is defined by

$$p(\tau) d\tau = e^{-\mu_s \tau} d\tau$$

Hence the cumulative probability of being scattered after travelling a distance τ is

$$\int_0^{\tau} e^{-\mu_s \tau'} d\tau' = 1 - e^{-\mu_s \tau} \equiv r$$

where $r \in [0...1]$ is a random number. Thus the distance between scattering events is given by

$$\tau = -\frac{1}{\mu_s} \ln(1 - r)$$

which is equivalent to

$$\tau = -\frac{1}{\mu_s} \ln(r)$$

The azimuthal and polar scattering angles, θ and ϕ , relative to the previous direction of motion are given by $\phi = 2\pi r_1$ and

$$\int_0^\theta f(\theta') d\theta' = r_2$$

where r_1 and $r_2 \in [0...1]$ are uniformly distributed random numbers. Absorption can be taken into account either by terminating an absorbed photon's path or by introducing a weighting scheme. Thereby the photon's weight $w \in [0...1]$ is reduced between successive scattering events according to

$$w = w' e^{-\mu_a \tau}$$

where w is the weight before the interaction, and t is the distance travelled since the last scattering event. Photon paths are terminated when either the weight becomes negligible, the photon leaves the boundary or region of interest, or hits the detector. In the latter event the detection count rate is increased by the remaining photon weight w . This technique, also referred to as 'survival weighting', is one of several so called 'variance reduction techniques' that aim to make Monte Carlo simulations more accurate while being computationally efficient.

Random walk

In Random Walk Theory (RWT) the statistical behavior of random walks in space is used to solve for quantities such as the spatial dependence of scattered reflectance arising from a point source [Bonner 1987, Gandjbakhche 1995]. Photon random walks occur on a discrete, cubic lattice where the lattice spacing is equivalent to the root mean square distance between scattering events, and absorption occurs in the

intervening space. While this is equivalent to isotropic scattering, the model can be extended to anisotropic scattering through the use of so called 'constrained walks'.

Despite the fact that the number of directions in which motion is possible is severely restricted, RWT provides a powerful description of photon migration in random media. Predictions of such models have been validated with Monte Carlo simulations, diffusion theory and experimental measurements [Hebden 1995a]. In the limit of large numbers of steps in the walk, one can derive analytic expressions for physical quantities such as the probability of finding a photon a certain distance from a point source. However, as a large number of steps physically correspond to a low probability of absorption, this model is most useful in the regime where diffusion theory also holds. [Chandrasekhar 1943] has shown the equivalence between the two models of photon transport through highly scattering media.

Chapter 3

Tunable Filters

A tunable filter (TF) is a device whose spectral transmission can be electronically controlled by applying voltage, acoustic signal, etc. An ideal tunable filter would possess the attributes listed below. In practice these attributes are only met to a limited degree and each TF technology presents advantages and disadvantages. Hence, each application should carefully consider the tradeoffs, so working solutions should be developed that capture the best attributes of a technology, and overcome other limitations.

- Minimal tunability time
- Minimal out – of – band transmission
- Minimal physical thickness
- Low power consumption
- Polarization insensitive
- Selectable band pass
- Perfect MTF
- Insensitive to environment(e.g. , ambient temperature, humidity)
- Insensitive to angle of incidence of the incoming light(wide FOV)
- Top hat band pass curve(see Fig. 1)
- Large aperture
- Constant band pass
- Random access to wavelengths

Spectral tunability can be achieved in a number of ways. We present ETFs using examples of current and upcoming devices. To fully characterize the spectral transmission of the TF, the transmission over the complete spectral range of interest needs to be characterized when the filter is tuned to a series of spectral positions. The TF performance is described by a matrix $\mathbf{A} = (a_{i,j})$ of $L \times K$ elements, where L transmission curves are measured, each at K wavelengths, where typically $K \gg L$.

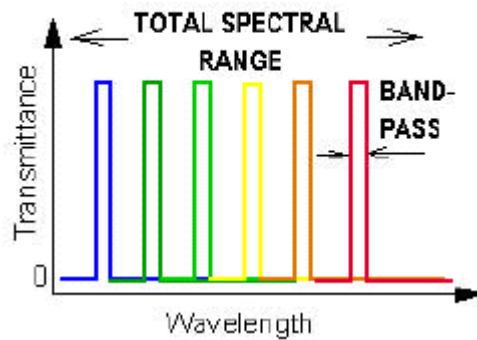


Figure 1. Ideal ETF

Electronically tunable filter examples

We discuss three classes of ETFs: liquid crystal devices based on birefringence, acousto – optical devices based on diffraction, and briefly also mention the better known interferometer type filters.

Liquid crystal tunable filters (LCTFs)

A Lyot-Ohman (or birefringent) filter, Figs. 2 and 3 is built using a stack of polarizers and tunable retardation (birefringent) liquid crystal plates. The transmission of successively thicker retardation plates is shown in Fig. 3 as curves *a, b, c*, etc. The transmission of the complete system comprising the stack is shown by the bottom curve. The LCTF is polarization sensitive. Switching speed is limited by relaxation time of the crystal and is of the order of ~ 50 msec. Special devices can be designed for fast switching (~ 5 msec) through a short sequence of wavelengths.

Spectral resolution, or band pass, of the LCTF is typically of the order of several nm, although a narrower band pass can also be constructed. This is sufficient for most reflectance/transmittance analysis and even Raman measurements. Typical transmission curves are shown in Fig. 4. The band width is constant in frequency space ($Du/u = \text{Const.}$) A blocking filter (e.g., a low pass with a sharp cutoff at 750 nm, in this case) is used to block the out-of-band transmission of the filter.

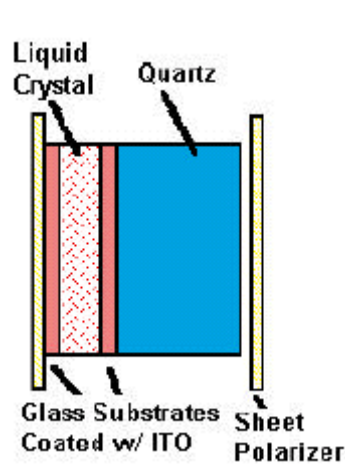


Figure 2. LCTF element

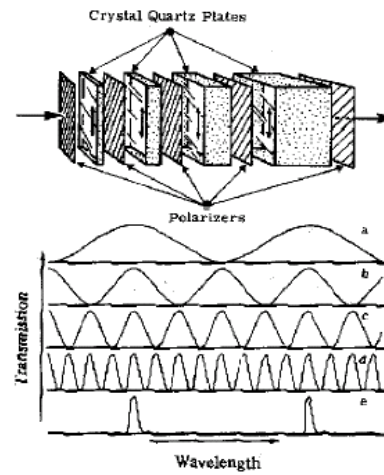


Figure 3. Operating principle of Lyot filter

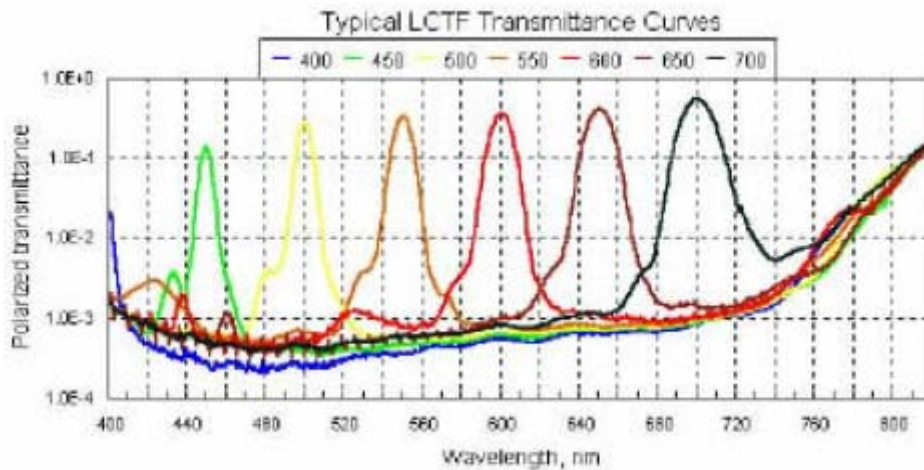


Figure 4. Transmission curves of a real LCTF

Holographically – formed, polymer dispersed liquid crystal (H-PDLC)

A different variation on LCTF is illustrated in Fig. 5, showing the different configurations for polymer and liquid crystal dispersions; (a) conventional PDLC; (b) reflective H-PDLC; and (c) transmissive (sometimes known as diffractive) H-PDLCs. Conventional PDLCs, Fig. 6a, are systems that capitalize on the phase separation of the liquid crystal and the evolving polymer during polymerization. Micron-sized liquid crystal droplets are randomly dispersed in a solid polymer binder after photo polymerization. In the zero-voltage state, the symmetry axis of the droplets is randomly oriented and there is a mismatch in the index of refraction between the surrounding polymer and liquid crystal droplets. This condition results in a strongly scattering (opaque) appearance. By matching the ordinary refractive index of the liquid crystal with that of the surrounding polymer matrix, a transparent condition is

achieved when a sufficient voltage is applied to reorient the liquid crystal droplets. Fig. 6a shows a two pixel device, where the bottom pixel is in the off-state (scattering condition) and the top pixel is in the on-state (transparent condition).

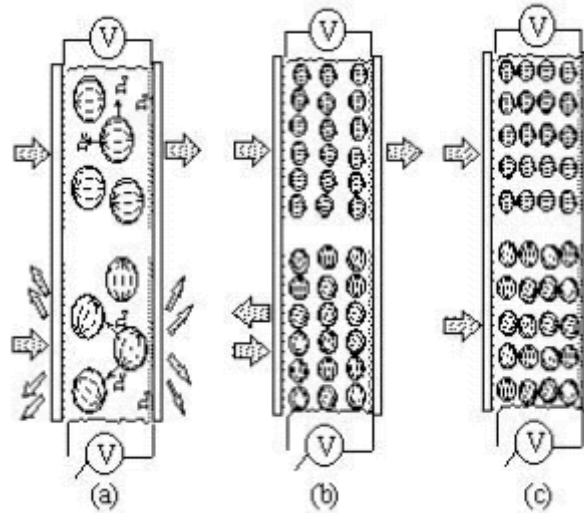


Figure 5. H – PDLC operations

As a result of the holographic processing H-PDLCs contain a periodic array of liquid crystal droplets and solid polymer planes, Figs. 5b and c. H-PDLCs may reflect (Fig. 5b) or diffract (Fig. 5c) various wavelengths and upon application of an applied voltage the reflection or diffraction is eliminated to make the materials transparent. The reflection or diffraction wavelengths are determined by the cure conditions, and governed by electrical field controlled birefringence. Response times for H-PDLCs are of the order of $\sim 100 \mu\text{s}$.

Acousto – optical tunable filters (AOTFs)

An AOTF consists of a crystal in which radio frequencies (RF) acoustic waves are used to separate a single wavelength of light from a broadband source, Fig. 6. The wavelength of light selected is a function of the frequency of the RF applied to the crystal. Thus, by varying the frequency, the wavelength of the filtered light can be varied. The most common types of AOTFs that operate from the near UV through the short wave infrared region, use a crystal of Tellurium Dioxide (TeO_2) or Hg_2Cl_2 in a so-called non-collinear configuration — the acoustic and optical waves propagate at quite different angles through the crystal. An RF transducer, bonded to one side of the TeO_2 crystal, emits acoustic waves. As these acoustic waves pass through the TeO_2 , they cause the crystal lattice to be alternately compressed and relaxed. The resultant density changes produce refractive index variations that act like a transmission diffraction grating or Bragg diffracter. Unlike a classical diffraction

grating, however, the AOTF only diffracts one specific wavelength of light, so that it acts more like a filter than a diffraction grating. This is due to the fact that the diffraction takes place over an extended volume, not just at a surface or plane, and that the diffraction pattern is moving in real time. The diffracted light intensity is directed into two first order beams, termed the (+) and (-) beams, orthogonally polarized, both of which are utilized in certain applications. To use the AOTF as a tunable filter, a beam stop is used to block the undiffracted (zero order), broadband light and the (+) and/or (-) monochromatic light is directed to the camera. The angle between the beams is a function of device design, but is typically a few degrees. The bandwidth of the selected light depends on the device and the wavelength of operation, and can be as narrow as 1 nm FWHM. Transmission efficiencies are high (up to 98%), with the intensity divided between the (+) and (-) beams. AOTFs can also be of collinear type depending on the AO crystal used to fabricate the cell (typically with crystals such as quartz, lithium niobate, etc.), where the incident and diffracted light and acoustic waves travel in the same direction. The polarization of the incident and diffracted beams are orthogonal, and the two beams are separated by using a set of polarizers.

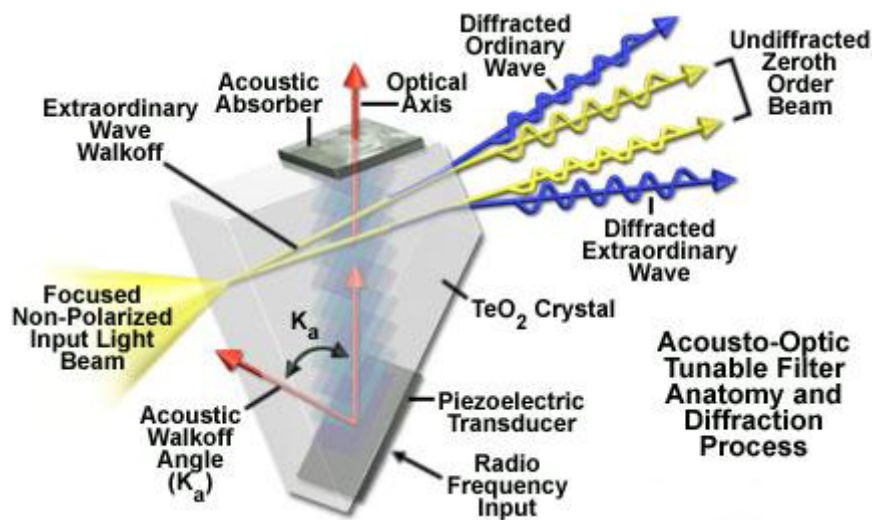


Figure 6. AOTF operations

Underlying Principles of AOTF Operation

An acousto-optic crystal is defined as having optical properties that are altered in the presence of an acoustic wave. When an acoustic wave propagates through such a material, the crystal lattice structure is alternately compressed and relaxed in response to the oscillating wavefront. The basic mechanism responsible for this

acousto-optic interaction is known as the elasto-optic effect. Periodic regions of lattice compression and rarefaction throughout the crystal are manifested as refractive index fluctuations that can produce diffraction of incident light. Although the function of the acousto-optic tunable filter is similar to that of a diffraction grating, its behavior differs in that diffraction occurs over an extended volume of the crystal rather than at a planar surface, and only a limited band of spectral frequencies are affected. In this respect the AOTF performs more as a bandpass filter than a diffraction grating. The propagating acoustic waves generate a periodic modulation of the index of refraction throughout the crystal, effectively producing a mobile phase grating, which will diffract portions of the incident light that satisfy appropriate phase-matching (or momentum-matching) conditions. For a particular acoustic frequency, only a limited range (band) of spectral frequencies satisfies the phase-matching condition, and becomes diffracted. Varying the radio frequency driving the piezoelectric transducer changes the center of the spectral pass band, as required to maintain the phase-matching condition. Appropriate selection of the drive frequency allows the crystal to be tuned to separate a particular wavelength band for diffraction, which then exits the crystal at a distinct angle relative to the undiffracted beam.

The diffracted wavelength(s) vary as a function of the radio frequency signal applied to the crystal. For a specific set of AOTF design parameters (including crystalline material and geometry), the central wavelength (λ) of the pass band is determined by the phase-matching (and momentum-matching) condition defined by the following equation:

$$\lambda_{\text{center}} = \mathbf{V} \cdot \Delta\mathbf{n}/\mathbf{f}$$

In the preceding equation, \mathbf{V} is the acoustic wave velocity, $\Delta\mathbf{n}$ is the birefringence of the acousto-optic crystal, and \mathbf{f} is the acoustic wave frequency. The amplitude of light waves transmitted in the diffracted beam is proportional to the radio frequency power applied to the crystal. Consequently, varying the frequency and power of the RF signal provides a mechanism for selecting the wavelength and intensity of the light filtered by the AOTF.

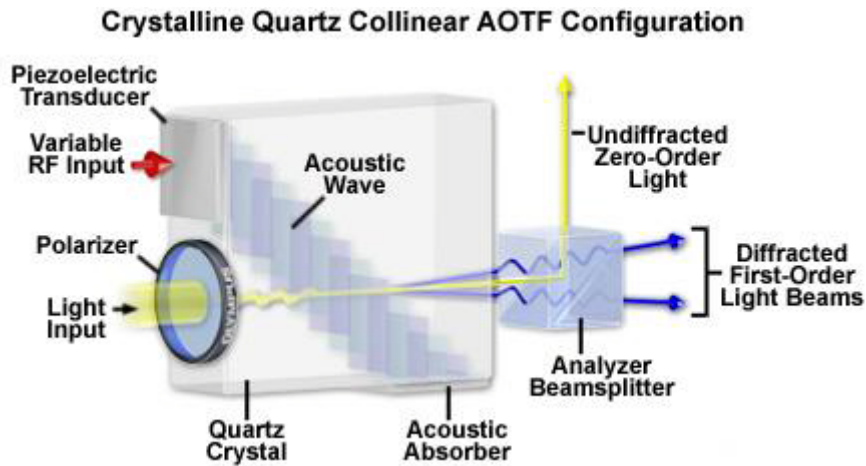


Figure 7. Crystalline Quartz Collinear AOTF Configuration

The initial AOTF design centered on a configuration in which the interacting acoustic and optical waves are collinear, as illustrated in Figure 7. In this design, the acoustic wave is launched along a principal axis of the crystal, and the incident optical beam passes through a polarizer and follows the same propagation path along the crystal axis, interacting collinearly with the acoustic waves (Figure 7). A narrow band of spectral wavelengths is diffracted into a polarization direction orthogonal to that of the incident beam, and can be separated from the coupled collinear beams by an output polarizer (Analyzer Beam splitter, Figure 7). As described previously, the center of the wavelength pass band is determined by the phase-matching condition that exists between optical and RF signal frequencies.

The collinear AOTF geometry is restricted to use with a limited category of crystals, which unfortunately does not include some of the most efficient acousto-optic materials. In order to take advantage of the benefits from materials such as tellurium dioxide, and to utilize a geometry that is simpler to fabricate, a configuration in which the acoustic and optical waves are non – collinear was developed (Figure 6. In this design, the narrowband diffracted light and incident broadband light is physically separated, and because they exit the crystal through different pathways, polarizers are not required for operation. The zeroth-order undiffracted beam can be blocked by a beam stop, while the filtered diffracted beam is utilized for specimen illumination. A phenomenon referred to as acoustic walk-off is illustrated in Figure 6 by the angular difference between the acoustic group velocity and the normal to the acoustic wavefront, a variance that is common to many acousto-optical devices.

The significance in a collinear AOTF configuration (Figure 7) is that although the direction of light propagation and the acoustic phase velocity are by definition collinear, the resulting acoustic group velocity follows a slightly different angle.

When a non-polarized incident light beam is employed in the non – collinear configuration (illustrated as a focused light cone in Figure 6), the diffracted portion of the beam comprises two spatially separated first-order beams, which are orthogonally polarized. If the input beam to the AOTF is linearly polarized (as with a laser source), only one diffracted beam exits the device, with its polarization state rotated 90 degrees relative to the input polarization axis. Because the two orthogonally polarized first-order beams do not separate until they leave the crystal, and then diverge at a fixed angle, the diffraction angle (and spatial location of the resulting image) does not change with wavelength. In applications that utilize the non – collinear AOTF as a tunable filter, the first-order diffracted component is allowed to illuminate the specimen (typically only one diffracted output is used), while the zeroth-order beam is blocked. The two beams are typically separated by a few degrees, which is a function of the device design. By utilizing crystals having larger birefringence values, this deflection angle (the angle separating the diffracted and undiffracted beams) is increased, a desirable property for achieving adequate separation between the diffracted and undiffracted beams without using polarizers. The deflection angle taken by the diffracted beam is at a minimum for the tellurium dioxide crystal system when the beam incidence angle is parallel to the [110] axis (at 90 degrees to the optical axis), and increases up to a practical limit between 8 and 9 degrees as the incidence angle increases with respect to the [110] axis. The deflection angle occurring between the diffracted and undiffracted beams after leaving the crystal has the following relationship to the birefringence of the crystal material:

$$\theta_i - \theta_d = \Delta n \sin 2\theta_i$$

In the expression above, $\theta(i)$ and $\theta(d)$ are the angles, relative to the optic axis, of the incident and diffracted beams, respectively. The birefringence is represented by Δn . AOTF devices based on the collinear mode of operation, such as those utilizing quartz as the birefringent material, can be considered a simplified variation of the non – collinear design with an incidence angle, $\theta(i)$, of 90 degrees, and a deflection angle of zero.

Although in principle, both isotropic and anisotropic Bragg diffraction patterns can be exploited as mechanisms for spectral filtering, a critical limitation exists in the use of isotropic filter media, because the spectral pass band varies with the incident light angular aperture, and therefore a well-collimated beam is essential. The effect of angular aperture on pass band properties results from the fact that changes in the incidence angle produce momentum mismatches, causing the diffracted beam to be deflected differently for each wavelength. For a divergent incident beam, the optical pass band width is dramatically increased compared to that for a collimated beam, severely limiting the practical angular aperture of the filter.

The anisotropic acousto-optic filter has the practical advantage that a narrow pass band can be maintained over a large range of incident beam angles. With this design, the polarization plane of the diffracted beam is rotated 90 degrees relative to the undiffracted beam polarization direction. Because the refractive indices experienced by the ordinary and extraordinary rays in a birefringent crystal are unequal, the acoustic wave propagation direction can be chosen to cause the group velocity for the incident and diffracted light to be collinear (a condition referred to as noncritical phase matching). In this situation, the momentum mismatch produced by the angular variation of the incident light beam is maximally offset by the angular change due to birefringence. Since the noncritical phase matching condition is satisfied over a large range of incident beam angles, the angular field of view for a non – collinear AOTF can be relatively high, while maintaining desirable properties, such as a narrow pass band.

Materials for AOTF Fabrication

The significant increase in the number of applications utilizing acousto-optic devices in recent years has largely occurred due to the development of improved materials for their fabrication. The selection of an appropriate material depends on the specific device target function. For example, gallium phosphide has superior characteristics for construction of wideband acousto-optic deflectors and modulators, but because the crystalline structure is optically isotropic, the material is not suitable for tunable filter devices. Specific general requirements, however, pertain to any type of optical device, and these include high optical transparency over the wavelength range to be utilized, availability in sufficiently large single crystals, and reasonable cost, among other factors. One useful variable for evaluating a material's performance is a factor referred to as the acousto-optical figure of merit, as appropriately defined for the particular device type. The literature presents at least five different expressions for calculating figure of merit, each employing variables considered relevant to particular device functions. Parameters typically considered include index of refraction, density, acoustic wave velocity, bandwidth, resolution (defined by a variety of methods), and a range of elasto-optic coefficients. The specific variables that must be optimized in AOTF design are diffraction efficiency, wavelength resolving power, and solid angular aperture. Regardless of the equation employed for its calculation, any figure of merit is generally stated as a dimensionless value normalized to the appropriately determined absolute value for fused silica.

Typical Specifications for Non – collinear and Collinear AOTFs

Specification	Noncollinear (Tellurium Dioxide)	Collinear (Quartz)
Wavelength Tuning Range	0.38 - 5.5 mm	0.2 - 1.0 mm
Acoustic Tuning Range (Single Transducer)	1 octave	1 octave
Optical Aperture	0.1 - 1.5 cm ²	0.1 - 5.0 cm ²
Solid Angular Aperture	5 - 15 degrees	2 - 5 degrees
Deflection Angle ($q_i - q_d$)	3 - 9 degrees	0 degrees
Diffraction Efficiency (Polarized Light Input)	10 - 90 percent	20 - 90 percent
Tuning Speed	4 - 20 msec	14 - 35 msec
Extinction Ratio	greater than 1000	greater than 1000
Input RF Power	0.5 - 3 watts	5 - 30 watts
Input RF Frequency	20 - 200 MHz	50 - 220 MHz
Piezoelectric Transducer Material	LiNbO ₃	LiNbO ₃

Based on its many favorable properties, and the resulting high acousto-optic figure of merit, tellurium dioxide is currently the preferred AOTF material. The first reported experimental demonstration of the non – collinear mode in AOTF operation

was performed using a tellurium dioxide crystal operating in the visible spectral region. The device described is capable of tuning an output wavelength range of 700 to 450 nanometers (pass band center) by varying the RF drive frequency from 100 to 180 megahertz. The diffraction angle of the filtered beam relative to the incident beam is about 6 degrees, with nearly 100 percent of the incident light being diffracted at a drive power of 120 milliwatts.

Tellurium dioxide is functional throughout the visible spectrum and into the infrared up to approximately 5.5 micrometers wavelength, and has a short wavelength transmission cutoff at approximately 350 nanometers. In order to extend the AOTF usable range into the deep ultraviolet or further into the infrared, another material must be employed. After the initial development of tellurium dioxide devices, crystalline quartz was used to broaden the operating range into the ultraviolet, and further extension into the infrared region has been accomplished with thallium-arsenic-selenium crystals. Expanding the spectral range attainable with AOTFs is primarily limited by the availability of materials that perform efficiently and at high transparency in the desired wavelength bands.

As previously discussed, because of the limited number of crystal classes suitable for collinear AOTF operation mode, significantly more effort has been concentrated on developing materials for non – collinear devices. Performance specifications are reported in the literature for non – collinear AOTFs employing a variety of materials, including tellurium dioxide, thallium-arsenic-selenium, and mercuric chloride for operation in the infrared (up to approximately 11 micrometers wavelength). AOTFs for tuning in the ultraviolet spectral region have been fabricated from crystalline quartz, magnesium fluoride, and sapphire (aluminum oxide). Crystalline quartz is the preferred material for operation in the ultraviolet region. Because the acousto-optic figure of merit for quartz is only about 0.002 that of tellurium dioxide, quartz-based AOTFs perform with lower diffraction efficiency and require perhaps ten times higher power values to drive the RF transducer, in comparison to a tellurium dioxide filter.

Operations in the long wave infrared (LWIR) require special materials operating at cryogenic temperatures. TAS (Tl_3AsSe_3) is one material of choice, although difficult to work with due to cryo – cooling requirements.

Interferometers

A number of interferometers have been used as ETF in similar applications. These devices produce an extremely high spectral resolution and may be more appropriate for gas/plume detection tasks. A Fabry-Perot filter is simply an optical resonator, consisting of two planar partial reflectors spaced by a fixed distance. Light incident

on the device must satisfy a resonance condition, representing a standing wave in the cavity, in order to be efficiently transmitted. Thus, the ideal transmission spectrum is a periodic function consisting of narrow resonant bands that efficiently transmit, separated by broad bands with strong rejection. The rejected non-resonant light is back reflected by the structure.

Free Spectral Range

Management of this light by the optical system is key to achieving high performance. The periodicity of the spectrum, or free spectral range (FSR), depends only upon the separation of the mirrors, with period increasing as the mirrors are moved together. The width of the spectral band satisfying the resonance condition specified by the full-width-half-maximum (FWHM), narrows as the mirror reflectivity is increased. Likewise, the degree of blocking (or rejection) increases with reflectivity.

The transmission function for the ideal lossless Fabry-Perot filter is determined by the round-trip phase of the cavity, ϕ , and the mirror reflectivity, R .

$$T = \frac{1}{1 + \frac{4R}{(1-R)^2} \sin^2 \phi}$$

where

$$\phi = \frac{2\pi n l \cos(\theta_i)}{\lambda},$$

and where n is the refractive index of the liquid crystal, l is the cavity length, and θ_i is the angle of incidence.

The periodicity of the spectrum, or free-spectral-range (FSR), is inversely proportional to the separation of the mirrors and is independent of the mirror reflectivity,

$$FSR = \frac{\lambda^2}{2nl}.$$

The plot below shows how the FSR varies with wavelength for various cavity thicknesses (2 μm , 4 μm , etc.).

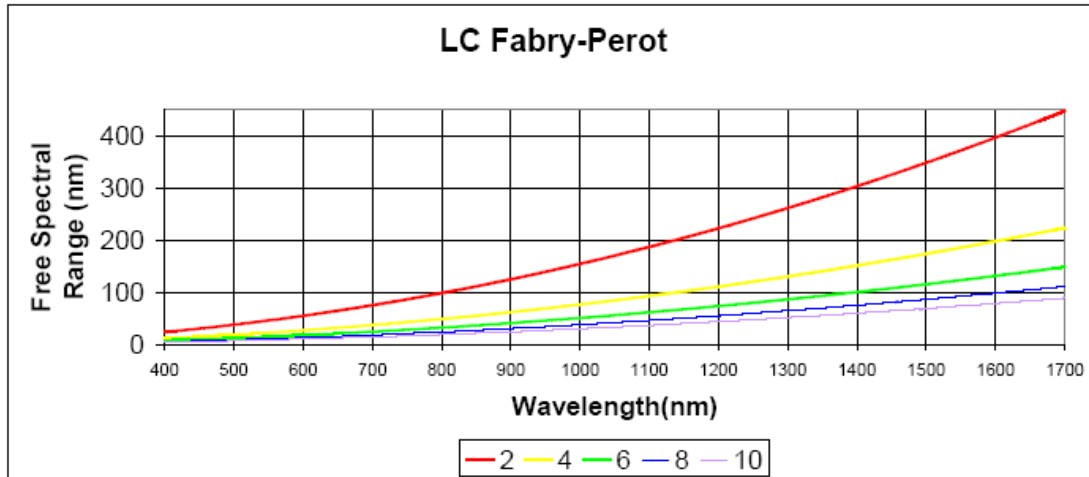


Figure 8.

The resolution of the spectral band satisfying the resonance condition, often specified by the fullwidth-at-half-maximum (FWHM), is proportional to the FSR and a factor that depends solely on reflectivity of the mirrors:

$$FWHM = \frac{(1-R)}{\pi\sqrt{R}} FSR.$$

The coefficient of the above equation is the inverse of the filter finesse, or number of wavelength channels in a spectral period. The above assumes ideal performance, termed the "reflective finesse" condition of the filter, and is a situation highly sought in fabrication. Figure 9 below shows the relationship between FSR and resolution at various reflectivities.

In actuality, defects and the ever-present cavity losses, however small in a single pass, determine the upper limit of performance. It is therefore extremely important that the optical losses be minimized when implementing high finesse filters. Mirror flatness, parallelism and RMS roughness must all be taken into consideration when attempting to achieve reflective finesse over the desired clear aperture.

The Liquid Crystal tunable Fabry-Perot filter is a hybrid device that combines the F-P structure with LC technology. The LC tunable F-P filter is an electro-optical device. The transmission mode can be tuned by changing the optical path length of an intra-cavity material. This is ideally accomplished using a material with a voltage dependent refractive index, allowing rapid electronic wavelength selection. In this case, tunability is accomplished using a specific LC alignment, which induces the anisotropic molecules to "stand-up" in the presence of an applied AC field.

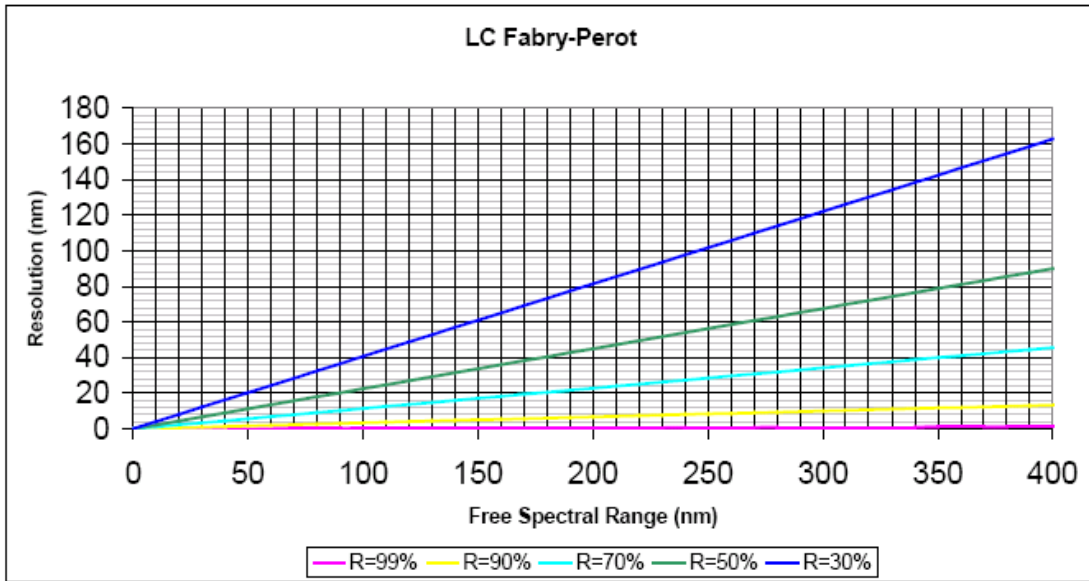


Figure 9.

In order to shift the resonance wavelength through an entire period, (full FSR of tunability), a single-pass optical path length change of $\lambda/2$ is required. In other words, full-tunability requires an analog optical phase shifter with a 180° phase modulation within the cavity. In light of the large FSR required, one might assume that a decrease in cavity width would increase the tuning range. However, the tuning range of the filter is given by

$$\Delta\lambda \approx \frac{\lambda}{n} \Delta n.$$

The important thing to note here is that the tuning range is independent of the cavity width, simply requiring a large percentage change in refractive index of the nematic LC(see figure 10).

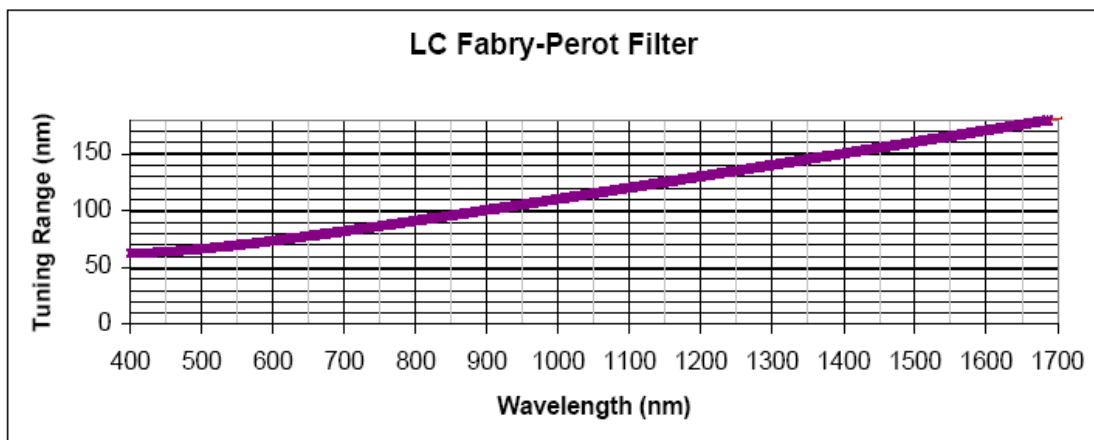


Figure 10.

Tunable liquid crystal based Fabry-Perot filters are suitable for applications requiring reasonable pass band widths ($> 3\text{nm}$). These solid-state devices are attractive alternatives to mechanically rotating filter wheels. The tuning range of these devices can be 60-80 nm in the visible or 120 – 160 nm at telecom wavelengths. Their analog tuning capabilities and large clear aperture make these filters especially suitable for spectroscopic imaging applications

Linear Variable Filters (LVFs)

A Linear Variable Filter (LVF) is a bandpass filter coating that has been intentionally wedged in one direction. Although non tunable, is also a useful spectral imaging device. Since the bandpass' center wavelength (CWL) is a function of the coating thickness, the peak wavelength transmitted through the filter will vary in a linear fashion in the direction of the wedge. The variation in CWL can be maintained to within $\pm 0.5\%$ of virtually any monotonic function (e.g. linear or logarithmic).

A specific wavelength may be selected by simply adjusting the filter to the appropriate linear position. Movement of the filter in front of a source, or raster scanning, will provide a continuous rapid scan of the total wavelength range of the filter.

The LVF coating can be manufactured in any wavelength range from $\sim 300\text{ nm}$ in the VIS region of the spectrum up to $\sim 20\ \mu\text{m}$ in the IR. The specified wavelength range for a typical LVF is $\sim 2\times$ the beginning wavelength of the filter. For example, if the required starting wavelength of the LVF is 380 nm, the ending wavelength can be $\sim 760\text{ nm}$. The LVF design allows multiple filters to be placed together to provide wavelength coverage greater than 2:1 spread.

The resolution of LVFs has typically been specified between 1-2% of CWL. Higher (or lower) resolutions are possible. In a specific instance, an LVF with 0.005% resolution was produced, corresponding to $\sim 1\text{\AA}$ in the NIR. LVFs are also easily customized to meet specific resolution requirements for particular applications.

Fourier Transform Spectrometers (FTS) have been used in imaging modes often, though, with a small number of spatial pixels. Various forms of Fabry-Perot (F-P) etalons and liquid crystal F-P (LCFP) have been used in imaging spectrometry. Micro electro manufacturing (MEM) technology promises small scale integration of F-P or FTS filters on a chip, simplifying the overall sensor design. Other application specific imaging techniques worth mentioning, include the Shearing Interferometer, pressure modulated gas filtering, and gas correlation spectroscopy.

Tunable filters commercial applications

VariSpec

The VariSpec™ LCTF is like a high-quality interference filter, but the wavelengths of the light it transmits are electronically controllable, providing rapid, vibrationless selection of any wavelength in the visible and near-infrared tuning ranges. The VariSpec™ filter's unlimited wavelength selection and excellent image quality are particularly valuable in a wide variety of applications such as remote sensing, airborne hyperspectral imaging, Raman chemical imaging, and process quality control.

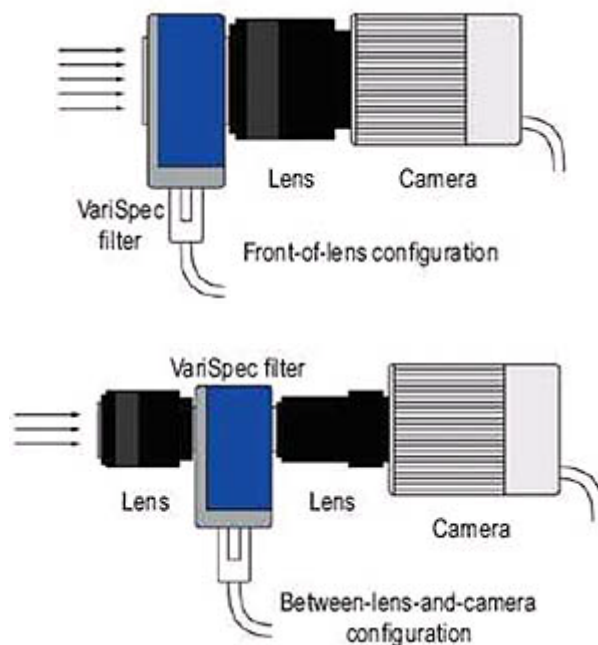


Figure 11.

Figure 11 above demonstrates how VariSpec™ can be used in the various applications. The polarized transmittance is shown below (figure 12). As we can see, below the 500nm wavelength the transmittance is lower than 30% and at 400nm is as low as 2%.

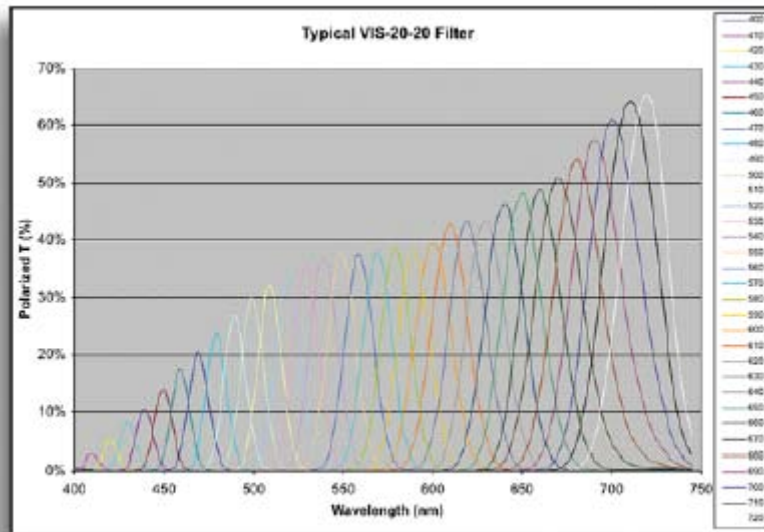


Figure 12.

Gooch & Housego

Gooch & Housego provide Tellurium Dioxide AOTFs at many different spectral ranges.



Figure 13.

In figure 13 we have a medium size AOTF that allows the use at microscopes and endoscopes. Its spectral range is one octave and its resolution can be 0.1% of the tuned wavelength. This indicates the fact that spectral resolution is not the same along its tunable range. Another feature of the AOTFs is the existence of side lobes of the tuning signal. The result of these side lobes are chromatic aberration and acousto-optic blur.

SpectralView^R

SpectralView^R is a HySIS that uses an interferometer for spectral imaging with direct view for a CCD camera. It's spectral range extends from 400nm to 1000nm. Sensitivity below 450 and above 780nm is significantly reduced in this system too. It's spectral resolution (FWHM) is <5nm at 400 nm, <20nm at 780 nm, user selectable (250 cm⁻¹ in all range). The FFT process time is about 5 seconds, depending on the size and resolution of the spectral image and so unsuitable for real time applications. Figure 14 demonstrates a SpectralView^R HySIS on a microscope.



Figure 14. SpectralView microscope example

Each system showed previously represents a different technology and approach to hyperspectral imaging.

Chapter 4

Introduction to image enhanced endoscopy

Endoscopy has evolved over the last 50 years in such a way, that it has change the way gastrointestinal diseases are managed by the physicians. Since Nitze first used electrical illumination in his pioneering rigid endoscope in 1888, the introduction of the fiberscope by Hirschowitz and Curtis in 1958 and the introduction of the video endoscope by Sivak and Fleischer in 1984, many innovations have occur. The collaboration between physicians and engineers has enabled the incorporation of novel technologies into the field of endoscopy to provide improved diagnostic and therapeutic performance.

Standard video endoscopy is been used broadly as a diagnostic procedure. Video sensors of 0.1 to 0.3 megapixels are used with the conventional endoscopes, achieving an x5 magnification. For illumination a cold, white light source is utilized, usually integrating a Xenon light bulb. The performance of these systems is highly dependent to the skills of the operator, his clinical experience and his analyzing and detecting skills.

Conventional white light endoscopy is associated with a disproportionate miss rate for subtle lesions (e.g. flat adenomas). Numerous studies have demonstrated that experienced gastroenterologists miss up to 6% of advanced adenomas and 24% of all adenomas. Certain endoscopic techniques are associated highly with missed lesions. Therefore, the present and future directions of endoscopy are to improve the diagnostic techniques through monitoring adenoma detection rates, withdrawal time with better education and practice improvement interventions. However, subtle dysplastic and early neoplastic lesions remain often too small, flat or depressed to be detected during regular standard white-light endoscopy even with ideal (improved) techniques. This has led to intensified efforts to develop other alternative, optically based techniques as well as other diagnostic modalities that would compete with and/or be complementary to existing conventional endoscopic methods in the detection of subtle lesions.

Novel diagnostic Advances in Endoscopy

Imaging enhanced technologies that are currently available in endoscopy include field enhancement techniques such as chromoendoscopy, auto fluorescence imaging (AFI) narrow band imaging (NBI) and digital image processing (like FICE and i-Scan), as well as point enhancement techniques, such as high definition television (HDTV) endoscopy and confocal laser endomicroscopy (CLE). These enhancements offer improved visualization of lesions and/or abnormalities, which, in turn, may provide

guidance in determining optimal treatment. Currently, endoscopes with integrated zoom lenses and probe microscopes small enough to be passed through the accessory endoscopic channel are available. With these add-ons, intestinal tissue can be visualized at a cellular or sub cellular level and may be able to provide in vivo optical histology. Endoscopic systems that are equipped with field enhancement modes accommodate high resolution optical sensors and provide high-magnification capabilities and improved image quality. High resolution endoscopes with high-density charge coupled device (CCD) provided resolutions from 0.6 up to 2 megapixels (HDTV systems) and produce high magnification images for the detection of microscopic abnormalities in tissue. They provide image enlargement up to 120 times compared with 30 times with standard endoscopes. In this paper the above mentioned novel endoscopic imaging enhancement technologies will be reviewed and a new approach for enhanced image in hysteroscopy will be presented.

Chromoendoscopy

Chromoendoscopy involves the topical application of stains or pigments to impose tissue localization, characterization or diagnosis during endoscopy. This image enhancement method has been applied in a variety of clinical settings and throughout all gastrointestinal tract segments that are accessible to an endoscope, as the equipment needed is widely available and the staining techniques are simple, inexpensive and safe. Examples of stained tissues are in Figure 1. Interest has been renewed in recent years in part because of the development of new technologies such as endoscopic mucosal resection and photodynamic therapy, which require precise visual tissue characterization. However, staining of the entire mucosa is a time consuming process. Thus, efforts have been made to develop so-called virtual chromoendoscopy with the use of narrow band imaging or the Fujinon intelligent color enhancement system (FICE) to enhance mucosal contrast with no requirements for the use of topical stains. Like many endoscopic techniques, the impact of chromoendoscopy on clinical outcomes relative to standard endoscopic and histological methods has not been established in large controlled trials.

Auto fluorescence Imaging (AFI) Endoscopy

Living tissues contains proteins that emit auto fluorescence when exposed to proper wavelength of light (ultraviolet and blue). Many devices have been manufactured and patented for auto fluorescence endoscopy, initially for bronchoscopy. The principle of operation is simple: a powerful ultraviolet or blue light source is used to excite the living tissue and a video camera module, featuring one very sensitive optics sensor (e.g. a CCD) filtered to observe only the excitation spectrum and another for conventional endoscopic images. Deuterium lamps were initially utilized as excitation sources but soon were replaced by lasers coupled with a conventional white light source. Lasers have numerous advantages as they offer very high

intensity, narrow monochromatic illumination and a variety of wavelength available. The recent advances in semiconductor technologies have provided small size powerful blue lasers (at 405nm wavelength) that have allowed the designers of the endoscopes to integrate the laser at the tip of the endoscope. Also CMOS image sensors have been manufactured especially for endoscopic applications with dimensions that enable the placement of two image sensors at the end tip of many endoscopes.

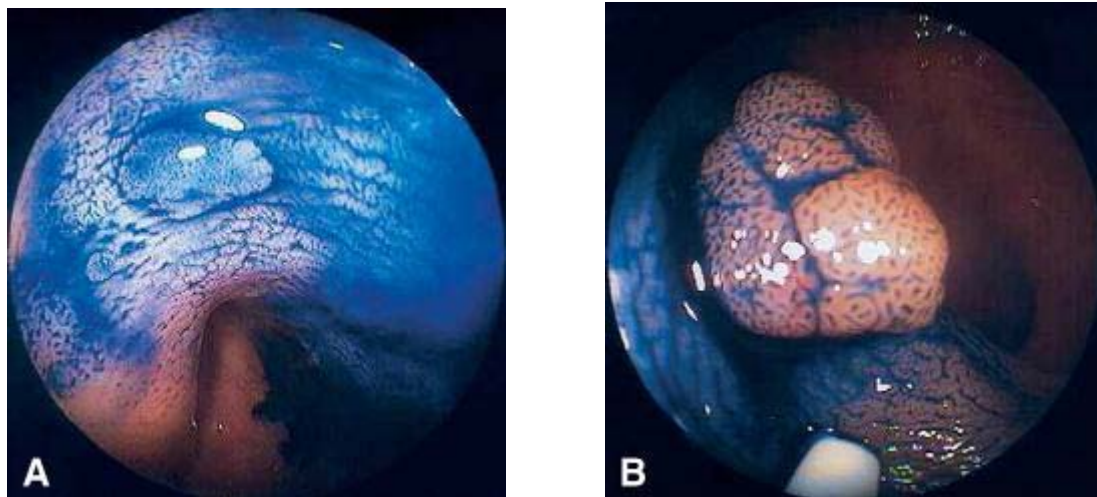


Figure 1. A, Colonoscopic view of hyperplastic polyp. **B,** Colonoscopic view of adenomatous polyp. In both cases tissue was stained with 0.9% indigo carmine dye.

(From Eisen GM, Kim CY, Fleischer DE, et al. High-resolution chromoendoscopy for classifying colonic polyps: a multicenter study. Gastrointest Endosc 2002;55:687-94.)

Olympus, in order to provide better image enhancement in its endoscopic high range systems “EVIS LUCERA SPECTRUM”, utilizes a 540-560nm reflectance image along with the 390-470nm excitation image. The pseudo color AFI image displayed to the user is created by assigning the auto fluorescence image to the Green Color plane of the pseudo color image and the reflectance image to the Red and Blue Color planes (Figure 2). Other companies use similar concepts for better visualization of the fluorescent tissue.

The common fluorescence substances in the living tissue include amino acids like NADH, flavin, and collagen richly found in the connective tissue. Several investigators have reported studies of auto fluorescence from living tissue. Although efforts in such studies, relationship between the auto fluorescence and the malignancy of the lesion is not still unclear in several tissue types. Gono K. et al. also investigated auto fluorescence spectra of the living tissue. A spectroscope was used and attached to it was an optical fiber probe compatible for an instrumental channel of the endoscope body. Several auto fluorescence spectra from normal colon tissues and adenomas were selected.

A recent multi-centre study by Curvers et al investigated the diagnostic potential of endoscopic tri-modal imaging including autofluorescence imaging (AFI) as well as high resolution endoscopy , and narrow band imaging (NBI) for the detection of early neoplasia in Barrett’s esophagus. The investigators noted that the addition of AFI to high resolution endoscopy increased the detection of both the number of patients and the number of lesions with early neoplasia in patients with Barrett’s esophagus. Furthermore, the initial false positive rate of AFI was reduced after detailed inspection with NBI. The results of this study demonstrate the promising role of prototype endoscopic systems combining the use of AFI and NBI technologies in one endoscope.

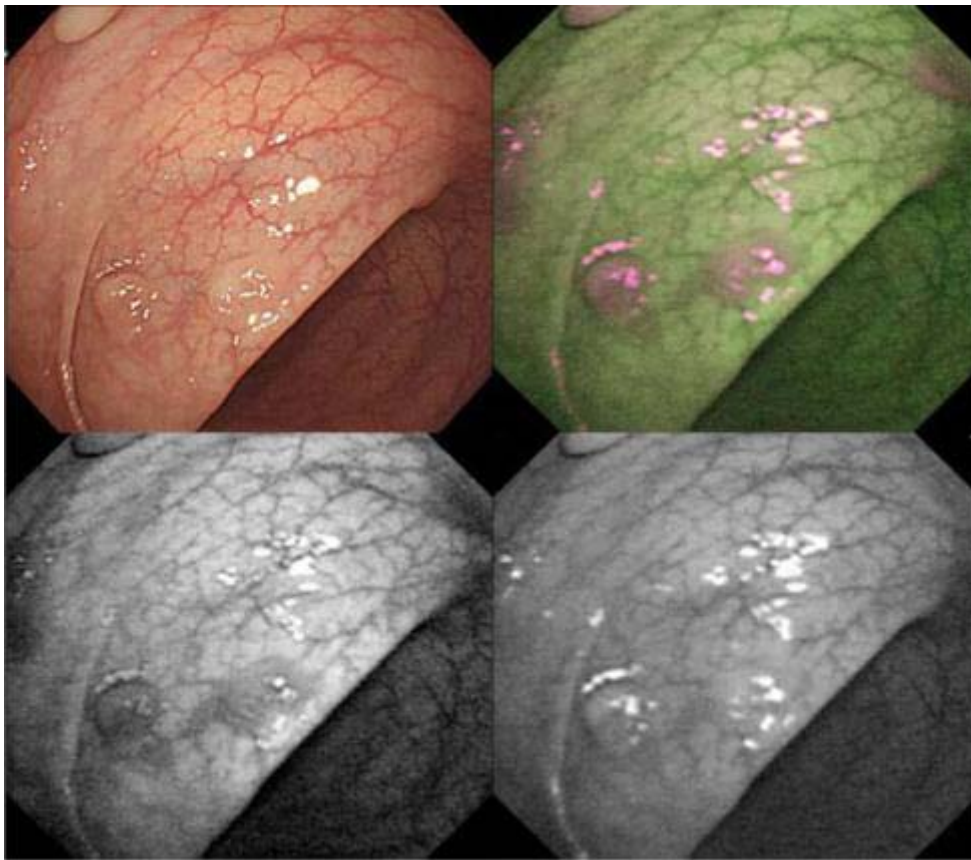


Figure 2. AFI image of colon polyps. Upper left is white light image. Upper right is AFI pseudo color image. Both right is the green channel reflectance image and bottom left the fluorescence image.

Moreover, colonic autofluorescence has also been described both at glandular and cellular level and appears to be promising. In the studies by DaCosta et al dysplastic and adenomatous epithelial cells had much higher autofluorescence and contained numerous highly auto fluorescent lysosomal granules. Epithelial autofluorescence may be helpful in distinguishing hyperplastic and adenomatous lesions.

Narrow band Imaging (NBI) Endoscopy

Narrow Band Imaging was developed by Olympus as an optical image improvement technology that enhances vessels in the surface of the mucosa. In the NBI endoscopic system, RGB and bandpass filters are rotated in front of a Xenon lamp to provide illumination to generate either a traditional RGB image or a narrow band wavelength pseudo color image. As the illumination changes sequentially with the rotating filters, a CCD detects each image. Next, an image processor produces color images by composing the images acquired. If the filters are the common RGB filters, the image produced is equivalent with that captured by a color (RGB) CCD camera. However, it is *difficult* to see information that appears in a specific wavelength. For that reason, the narrow band pass filters used in NBI systems are selected in the blue filter wavelength and designed to correspond to the absorption spectrum of the hemoglobin. Also, because blue light penetrates into the superficial-most layers, the mucosal pattern is highlighted, whereas the deeper layers are not seen.

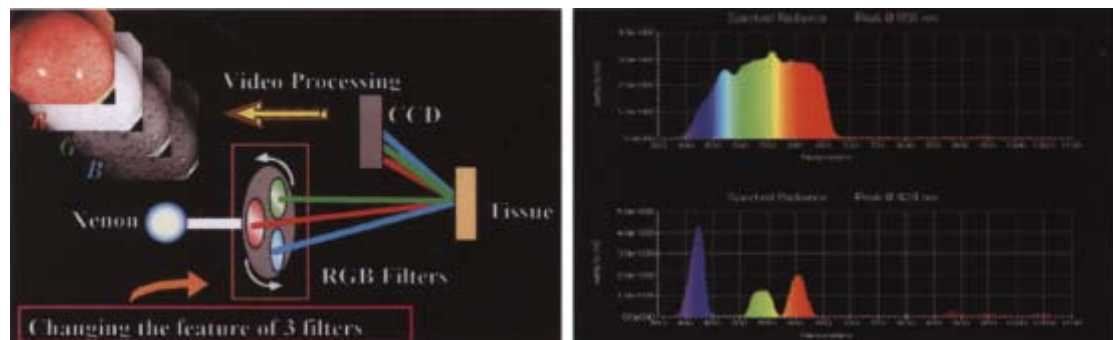


Figure 3. NBI image acquisition process (left) and NBI optical filter properties (right bottom).

The initial designs of the NBI systems incorporated three bandpass filters, one at 415nm, the second one at 540nm and a third at 600nm. Each image captured was assigned to the responding channel of the pseudo color NBI image (Figure 3). In another initial NBI system (EVIS 240; Olympus Co Ltd) a xenon lamp and rotation disk with 3 broadband filters and three NBI filters at 415nm, 445nm and 500nm were selected to obtain images of the micro-vascular structure. Because 415nm is the hemoglobin absorption band, the thin blood vessels such as capillaries on the mucosal surface can be seen most clearly on this wavelength. The latest designs though use only the first two bandpass filters at 415nm and 540nm.

Early studies have demonstrated the value of this technology in the evaluation of patients with upper GI lesions including Barrett's esophagus dysplasia. NBI technology is also useful in the classification of colorectal lesions as many researchers have demonstrated. However, a few recent studies have revealed conflicting results with no improvement in adenoma detection rates with the use of

this novel technique. The results of Gross et al prospective randomized back-to-back trial comparing narrow band imaging to conventional colonoscopy for adenoma detection shows that the miss rate for polyps, and for adenomas, may be lower with high definition NBI than for standard colonoscopy. East et al also demonstrated that NBI could play a role in adenoma detection in high risk groups as they found that a second additional examination with NBI doubled the total number of adenomas detected in 62 patients with hereditary non-polyposis colorectal cancer.

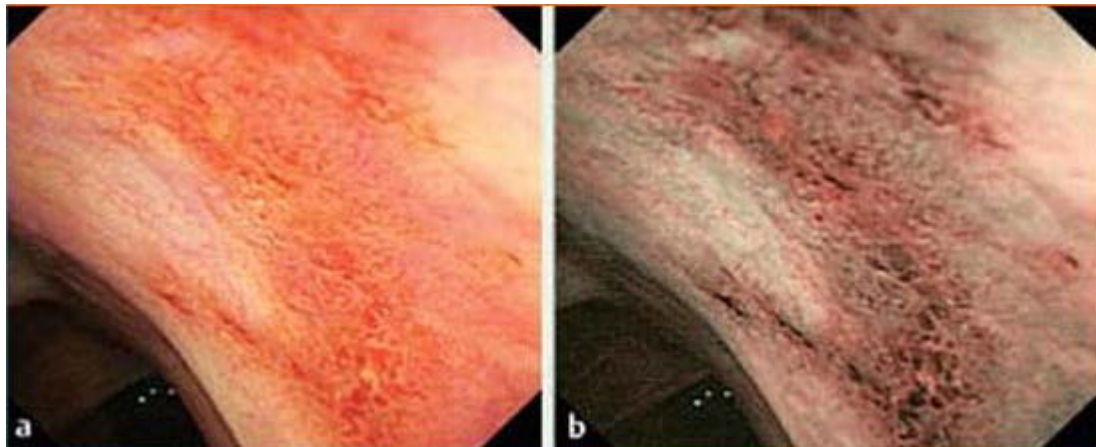


Figure 4. Irregular mucosa with high-grade neoplasia in a patient with long-standing ulcerative colitis. **A**, viewed with white light endoscopy and **B**, by NBI, revealing a Kudo type IV pit pattern.

Fujinon intelligent color enhancement (FICE) and i-Scan endoscopic systems

Eager to provide endoscopic systems with image enhancement technologies, Fujinon and most recently Pentax Medical Company developed all-digital endoscopic systems to provide diagnostic assistance to the physicians. To many researchers these systems are known as computed virtual chromoendoscopy imaging systems, as their aim is to provide similar visual results without staining. While the NBI system depends on optical filters within the light source, the FICE system is based on a computed spectral estimation technology that processes the reflected photons to reconstruct virtual images with a choice of different wavelengths. An RGB image is captured and disintegrated into each color component. Then, and in real time, a digital signal processor performs matrix calculations for each pixel using stored coefficients corresponding to a desired wavelength. After that a pseudo color image is reconstructed featuring one to three selected wavelengths. Various combinations of wavelengths are preset for the user that provide image enhancement for specific areas of interest. This leads to enhancement of the tissue microvasculature as a result of the differential optical absorption of light by hemoglobin in the mucosa. These abnormal areas can be defined by the magnification.



Figure 5. Early gastric cancer as seen with white light (left) and with FICE (right).

The i-Scan system is considered as a digital contrast method, with three modes of image enhancement: surface enhancement (SE), contrast enhancement (CE) and tone enhancement (TE). In SE mode, the structure is enhanced through the detection of the edges and their enhancement. In common endoscopic image sensor systems, minor changes in structure are perceived as noise, and the area that shows such changes is smoothed out from their image processing algorithms. With SE, on the other hand, adjustment of the noise erasure function allows more evident enhancement of the edges, which corresponds to minor changes in structure, making it easier to check changes on the basis of structural differences. With CE mode, areas lower in luminance intensity compared to surrounding pixels are identified from the luminance intensity data of each pixel, followed by relative enhancement of the Blue color channel through the slight suppression of Red and Green color channels in this low luminance area, resulting in slightly a bluish white color of the area applied. Finally, with TE mode the RGB color channels of an ordinary endoscope image are split into each color channel (Red, Green and Blue), and each channel is converted independently along the tone curve, followed by a re-synthesis of the three components to yield a pseudo color image. The tone curve is changed according to the need of the user and provides various modes, depending in the area of application. Sample images can be seen in figure 6.

The FICE system used in esophageal neoplasia demonstrated improvement in the detection of early neoplasia. The application of FICE technology in the detection and classification of colorectal lesions is also being currently investigated. Pohl et al in their prospective trial compared computed virtual chromoendoscopy system (FICE) with other modalities such as standard colonoscopy, conventional chromoendoscopy with indigo carmine in low and high magnification modes for determination of colonic lesion histology. Based on this study, the FICE system was able to identify morphological details that efficiently predicted adenomatous histology and was superior to standard colonoscopy and equivalent to conventional chromoendoscopy. As far as i-Scan endoscopic system is concerned, similar studies are yet available.



Figure 6. Esophageal cancer as captured with an i-Scan system. **A**, the conventional white light image. **B**, SE + CE modes enabled captured image. **C**, TE mode captured image.

Confocal laser endomicroscopy (CLE)

Confocal laser endomicroscopy (CLE) is one of the newest advancements in diagnostic endoscopy. Recent technologic advances allowed for a confocal imaging microscope to be integrated into the tip of a conventional endoscope (Pentax Medical Company), or in a probe, which can be passed through the working channel of the endoscope (Mauna Kea Technologies). The aim of this technology is to provide real-time in vivo histologic images, or so-called “virtual biopsy specimens,” of the GI mucosa during endoscopy. Confocal endomicroscopy allows high resolution imaging of cellular and sub cellular tissue when optical slices of the mucosal surface created by detecting reflected light and tissue autofluorescence enhances through the administration of IV or topical contrast fluorescent contrast agents, like IV fluorescein sodium. Sample images are available in figure 7.

The first report on the use of confocal endomicroscopy was made from Kiesslich et al in 42 patients during ongoing colonoscopy in diagnosing intraepithelial neoplasia and colorectal cancer. A total of 134 small lesions (mean size 4 mm) were identified during colonoscopy after staining with methylene blue. According to the study, intraepithelial neoplasia was predicted with the help of the confocal endoscope with a sensitivity of 97% and a specificity of 99% (accuracy, 99%). The potential applications of this technology extends beyond the discrimination of neoplastic and non-neoplastic (hyperplastic) polyps, to detection of other pathologies such as Barrett’s esophagus, esophagitis, gastritis, coeliac disease, etc. In a study of 63 patients with Barrett’s esophagus using fluorescein-aided endomicroscopy, Kiesslich et al predicted Barrett’s esophagus with a sensitivity of 98% and specificity of 94%. A limitation of the confocal system used in the above studies includes its reliance on a single integrated confocal endoscope. Recently, a miniature probe confocal laser endomicroscopy was developed to overcome that difficulty. At this moment is the world smallest microscope, available through the integration of numerous technological advances in miniature optics, nanomaterials, high speed scanning and advanced real time image processing. This probe can be passed through the accessory channel of almost any endoscope and be used as needed in any endoscopy

case. Becker et al studied 7 patients with various GI pathologies and confirmed that mini probe-based confocal microscopy in conjunction with video mosaicing can provide images similar to standard histopathology. Another concern regarding confocal endomicroscopy is the learning curve of the physicians and the reliable interpretation of the images. Very good knowledge of histopathology is needed for the endoscopist. According to Buchner et al, the interpretation of images is highly reliable among physicians, while the learning curve appears to be rapid among new users, achieving accuracy greater than 80% after 60 cases.

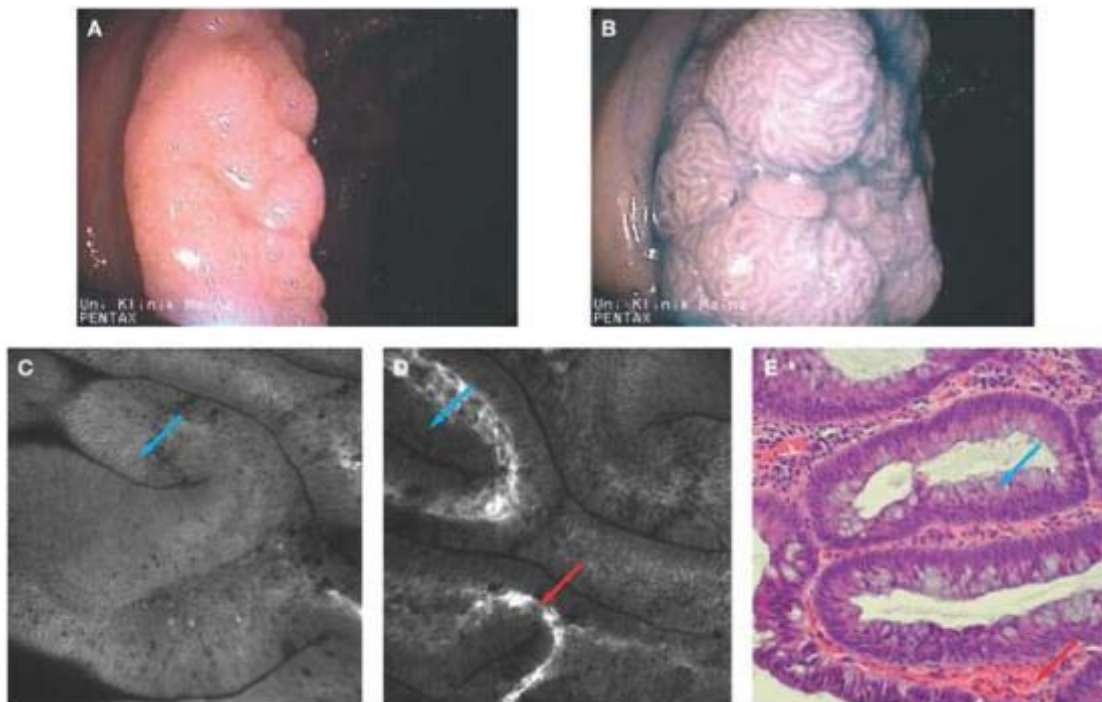


Figure 7. Tubular adenoma with low grade intraepithelial neoplasia (A) Analysis of a colonic polyp with white-light endoscopy, (B) chromoendoscopy, (C,D) fluorescein-based confocal endomicroscopy in different imaging depths and (E) final histology. Chromoendoscopy highlights surface architecture with tubular staining pattern. Endomicroscopy of the surface shows characteristic tubular cellular and tissue architecture (C, blue arrow). At a depth of around 150 μm , subepithelial capillaries become visible (D, red arrow). Final histology (E) confirms the presence of tubular adenoma (blue arrow) with low-grade intraepithelial neoplasia (red arrow).

Clinical Applications

The above technologies combined with high magnification endoscopes are applied in many medical fields such as lung and bronchial system, human tongue, colorectal tissues, cervix and others. The results and the technological background are presented below.

Early cancer of the colon

Confocal Endomicroscopy

The classification of colorectal lesions using confocal microscopy was initially described on ex-vivo samples using a reflectance confocal microscope without contrast agents. Since then, there have been several in-vivo evaluations of colonic lesions using confocal endoscopes with fluorescent contrast agents (acriflavine hydrochloride and fluorescent sodium).

In a study by Kiesslich *et al.*, neoplastic changes could be predicted in polyps with a sensitivity, specificity, and accuracy rate of 97.4%, 99.4%, 99.2%, respectively. Since this study, the same group evaluated the combination of methylene blue chromoscopy and confocal endoscopy in 161 patients with ulcerative colitis in clinical remission. By combining confocal with the technique of chromoendoscopy, more neoplasias were detected than with conventional colonoscopy.

A recent feasibility study was performed by Yoshida *et al* with a laser scanning confocal microscope. Unlike the confocal endoscope used by Kiesslich *et al.*, the prototype laser confocal microscope (LCM) described by Yoshida *et al.* was a semiconductor laser at a slightly higher wavelength of 685 nm and did not require a contrast agent. While the images from this pilot study lacked the clarity of those obtained with the confocal endoscope used by Kiesslich *et al.*, the irregular nuclei of cancer cells were visual. While the device's image quality requires refinement and in-vivo, real-time evaluations need to be performed, these preliminary results are encouraging.

NBI in visualizing capillary patterns in colon

An initial evaluation by Gono *et al.* found that NBI was useful for visualizing capillary patterns in early cancers of the colon, and, as such, was complementary to magnification endoscopy. In a study by Machida *et al.*,^[5] NBI was compared with conventional colonoscopy and chromoendoscopy for the ability to differentiate between neoplastic and non – neoplastic lesions. In this pilot study of 34 lesions, NBI and chromoendoscopy had similar sensitivity (100%) and specificity (75%) rates and both techniques were superior to conventional endoscopy (sensitivity 83%, specificity 44%). Not surprisingly, NBI has been shown to be better at evaluating the capillary patterns, and chromoendoscopy the surface pit pattern.

The same group of researchers evaluated NBI in 62 patients with hereditary non-polyposis colorectal cancer to see if a second pass with NBI in the proximal colon could help detect additional adenomas. With NBI, the total number of adenomas increased from 25 to 46, an increase which was statistically significant. The authors

concluded that NBI was helpful in this high-risk population, largely by aiding the detection of flat adenomas which were poorly visualizable on white-light endoscopy.

A recent, randomized, prospective trial compared high-resolution colonoscopy with NBI in 401 patients undergoing screening colonoscopy. In this study, there was no statistically significant difference in adenoma detection rate means with NBI. Thus, further information is needed to determine whether NBI presents an advantage when compared with high-resolution, white light endoscopy in an average-risk population.

Another study was performed with NBI in detecting neoplasias in colorectal lesions. In this study Narrow band imaging (NBI) uses optical filters for red-green-blue sequential illumination and narrows the bandwidth of spectral transmittance. This study aimed to clarify the clinical usefulness of NBI magnification in assessment of pit patterns for diagnosis of colorectal tumors.

Patients and Main Outcome Measurements

A total of 148 colorectal lesions, 16 hyperplasias, 84 tubular adenomas, and 48 early carcinomas were examined and diagnosed histologically. Mean size of lesions was 15.6 ± 7.28 mm. Lesions were observed first under NBI magnification without chromoendoscopy and then under standard magnification with chromoendoscopy, and pit patterns were recorded. Results of NBI magnification were compared with those of standard magnification with chromoendoscopy to assess the clinical usefulness of NBI magnification for diagnosing colorectal neoplasia.

The results were :Correspondence between the two diagnostic methods was 88% (14/16) for type II, 100% (2/2) for type IIIs, 98% (73/75) for type IIII, 88% (7/8) for type IV, 78% (25/32) for type Vi, and 100% (3/3) for type Vn pit patterns. NBI depicted brownish change on the basis of surface capillaries in 6% (1/16) of hyperplasia and 99% (83/84) of tubular adenomas. This difference in color depiction was significant.

Determination of pit patterns of colorectal neoplasias by NBI magnification was nearly the same as that by standard magnification with chromoendoscopy. Furthermore, NBI can distinguish neoplastic and non-neoplastic lesions without chromoendoscopy.

AFI in colonic epithelial cells

DaCosta et al. evaluated autofluorescence on cultures of a variety of colonic epithelial cells. In this study, mitochondria and lysosomes were identified as the main intracellular fluorescent components in all cell types. Normal and hyper-plastic epithelial cells were weakly auto fluorescent and had similar numbers of

mitochondria and lysosomes. Dysplastic or adenomatous epithelial cells showed much higher autofluorescence and contained numerous highly autofluorescent lysosomal granules. This study suggested that epithelial autofluorescence alone may be sufficient to differentiate hyperplastic and adenomatous polyps.

Early diagnosis and detection of Barrett's esophagus

NBI

NBI technology provides detailed images of the mucosal and vascular surface patterns within the Barrett's esophagus segment with high resolution and contrast, eliminating the need for chromoendoscopy. NBI technology relies on using light filters that enrich blue light of a narrow wavelength (415 nm), which is absorbed by hemoglobin allowing visualization of fine vascular patterns. The correlation of NBI-visualized patterns with Barrett's esophagus histology was recently assessed in a feasibility trial by Sharma *et al.*^[15] In 65 Barrett's esophagus patients, the correlation of NBI patterns in a prospective, blinded manner, showed a high sensitivity of the regular ridge/villous pattern (93.5%) for nondysplastic tissue and the irregular pattern (100%) for HGD. Thus, NBI is a tool that could potentially be used for detecting dysplasia using targeted biopsies; further studies in non-Barrett's esophagus and dysplasia enriched populations will be needed in the future to fully evaluate its role prior to its routine use in clinical practice.

AFI

Another enhanced endoscopic mucosal imaging technique that has recently been evaluated is autofluorescence imaging (AFI). AFI makes use of native tissue fluorophores that emit fluorescent light of longer wavelength when excited with light of a shorter wavelength. Normal and neoplastic tissue have some difference in auto fluorescence characteristics that may enable their distinction. Initial studies using a real-time broad-field AFI imaging system have had a disappointingly high false positive rate and attempts to reduce this false positive rate have led to a combination of AFI with additional techniques. Curvers *et al.*^[16••] tested this principle using an endoscopy system that incorporated high-resolution white light endoscopy (HRE; 100×), AFI and NBI in one system. Eighty-four Barrett's esophagus patients were included in this international multicenter study; AFI in combination with HRE served to identify suspicious areas, which were then inspected by NBI. All suspicious lesions were biopsied for blinded histological evaluation followed by random biopsies. AFI increased the detection of high-grade intraepithelial neoplasia (HGIN) from 45 to 90%; the initial false positive rate of AFI after HRE was 81%, which was reduced to 26% by detailed inspection with NBI. Three patients with HGIN, however, were detected solely by random biopsies. Moreover, although NBI reduced the false

positive rate, its role as a confirmatory technique still needs validation in larger prospective studies.

Confocal laser Endomicroscopy

Finally, confocal laser endomicroscopy is another imaging modality that allows subsurface analysis of the Barrett's esophagus mucosa, providing real-time in-vivo histology during endoscopy. In 63 Barrett's esophagus patients, fluorescence-aided confocal microscopy was able to predict Barrett's esophagus-associated neoplasia with a high accuracy of 96.8%^[17] All these imaging techniques require the learning of various mucosal, vascular and glandular patterns and will need to be tested for intra and interobserver variability.

Finally, novel optical enhancement technologies for the early and accurate detection of dysplastic Barrett's along with new endoscopic therapies may lead to improved outcomes among Barrett's esophagus patients.

Human tongue

NBI

This study was performed to examine the usefulness of medical endoscopic imaging utilizing narrow-band illumination. The contrast between the vascular pattern and the adjacent mucosa of the underside of the human tongue was measured using five narrow-band illuminations and three broadband illuminations. The results demonstrate that the pathological features of a vascular pattern are dependent on the center wavelength and the bandwidth of illumination. By utilizing narrow-band illumination of 415 ± 30 nm, the contrast of the capillary pattern in the superficial layer was markedly improved. This is an important benefit that is difficult to obtain with ordinary broadband illumination. The appearances of capillary patterns on color images were evaluated for three sets of filters. The narrow, band imaging (NBI) filter set (415 ± 30 nm, 445 ± 30 nm, 500 ± 30 nm) was selected to achieve the preferred appearance of the vascular patterns for clinical tests. The results of clinical tests in colonoscopy and esophagoscopy indicated that NBI will be useful as a supporting method for observation of the endoscopic findings of early cancer.

Lung cancer –Bronchoscopy

NBI in Bronchoscopy (angiogenic squamous dysplasia)

The use of high magnification bronchovideoscopy combined with narrow band imaging (NBI) for the detailed examination of angiogenic squamous dysplasia (ASD) is investigated. This study was carried out in relation to bronchial vascular patterns with abnormal mucosal fluorescence in heavy smokers at high risk for lung cancer.

Forty eight patients with sputum cytology specimens suspicious or positive for malignancy were entered into the study. Observations by high magnification bronchovideoscopy with conventional white light were made primarily at sites of abnormal fluorescence, and then repeated with NBI light to examine microvascular networks in the bronchial mucosa. The wavelength ranges of the new NBI filter were B1: 400-430 nm, B2: 420-470 nm, and G: 560-590 nm. The microvessels, vascular networks of various grades, and dotted vessels in ASD tissues were clearly observed in NBI-B1 images. Diameters of the dotted vessels visible on NBI-B1 images agreed with the diameters of ASD capillary blood vessels diagnosed by pathological examination.

High magnification bronchovideoscopy combined with NBI was useful in the detection of capillary blood vessels in ASD lesions at sites of abnormal fluorescence. This may enable the discrimination between ASD and another pre-invasive bronchial lesion.

Confocal laser Endomicroscopy

The previous study was re-examined with confocal laser scanning microscope. The confocal laser Endomicroscopy was equipped with argon –krypton of 488nm and 514nm laser sources. The result was that capillary blood vessels were clearly visible by green fluorescence by confocal laser scanning microscopy .

Autofluorescence bronchoscopy

This technique exploits the differences in the fluorescence properties of bronchial mucosa compared to mucosa of pre-invasive and invasive disease. The LIFE (Lung Imaging Fluorescence Endoscopy) system, the best known instrument, uses a blue (442 nm) helium-cadmium laser to illuminate the bronchial mucosa, and the resulting fluorescence is then digitised into a real-time video image.

The majority of published studies on autofluorescence bronchoscopy have shown a significant increase in diagnostic sensitivity for dysplasia and carcinoma in situ detection. In a recent meta-analysis of over 1,000 cases investigated with the LIFE device, the sensitivity of detection for such lesions was enhanced 1.8-fold when compared with conventional white light detection.

In a recent study of 79 patients with moderate atypia, fluorescence bronchoscopy successfully identified three patients (3.7%) with radiologically occult invasive squamous cell carcinoma.

A prototype fluorescence imaging system was developed which produces real time video images of tissue autofluorescence. The system consists of a filtered blue light source (400 - 450 nm), two intensified CCD cameras, a fiber optic endoscope, and a

computer based control center. The system produces a real time pseudo color display based on images acquired from two fluorescence bands. These bands were selected based on in vivo fluorescence spectroscopic studies. The generated pseudo image clearly delineates the abnormal tissue areas for biopsy. Early cancer sites missed under conventional white light examination became visible under fluorescence imaging. A further development allows the fluorescence imaging system to be used in an alternate fashion. The system captures a fluorescence image in the green and a reflectance image in the red-near infrared. Different spectral information was exploited in the two imaging modes.

Intestinal cancer

AFI

Autofluorescence is perhaps the best evaluated spectroscopic modality in the large intestine of autofluorescence were done on ex-vivo tissue in the early 1990s¹⁹⁻²⁰ In-vivo work was done by Mayinger et al using blue-light excitation on a variety of colonic lesions with a sensitivity and specificity of 98% and 89% for the detection of dysplastic adenomas. Several prototype autofluorescent imaging systems have been developed and studies are currently underway evaluating them throughout the gastrointestinal tract. Unlike confocal endocytoscopy, and the point spectroscopic techniques, these autofluorescent systems offer the ability to scan large areas of tissue.

Cervical cancer –Colposcopy

AFI

Autofluorescence spectroscopy in the diagnosis of cervical intraepithelial neoplasia (CIN) using broadband light excitation is presented.

In this study sixty-eight patients at risk for CIN were examined. After excitation with a broadband light between 375 and 440 nm, spectral distribution of native tissue fluorescence (autofluorescence) was acquired from 685 cervical sites for the localisation and differentiation of CIN, and compared with colposcopically directed biopsy and human papillomavirus (HPV) DNA testing. The evaluation of spectral measurements revealed significantly lower autofluorescence values for CIN 3 lesions compared with normal tissue ($P < 0.001$), and compared with CIN 1 or CIN 2 ($P < 0.002$). High grade CIN lesions (CIN 2/3) presented with a significant reduced autofluorescence compared with CIN 1 ($P < 0.002$). Patients with a positive HPV DNA testing showed a significantly lower autofluorescence than patients tested negative for HPV DNA ($P < 0.05$). Severe inflammation such as chronic cervicitis may lead to false positive results.

Consequently, autofluorescence spectroscopy represents an interesting approach for the detection of cervical neoplasia. Using an excitation wavelength band between 375 and 440 nm, significant differences between normal and precancerous lesions of the cervix can be seen.

Chapter 5

Material and Methods

The Spectral Imaging Endoscopic System (SIES) introduced in this thesis, consists of a Linear Variable Filter (LVF), a Xenon light source, the light transfer cable, the hysteroscope and the CCD camera. A stepper motor, an encoder and linear motion system provide the tunability to the LVF and a microcontroller, a USB to TTL interface controller and a stepper motor driver control the SIES from a PC through dedicated firmware/software that was developed. The forthcoming sections will illustrate how and why each component was selected.

The use of LVF

Typically the hardware of spectral imaging system comprises an imaging detector coupled with an imaging monochromator, both interfaced with personal computer and control units. The imaging monochromator is the critical component in any kind of spectral imaging system. It operates as a tunable optical filter, enabling the inspection and capturing of multiple narrow band spectral images across its tuning range or, if tuning spectral resolution is high, a full spectrum per image pixel.

Earlier we demonstrated some available imaging monochromators. As mentioned, these devices are design to comply with the needs of a variety of diverse applications, ranging from astronomy to microscopy. The three main categories of imaging monochromators widely used are: the Acousto-Optic Tunable Filters (AOTF), the Liquid Crystal Tunable Filters (LCTF), and the Fourier Transformed Interferometers (FTI). The integration of above-mentioned technologies to common optical devices such as cameras and optical microscopes, has led to the development of a valuable diagnostic tools. On the other hand several limitations of these devices have been reported such as limited spectral range (AOTFs, LCTFs), low throughput (AOTFs, LCTFs), image shifting during wavelength tuning (AOTFs), non-real time spectral imaging (FTI), time consuming acquisition (FTI). Moreover the relevant instrumentation is in all cases expensive, delicate and complicated. These technological limitations are in several cases preventing the applicability of these systems in endoscopy for in vivo, non-destructive analysis of living tissues applications. For these reasons we decided to use a LVF.

The LVF, with the optical design we introduce, has certain advantages. First of all, it presents a constant throughput, bigger than 40% through its whole spectral range. There are no image shifting during wavelength tuning and no chromatic aberrations. It is real time and the acquisition time is determined by the CCD camera capturing time and the step motor's speed. The device built is relatively cheap in comparison to other ETFs, robust and durable. There no limitations on transportation or use in

motion and due to the great range of fields of view and it can be used in numerous endoscopic applications. Despite the advantages, a LVF is not the perfect tunable filter. Its main disadvantage is the fact that being linear and with finite physical dimensions, does not allow the random, real time access to all wavelengths. The filter has to be moved into the correct position corresponding to the desired wavelength, passing all previous wavelengths. Of course, no real problem exists in case your main task is acquiring spectral cubes.

The integration of the monochromator was decided to be done on the entry of the light transfer cable. The main reason for that was the hysteroscope is handled by the physician single handed and the weight and volume of the imaging device must remain minimized. Using a monochromator of any kind coupled to the endoscope's camera would increase the physical dimensions considerably. Transferring the monochromator way from the imaging module of the SIES on a remote location provides spectral imaging capability without any change to optical characteristics and mechanical properties of the endoscope.

The placement of the LVF in front of the transfer light cable provides the necessary band pass filtering based on the width of the entrance point of the cable. It is pivotal then to drive the LVF to the desired position swiftly and accurately. The most obvious choice is a motorized linear stage. Many companies can provide stages with traveling speed 3m/s and accuracy up to 3 μ m. The disadvantages of such a stage are its dimensions and the difficulty to be controlled as desired for such an application. A linear stage with stroke around 200mm (that is the length of the LVF) has total length of least 500mm; equally high are width and height. All these stages are intended for industrial use and their motion is controlled by specialized driver that are bulky and their 'repertoire' of movements is limited. We decided to use linear ball bearing stage and a motor in order to build our own linear motorized stage. It has zero lashes and it provided untroubled, smooth linear motion, using two series of recirculating ball bearings. The motor could not be other than a step motor. Their unique ability to move steady step per pulse (hence the name) makes measurement of moving distance easy and the use of controller unnecessary when speeds are low. For higher speeds an encoder is necessary when absolute accuracy is essential. Including an encoder has another advantage; it creates a closed loop control system that is robust and accurate. Finally a unipolar step motor with embedded encoder was for the final design.

The step motor and the linear stages are the center of the whole mechanical design. They had to be combined some way in order to work as a linear motorized stage. The filter had to be able to move freely, with no lashes and the whole arrangement had to be mounted in complete alignment with the light source and the light transfer cable. The complete design was ours and fulfills all the above requirements in the

minimum outer dimensions. The figures 1 and 2 demonstrate the interior design that was made.

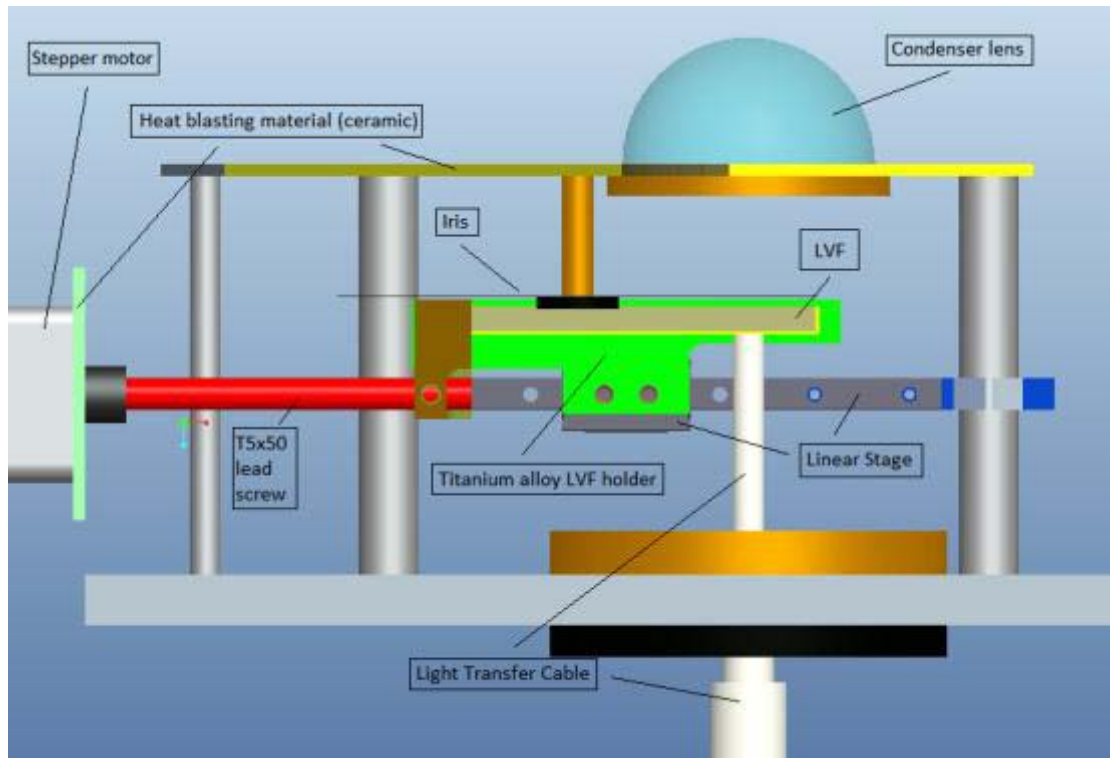


Figure 1. The 3D design of the solid model of the SIES light monochromator.

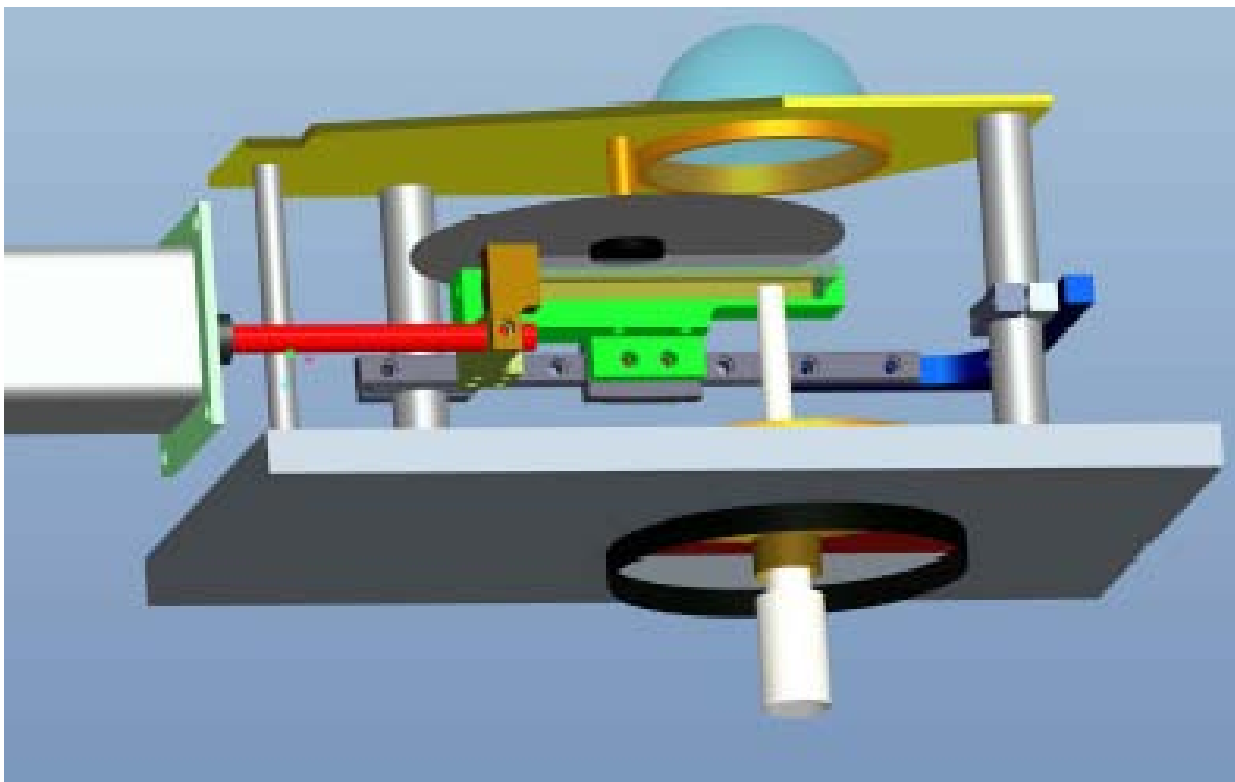


Figure 2. The 3D design of the solid model of the SIES light monochromator from another view.

Electronics

We had to fully develop the electronics controlling the device, both hardware and software. The device must move the filter left and right. It must be able to go into a random wavelength (e.g. 578nm) within its spectral range. User messages are also required. With these in mind and taking into consideration all specifications we concluded to the following:

Entries:

- Communication via USB.
- Three (3) SPST switches controlling operation: for movement to right, for movement to left and device reset.

Exits:

- Communicate with the PC via a concrete protocol which:
 - Accepts the commands of movement.
 - Returns messages of any dysfunctions.
 - Returns the suitable messages to the user concerning the proper operation.

The system should be able to calculate the position of the filter to be moved given the desirable wavelength. For that reason the system holds in the microcontroller's memory known positions of known wavelength and an interpolation function.

The electronic PCD design was decided to be one board only with the minimum dimension. The reason was the limited space inside the device and the ability to repair or replace the board with the least effort possible. Although SMD designs are more suitable for such construction, the lack of proper equipment led to the use of DIP IC.

Power supply is provided by a 12 Volt DC external power pack with certified medical specifications for clinical use.

Hardware – Parts

Microcontroller – ATmega162

The ATmega162 is a low-power CMOS 8-bit microcontroller based on the AVR enhanced RISC architecture. By executing powerful instructions in a single clock cycle, the ATmega162 achieves throughputs approaching 1 MIPS per MHz allowing the system – designer to optimize power consumption versus processing speed.

The AVR core combines a rich instruction set with 32 general purpose working registers. All the 32 registers are directly connected to the Arithmetic Logic Unit (ALU), allowing two independent registers to be accessed in one single instruction executed in one clock cycle. The resulting architecture is more code efficient while achieving throughputs up to ten times faster than conventional CISC microcontrollers.

The ATmega162 provides the following features: 16K bytes of In-System Programmable Flash with Read-While-Write capabilities, 512 bytes EEPROM, 1K bytes SRAM, an external memory interface, 35 general purpose I/O lines, 32 general purpose working registers, a JTAG interface for Boundary-scan, On-chip Debugging support and programming, four flexible Timer/Counters with compare modes, internal and external interrupts, two serial programmable USARTs, a programmable Watchdog Timer with Internal Oscillator, an SPI serial port, and five software selectable power saving modes. The Idle mode stops the CPU while allowing the SRAM; Timer/Counters, SPI port, and interrupt system to continue functioning. The Power-down mode saves the register contents but freezes the Oscillator, disabling all other chip functions until the next interrupt or Hardware Reset. In Power-save mode, the Asynchronous Timer continues to run, allowing the user to maintain a timer base while the rest of the device is sleeping. In Standby mode, the crystal/resonator Oscillator is running while the rest of the device is sleeping. This allows very fast start-up combined with low-power consumption. In Extended Standby mode, both the main Oscillator and the Asynchronous Timer continue to run.

The device is manufactured using Atmel's high density non-volatile memory technology. The On-chip ISP Flash allows the program memory to be reprogrammed In-System through an SPI serial interface, by a conventional non-volatile memory programmer, or by an On-chip Boot Program running on the AVR core. The Boot Program can use any interface to download the Application Program in the Application Flash memory. Software in the Boot Flash section will continue to run while the Application Flash section is updated, providing true Read-While-Write operation. By combining an 8-bit RISC CPU with In-System Self-Programmable Flash on a monolithic chip, the Atmel ATmega162 is a powerful microcontroller that provides a highly flexible and cost effective solution to many embedded control applications.

The figures 3 and 4 below demonstrate its pin – out and its block – diagram.

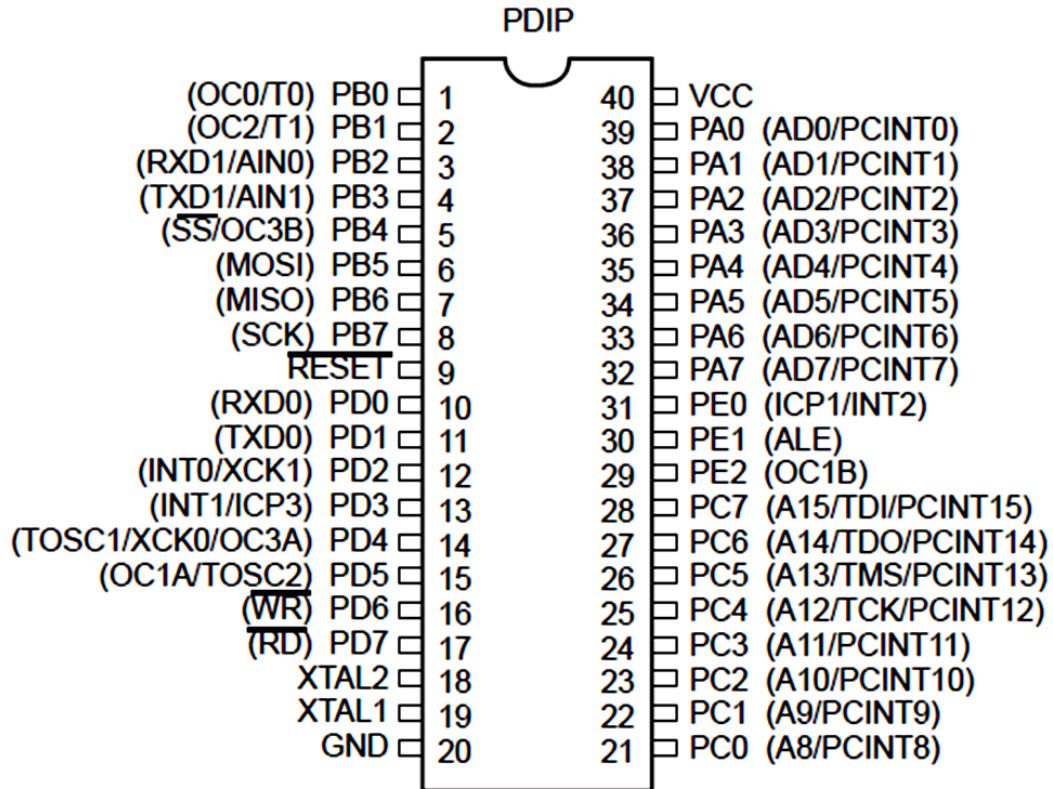


Figure 3. The Atmel ATmega162 pin – out.

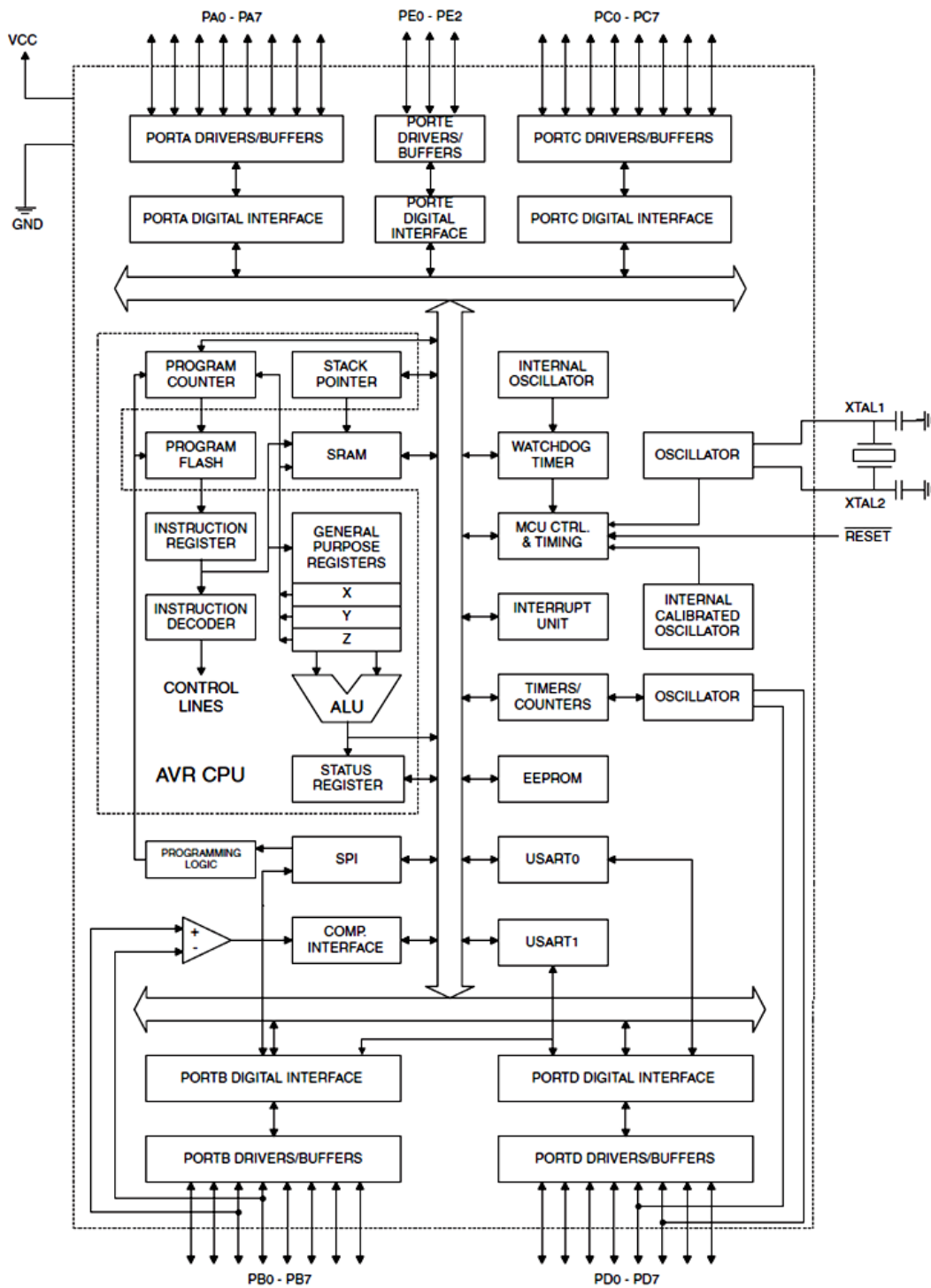


Figure 4. The Atmel ATmega162 block – diagram.

FT232R

The FT232R is the latest device to be added to FTDI's range of USB UART interface Integrated Circuit Devices. The FT232R is a USB to serial UART interface with optional clock generator output, and the new FTDIChip-ID™ security dongle feature. In addition, asynchronous and synchronous bit bang interface modes are available. USB

to serial designs using the FT232R have been further simplified by fully integrating the external EEPROM, clock circuit and USB resistors onto the device. The device offers the following advanced features:

- Single chip USB to asynchronous serial data transfer interface.
 - Entire USB protocol handled on the chip. No USB specific firmware programming required.
 - Fully integrated 1024 bit EEPROM storing device descriptors and CBUS I/O configuration.
 - Fully integrated USB termination resistors.
 - Fully integrated clock generation with no external crystal required plus optional clock output selection enabling a glue-less interface to external MCU or FPGA.
 - Data transfer rates from 300 baud to 3 Mbaud (RS422, RS485, RS232) at TTL levels.
 - 128 byte receive buffer and 256 byte transmit buffer utilising buffer smoothing technology to allow for high data throughput.
 - FTDI's royalty-free Virtual Com Port (VCP) and Direct (D2XX) drivers eliminate the requirement for USB driver development in most cases.
 - Unique USB FTDIChip-ID™ feature.
 - Configurable CBUS I/O pins.
 - Transmit and receive LED drive signals.
 - UART interface support for 7 or 8 data bits, 1 or 2 stop bits and odd / even / mark / space / no parity
-
- FIFO receive and transmit buffers for high data throughput.
 - Synchronous and asynchronous bit bang interface options with RD# and WR# strobes.
 - Device supplied pre-programmed with unique USB serial number.
 - Supports bus powered, self-powered and high-power bus powered USB configurations.
 - Integrated +3.3V level converter for USB I/O.
 - Integrated level converter on UART and CBUS for interfacing to between +1.8V and +5V logic.
 - True 5V/3.3V/2.8V/1.8V CMOS drive output and TTL input.
 - Configurable I/O pin output drive strength.
 - Integrated power-on-reset circuit.
 - Fully integrated AVCC supply filtering - no external filtering required.
 - UART signal inversion option.

- +3.3V (using external oscillator) to +5.25V (internal oscillator) Single Supply Operation.
- Low operating and USB suspend current.
- Low USB bandwidth consumption.
- UHCI/OHCI/EHCI host controller compatible.
- USB 2.0 Full Speed compatible.

The FT232RL we used adds two new functions compared with its predecessors, effectively making it a "3-in-1" chip for some application areas. The internally generated clock (6MHz, 12MHz, 24MHz, and 48MHz) can be brought out of the device and used to drive a microcontroller or external logic. A unique number (the FTDIChip-ID™) is burnt into the device during manufacture and is readable over USB, thus forming the basis of a security dongle which can be used to protect customer application software from being copied. Figures below show the block – diagram and pin – out of the FT232RL.

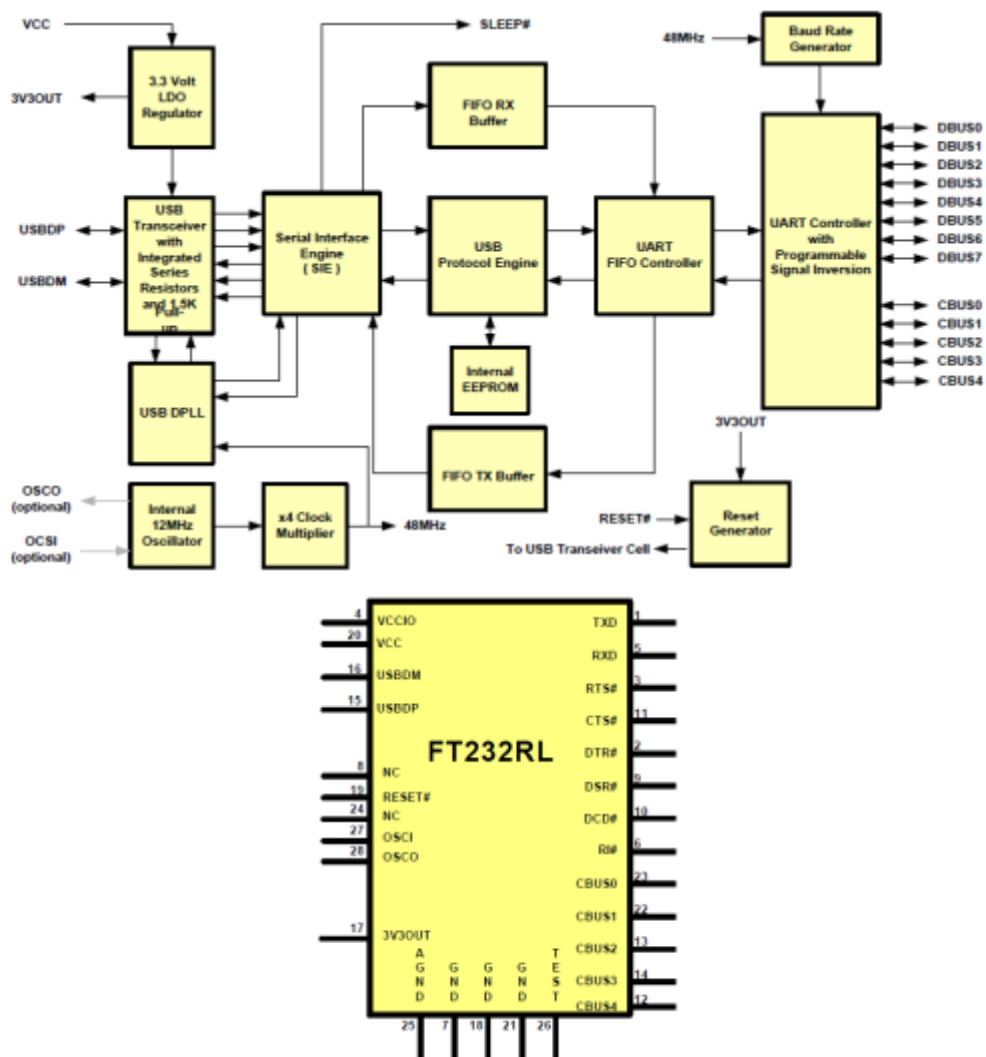


Figure 5. FT232RL block diagram and pinout

L293E

The L293B and L293E are quad push-pull drivers capable of delivering output currents to 1A per channel. Each channel is controlled by a TTL compatible logic input and each pair of drivers (a full bridge) is equipped with an inhibit input which turns off all four transistors. A separate supply input is provided for the logic so that it may be run off a lower voltage to reduce dissipation. This IC is used to provide enough current to drive a stepper motor using a microcontroller. Below are demonstrated the block diagram and its pin – out.

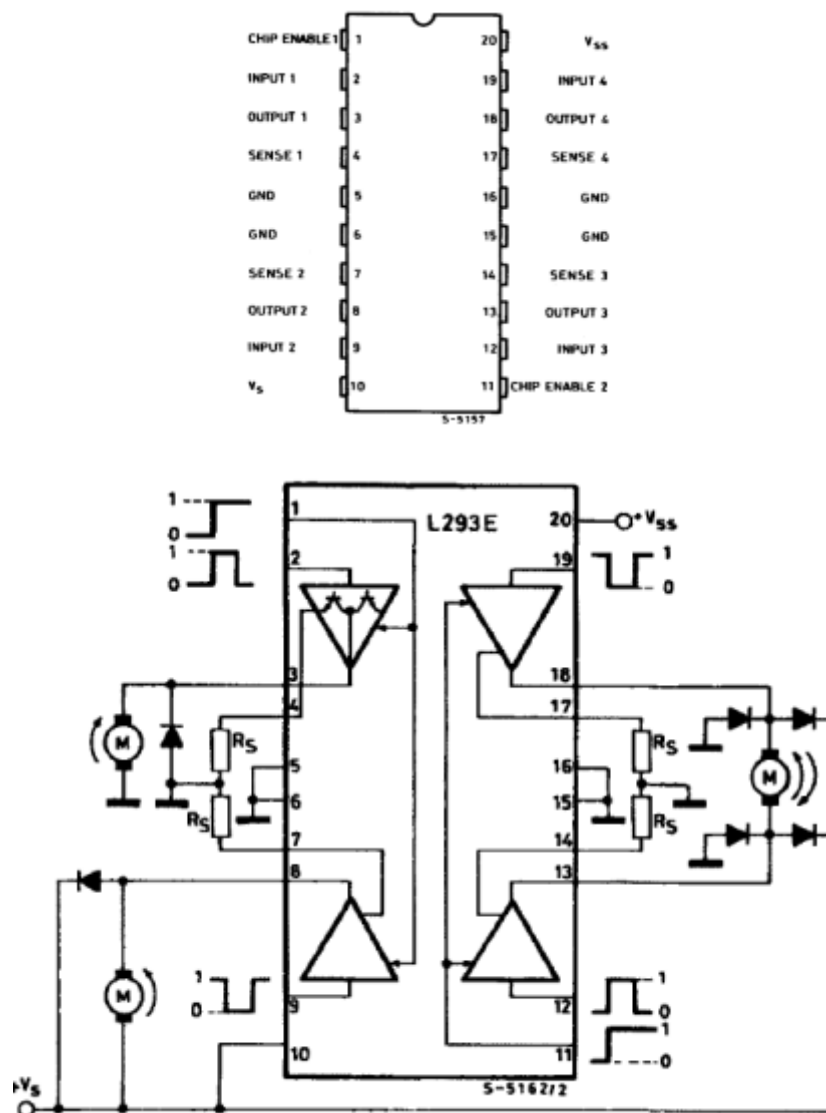


Figure 6. The L293E block diagram and pinout

L7805

The L7800 series of three-terminal positive regulators is available in TO-220 ISOWATT220 TO-3 and D2PAK packages and several fixed output voltages, making it useful in a wide range of applications. These regulators can provide local on-card regulation, eliminating the distribution problems associated with single point regulation. Each type employs internal current limiting, thermal shut-down and safe area protection, making it essentially indestructible. If adequate heat sinking is provided, they can deliver over 1A output current. Although designed primarily as fixed voltage regulators, these devices can be used with external components to obtain adjustable voltages and currents. The block diagram is displayed on the figure below.

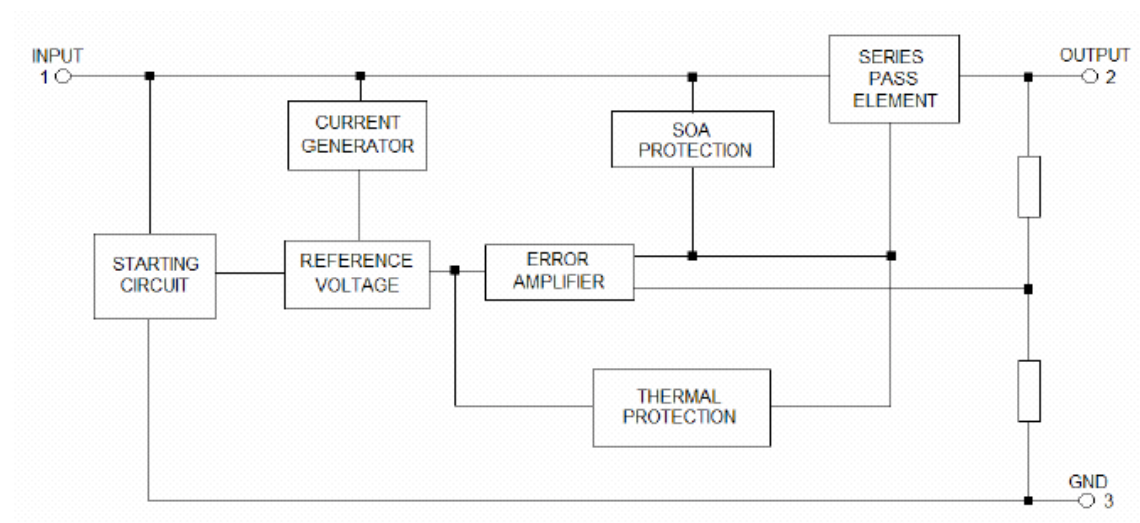


Figure 8. The L7805 block diagram

Hardware – Design

The PCB design was determined by the functionality of the endoscopic system and the future improvements. There were no space limitations inside the device so the size was not an issue. The schematic of the complete design is shown in figure 9 below. The design is double layer design, utilizing large clear copper areas as heat – sinks. Two stepper motors are driven by two L293E, controlled by the ATmega162. The operation voltage towards the stepper motors can be selected from a jumper near the current drivers. The FT232RL converts the USB to TTL level signals so that the user commands are transferred to the AVR. Finally, each stepper motor has start – stop switches for motion limit. As seen, the concept of the PCB design is one board only, for untroubled access and replacement. The prototype is demonstrated in figure 10.

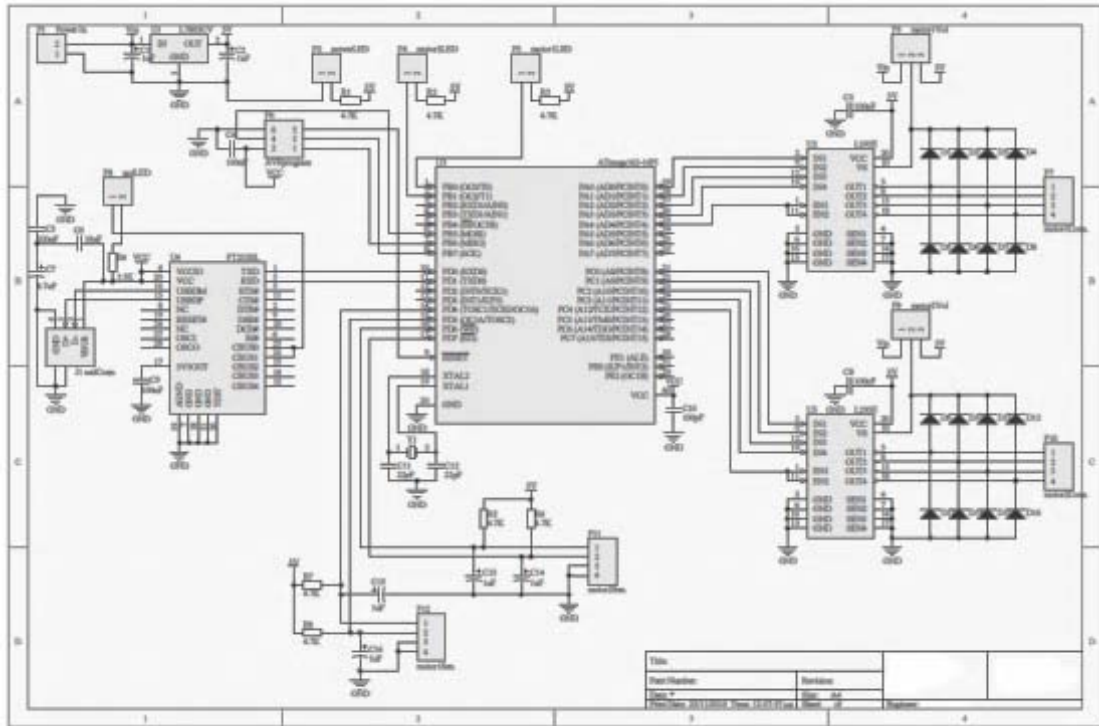


Figure 9. The schematic diagram

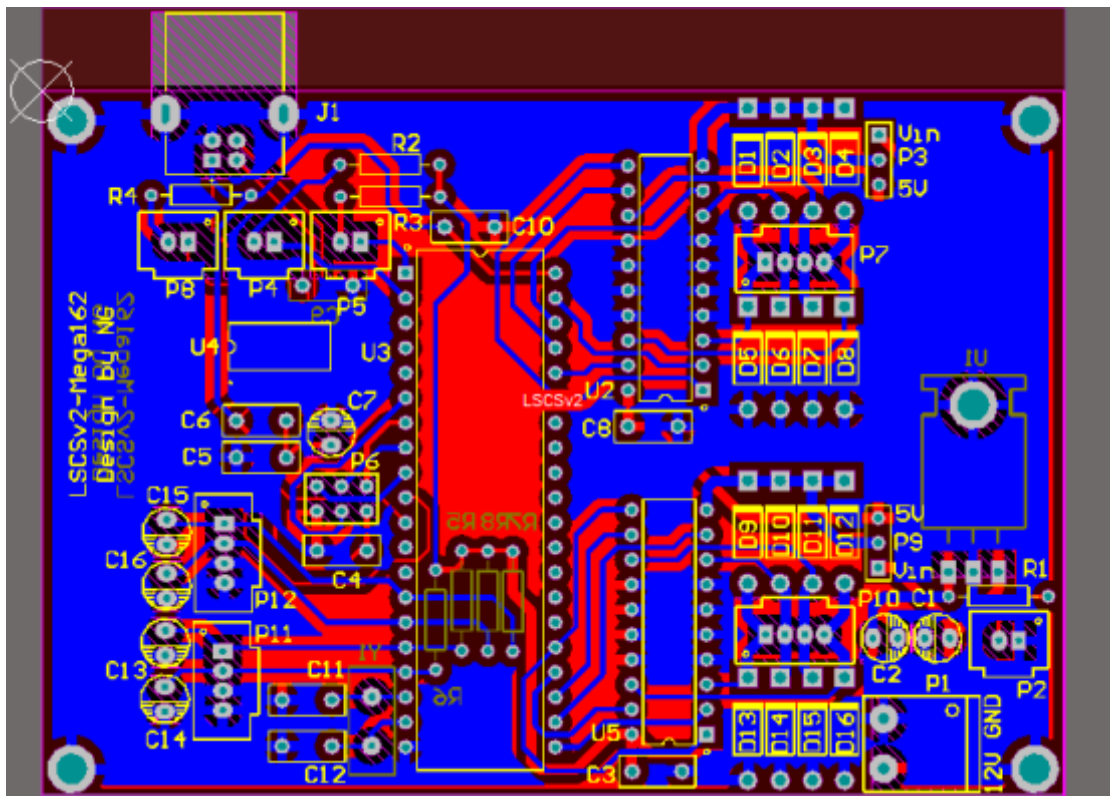


Figure 10. The PCB design

Firmware

The firmware was developed with the CV AVR compiler. The basic routine sketching the firmware's operation appear in the next flow chart (figure 7). The firmware firstly initializes the AVR and then waits in an infinite loop for a command to come from the PC. When a command arrives is executed immediately and only after it is executed, the next command takes its turn for execution. If no other command is waiting to be executed, the firmware returns to the infinite loop. The commands string along and are executed in FIFO order.

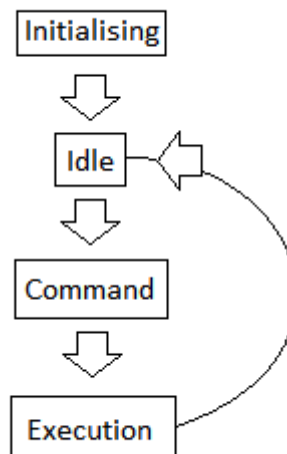


Figure 11. The main routine of the firmware.

The complete code in C (without the UART routine) can be seen in appendix A.

PC software

Having completed the firmware, dedicated software was developed to control the SEIS and enable the clinical evaluation of the system. The software was developed using Visual C++ and it performs the following tasks:

- Controls the position of the filter and thus, the wavelength of the light source.
- Controls the camera exposure and the acquisition settings.
- Displays the images captured from the camera in two monitors.
- Keeps a simple database of the patients that will be examined.
- Performs automated spectral cube acquisition.
- Performs automated time sequence image capture.
- Performs automated spectral cube acquisition over a specified time sequence.

Also, it enables the calibration of the light source and the parameters of the automated acquisition processes.

The snapshots of the application following (figures 12 to 15) demonstrate the graphic user interface. At figure 12 we can see the initial form of the Graphical User Interface (GUI) offers the all the features of the application available instantly to the user. Large applications button are designed as the SIES was operated via a touch screen monitor.

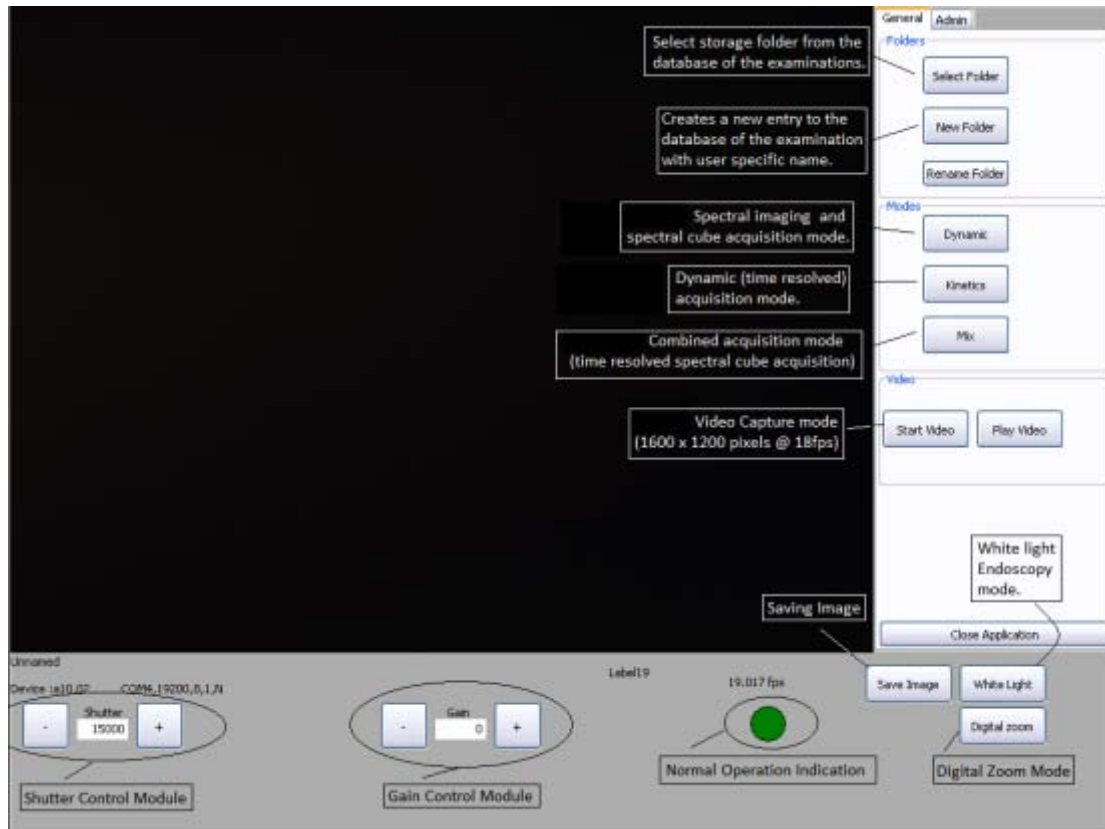


Figure 12. The GUI of the application when it starts (commented).

The user should firstly select a folder to store the data to be acquired. This can be done from select folder for a folder that already exists or the user can create a new folder from the corresponding button. A folder name can be change be selecting Rename Folder. The application holds a simple database (db) that identifies the root folders containing all the data (video, images, spectral cubes, time cubes) captured during an examination.

Continuing, the user can select to write high definition video and reproduce it, save images, zoom on the live endoscopic image and adjust the shutter and the gain of the camera. Moreover the user is able to select acquisition mode between three choices:

1. Spectral cube acquisition (Dynamic)
2. Time resolved acquisition (Kinetics) and
3. Combined acquisition (Mix).

In Dynamic a spectral cube is acquired, featuring selected bands. In Kinetics, images are acquired in time sequence in order to study phenomena that evolve over time. In the combined acquisition mode (Mix), spectral cubes are acquired in time sequence.

Figure 13 shows the GUI in Dynamic. The user can select to acquire a spectral cube or navigate through the spectral bands. The system offers 265 different spectral bands ranging from visible to near infrared.

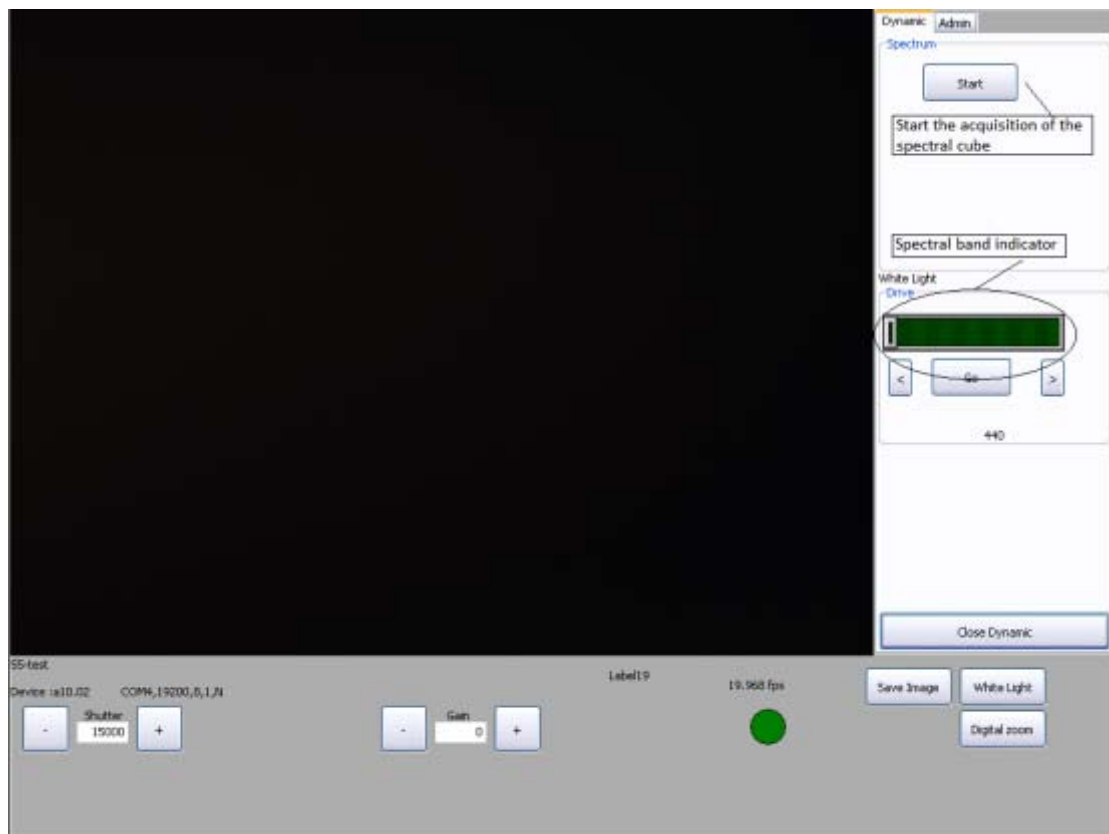


Figure 13. The GUI of the application when Dynamic is selected.

The GUI is the same in Kinetics and in Mix the spectral band indicator/navigator is not present as shown in figure 14. A fully automated process will scan all the spectral bands over a specific time sequence.

Finally, the application has a Administration form (figure 15), where the parameters of operation are defined.

The part of the code in C++ can be seen in appendix B.

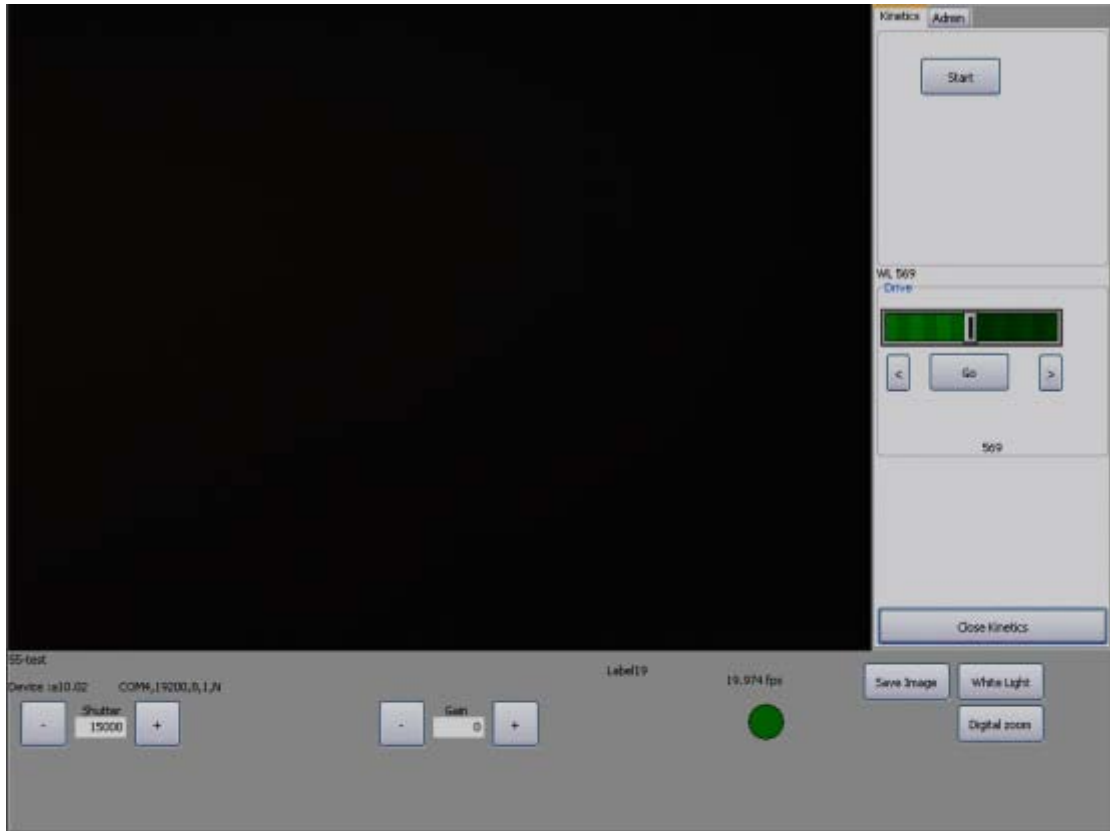


Figure 13. The GUI of the application when Kinetics is selected.

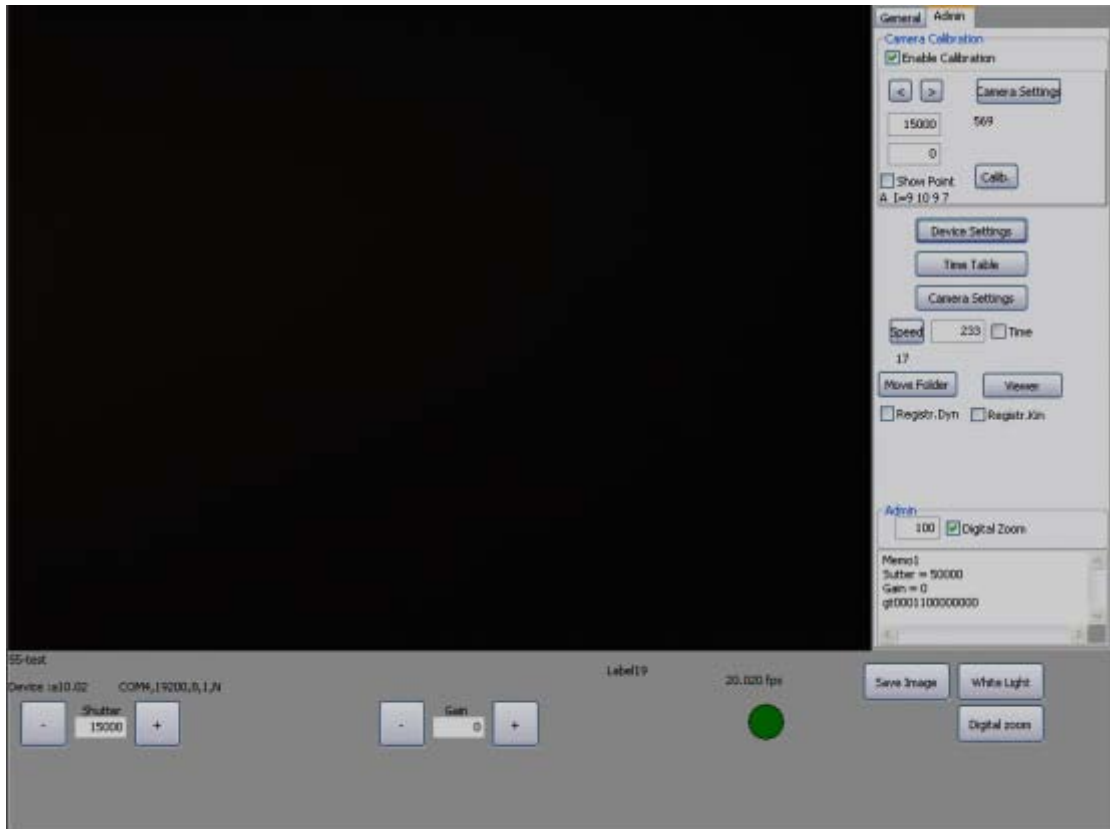


Figure 13. The GUI of the application in administration mode.

Chapter 6

Characterization and Clinical Validation

Spectral bands and calibration

On previous chapter we have described the optical and mechanical design of our SEIS. After the completion of the electronics, we set an experimental arrangement in order to calibrate the system and define its spectral characteristics. The light transfer cable was from one side attached to the light source and the other side was attached to the spectrometer, an Ocean Optics USB4000 spectrometer. The alignment of the arrangement was assured from the mechanical design. An image of the arrangement is shown in figure 1.



Figure 1. The experimental arrangement.

We made a series of measurements in order to determine the spectral resolution and accuracy of the system, the precision and the repeatability of the movements and the throughput of the SIES. With tuning step equal to 1mm, we measured the LVF from one end to the other. The spectral bands we got are shown in figure 2 below.

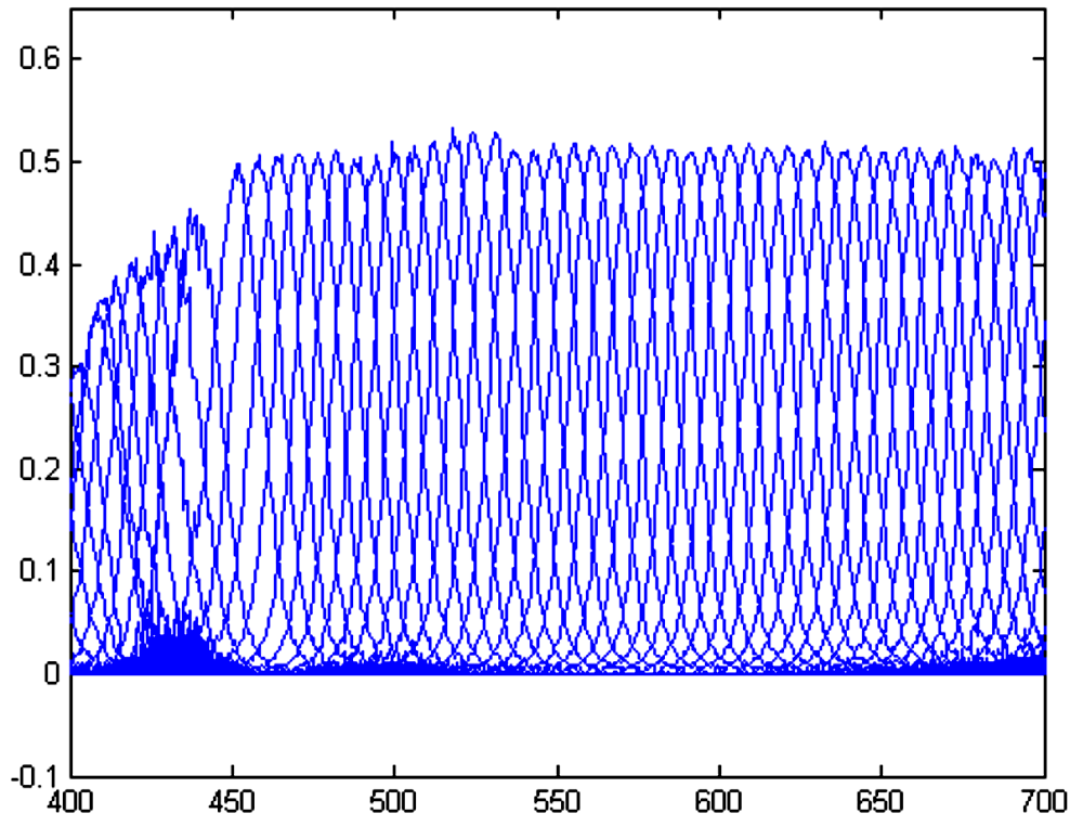


Figure 2. The Spectral response of the LVF.

With the use of MATLAB we extracted the intelligence needed for the spectral bands. Firstly we separated the bands so as the 50% of the curves' energy will not be overlapped by another band. The results are shown in figure 3. The same separation was made again but for the 10% of the curves' energy. The bands qualified are shown in figure 4.

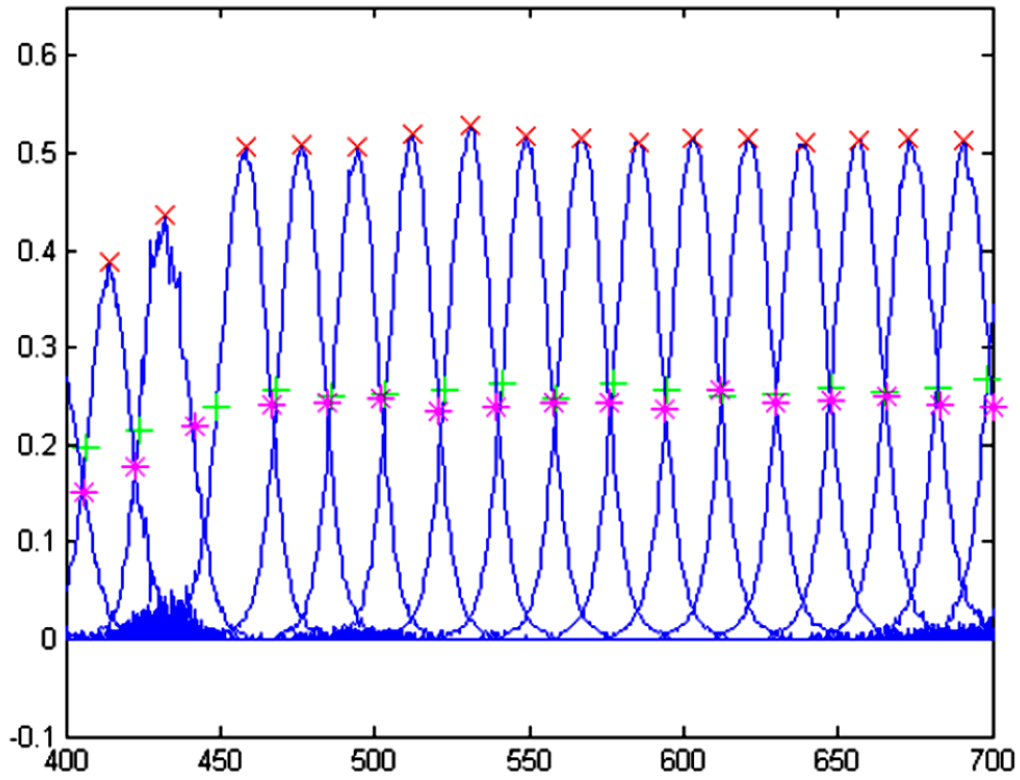


Figure 3. The bands for 50% overlapping

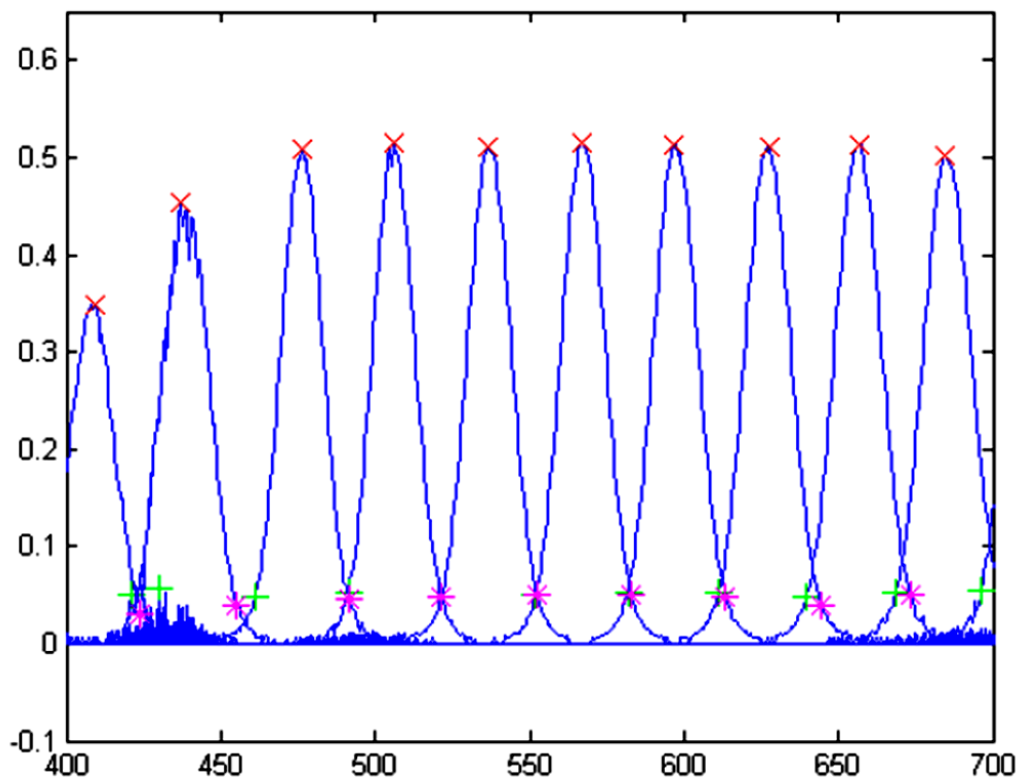


Figure 4. The bands for 10% overlapping.

The FWHM of every curve is critical for the determination of the operation characteristics of the HySIS. The FWHM is steady for the curves shown in figure 4. The spectral resolution of the HySIS does not vary more than 2nm from the maximum value to the minimum. The FWHM as a function of the wavelength is plotted and shown in figure 5.

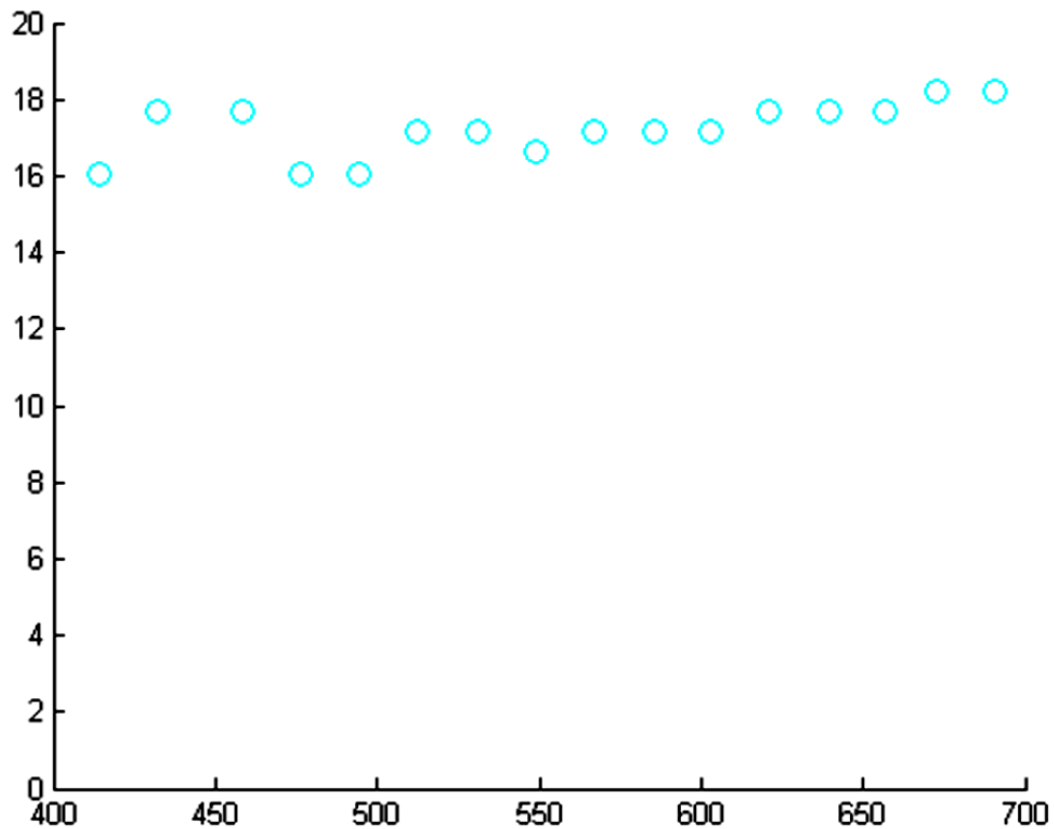


Figure 5. The FWHM of the spectral range of the LVF.

From figure 3 we can see that the transmittance is continually over 50% from 700nm to 450nm and there exist a small drop to 30% as we reach 400nm. Figure 6 shows the transmittance for the bands on figure 4.

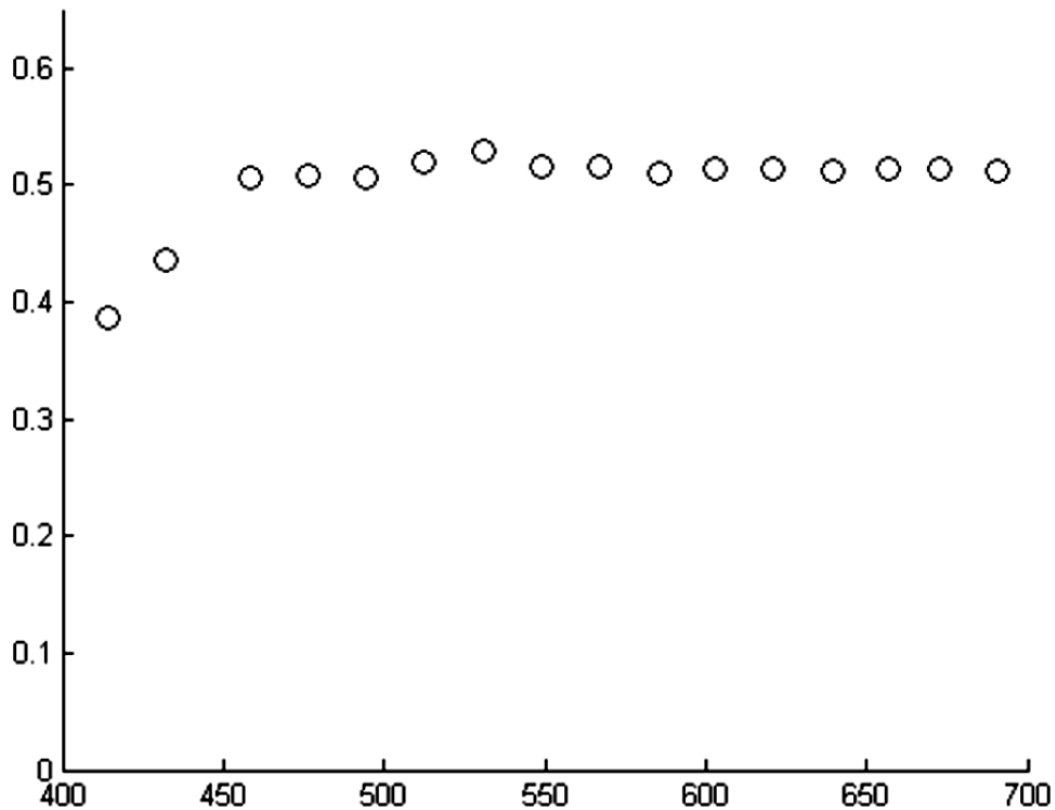


Figure 6. The FWHM for 10% overlapping bands

Although this arrangement was the final we wanted to test the repeatability of the system. We went back and forth the filter into three different wavelengths, 650nm, 550nm, 450nm, ten times. The results were the same in each case. The values varied only 1.5nm from minimum to maximum, showing that the firmware and the mechanics work more than fine. Taking into consideration that the step motor we used has 2 steps miss stepping, that is 0.1mm and with linear dispersion of 6.5nm/1mm, 0.65 nm the results prove excellent control of the LVF’s movement.

Finally, we tested another arrangement were the light transfer cable is coupled directly in front of the LVF without any optics. The output of the monochromator in that case was determined by the physical dimensions and the 6mm in diameter entrance pupil of the light transfer cable dictates 11 spectral bands of 25nm width each. The resulting spectral bands are demonstrated on figure 7 below.

Before the clinical evaluation, the system was calibrated so that each spectral band has exactly the same intensity during acquisition and, also, the color representation was normalized with the use of a MacBeth Color Chart Checker, the patent of whom is displayed at figure 8.

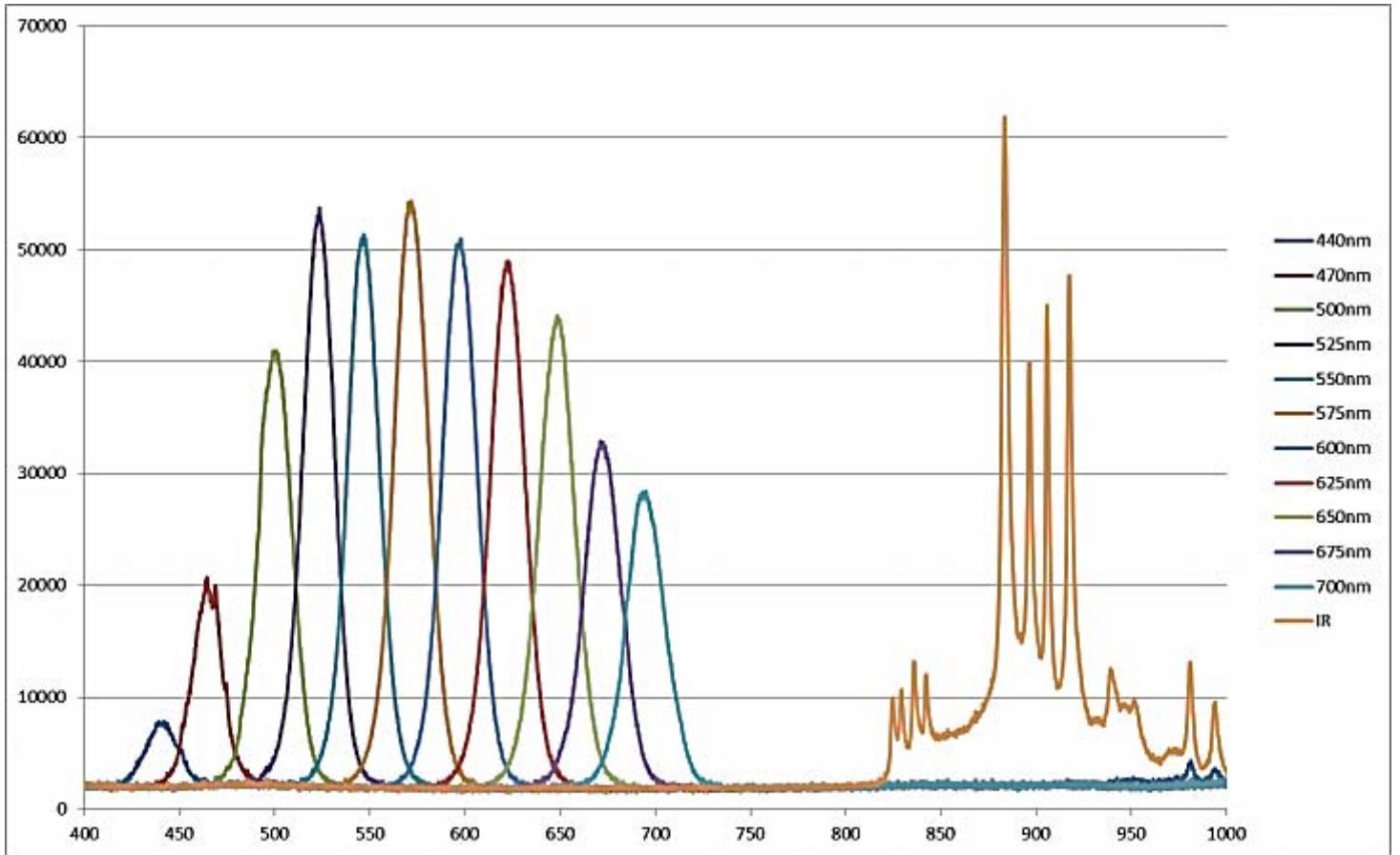


Figure 7. The spectral bands of the SIES.



Figure 8. MacBeth Color Chart Checker and the RGB values of each sample.

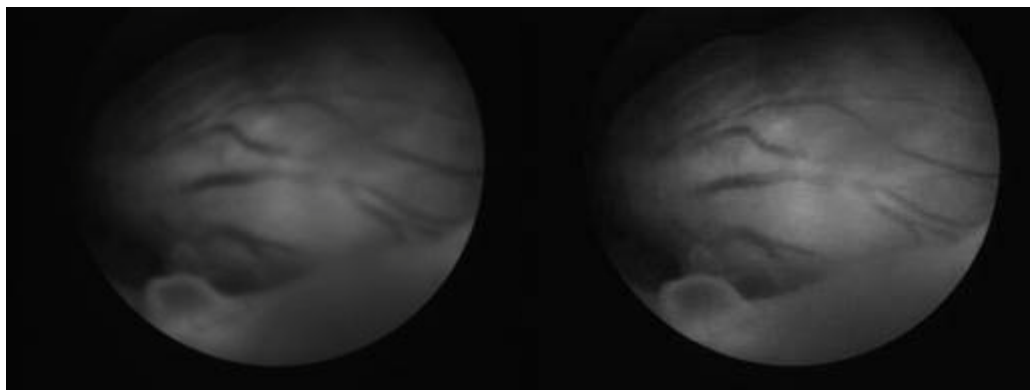
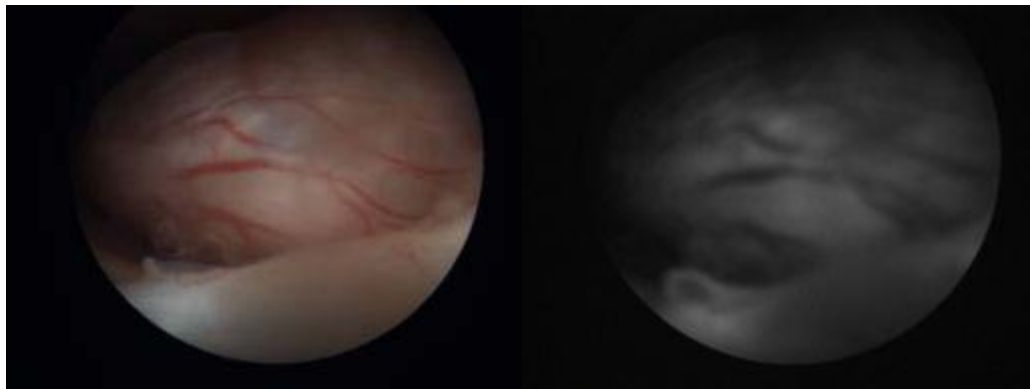
Clinical Evaluation

A set of 50 random patients were examined with our SIES in collaboration with the University Hospital of Ioannina. The patients were referred for hysteroscopy after previous ultrasonic check and/or prior doctor advice. During the examination, only doctors and medically trained personnel were present. The users of the SIES were trained previously ex-vivo. In all cases spectral cubes were acquired from various areas of interest according to the physician's opinion.

A total of 88 spectral cubes of diagnostic importance were finally selected. Inside that set, 5 spectral cubes were of undeveloped endometrium, 20 of polyps, 6 of hyperplastic endometrium, 6 of endometriosis, 2 of dysfunctional uterus bleeding (DUB) and 14 of various pathologies. The remaining spectral cubes were of normal endometrium. The total amount of data was more than 150 GB. For that purpose we will provide only one example of a spectral cube, the processing we undergo the data and characteristic cases.

Spectral image enhancement

A complete spectral cube of a patient is displayed below. The first image is the standard color RGB image and following in order (left to right) 440nm, 470nm, 500nm, 525nm, 550nm, 575nm, 600nm, 625nm, 650nm, 675nm, 700nm, IR (830nm, 80nm FW/HM).



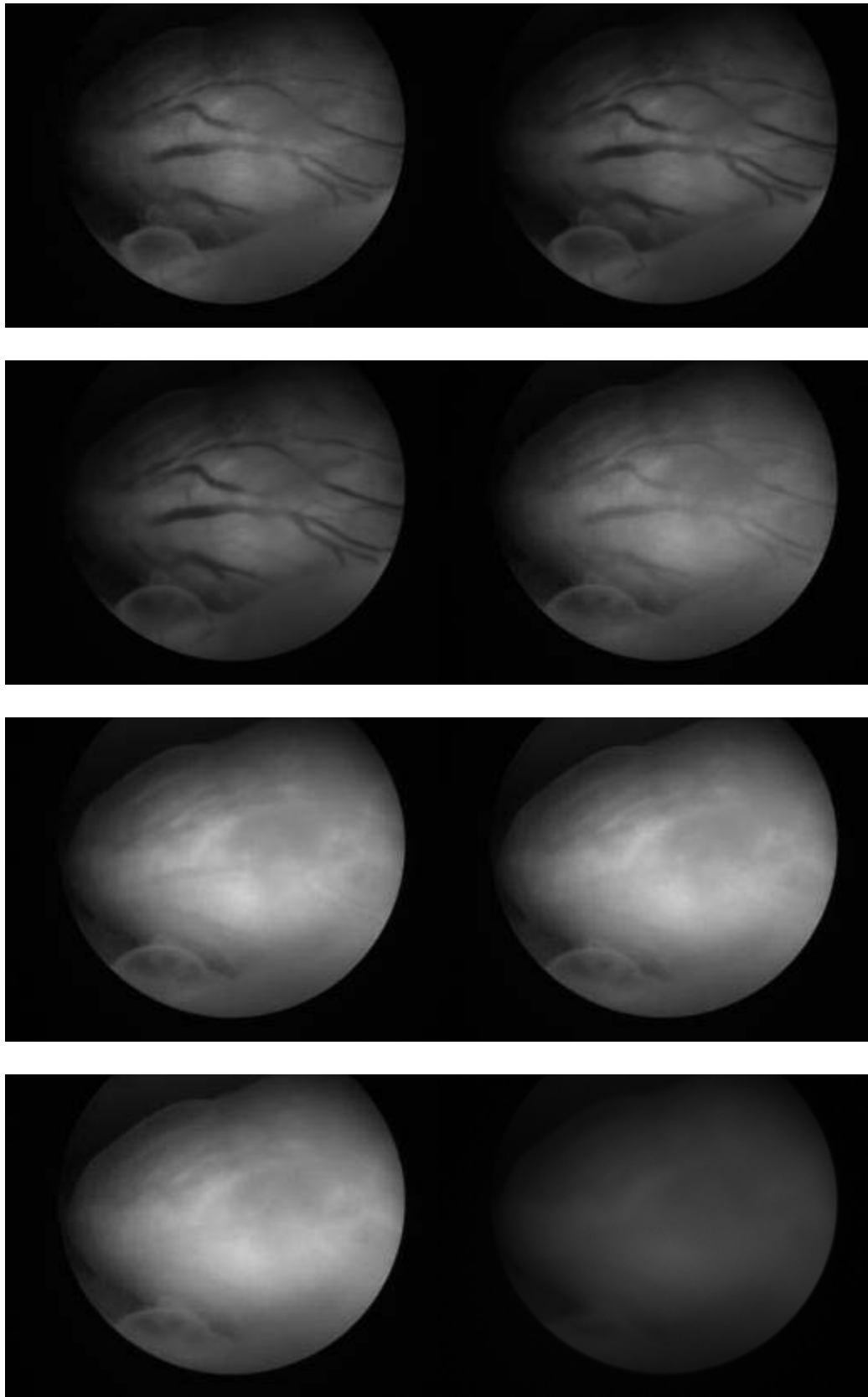


Figure 9. Color and spectral images from a single spectral cube.

As it can be seen, when in the blue area (400nm – 500nm) of the spectrum, more surface features can be visualized better. Moving to the green area (500nm – 600nm), vessels can be seen in greater contrast. Moreover, the green light penetrates the tissue in more depth and vessels unseen of the surface are seen. Finally, at the red and near infrared (NIR) area of the spectrum, the tissue becomes more transparent and the penetration depth is greater. Deep vessels and unseen features are better detected. The images following will demonstrate features and findings that were better enhanced through the various spectral bands of the SIES.

1. Invisible cyst

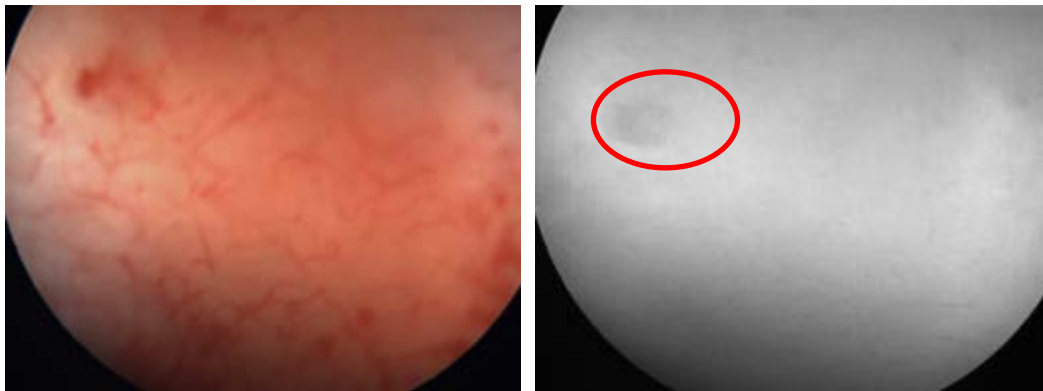


Figure 10. Color (left) and Spectral Image (right)

On the top left of the 675nm band image (marked) there can be seen a cyst which is invisible in the color image.

2. Micro vascular pattern

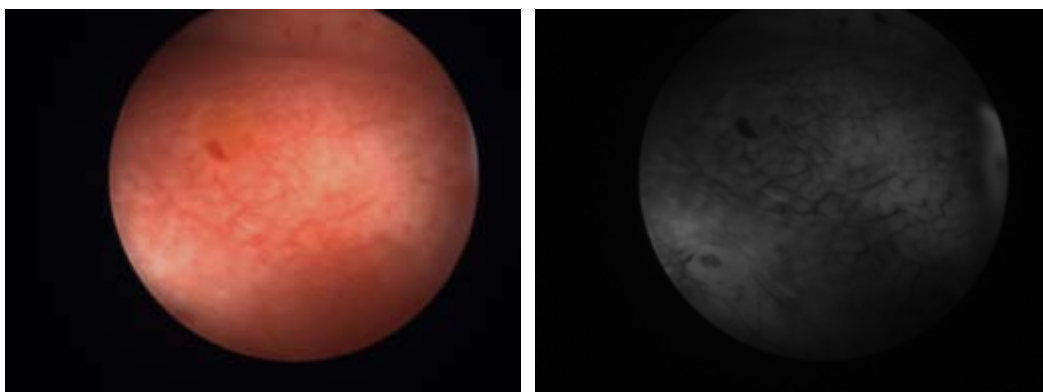


Figure 11. Color (left) and Spectral Image (right)

On the 575nm band image (right), the micro vascular pattern is very clearly distinguished, allowing the physician of better visualization of atypical blood vessel patterns, suspicious of neoplastic tumors growth.

3. Polyp's blood vessels

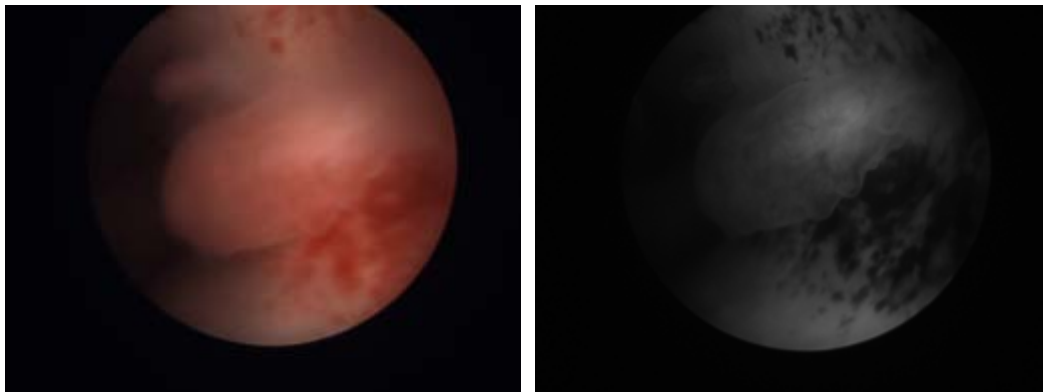


Figure 12. Color (left) and Spectral Image (right)

On the 575nm band image (right), the micro vascular pattern on the polyp can be clearly seen.

4. Deep Vessel



Figure 13. Color (left) and Spectral Image (right)

On the 550nm band image (marked), blood vessels are seen that are not visible on the color image.

5. Deep Vessel

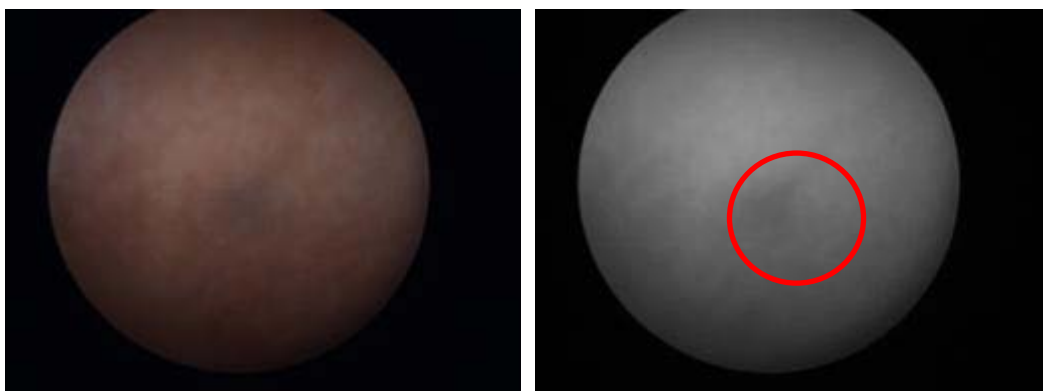


Figure 14. Color (left) and Spectral Image (right)

On the 700nm band image (markes), a shadow on its center can be seen, featuring probably a deeper vessel.

6. Vascular pattern

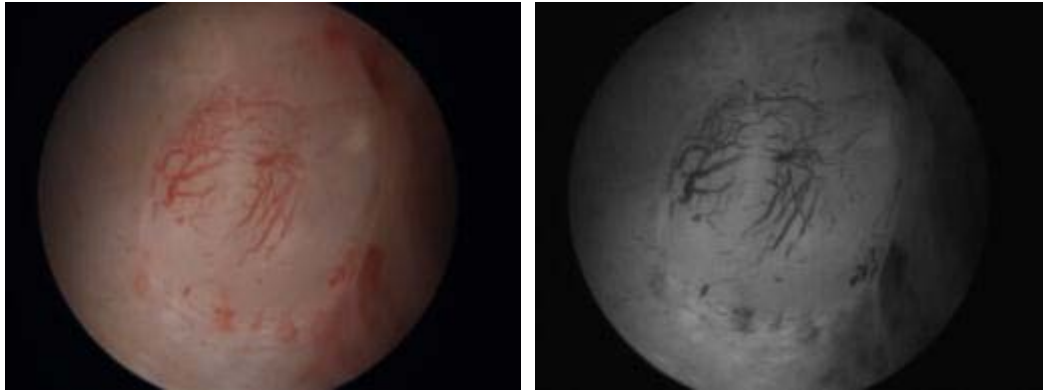


Figure 15. Color (left) and Spectral Image (right)

On the 470nm band image (right), the vascular pattern can be seen with greater contrast than in the color image and at the same time, the edges of the endometrium surface are enhanced.

Quantitative diagnostic spectral imaging

As it has been discussed previously, spectral imagery is usually depicted in a spectral cube, a registered set of images, featuring one spectral and two spatial dimensions (pixel coordinates). Spectral imaging data are transforming the RGB color space to a high dimensional representation of intensity vectors corresponding to different wavelengths.

The number of the spectral dimensions is proportional to the spectral resolution of the spectral camera and, in principle, the higher the spectral resolution, the greater the diagnostic information that it is contained to the acquired spectra. The number of spectra that are acquired by a spectral camera is proportional to the spatial resolution of its image sensor and therefore the higher the spatial resolution, the greater the topological information that can be obtained for the localization of a target feature. Generally speaking, hardware improvements towards increasing the system's spectral and spatial resolutions impact positively its accuracy in identifying and mapping compositional features of diagnostic importance. It should be noted however, that the spectral/spatial resolution requirements depend heavily on both sample's complexity and operating wavelength range (e.g. Ultraviolet-Visible-Infrared spectroscopy). Solid tissues are typically characterized by a high spatial heterogeneity, which sets high spatial resolution requirements in case that sample surface details need to be depicted.

The spectral resolution requirements depend largely on the operating spectroscopy type. For example, mid-infrared spectra contain fine features, such as sharp peaks and deeps, while visible and near infrared spectral profiles are typically smooth and broad. Higher spectral resolution is required for acquiring spectra containing fine features, but these spectra are much more informative for the composition of the sample, as compared to the smooth spectra. Smooth and broad spectra are in most cases the result of the superimposition of several spectra, corresponding to a number of co-localized compositional features. These spectra can be captured at a much lesser resolution, without significant loss of information. However, sophisticated spectral data processing and analysis methods are required for unmixing, extracting and classifying the diagnostic information that might be contained in the smooth spectra, produced by visible and near infrared absorption, scattering and fluorescence spectroscopy.

In most spectral cube datasets not all of the measured intensities at every wavelength are important for understanding the underlying phenomena of interest. As the processing the entire dataset may be computationally intensive and time consuming, transforming the image set into a reduced dimensionality structure is often of essential importance. This pre-processing step simplifies also the calculations performed by the classifier thus increasing its efficiency, while in parallel making the process relatively immune to the so-called “curse of dimensionality” issue.

As it is expected spectral bands at which the spectra are very similar can be omitted at no or minimum cost in the classification accuracy. It is therefore possible to isolate the most informative wavelengths by examining the spectra and reduce the vast amount of data we have collected. In more demanding applications, however, sophisticated methods are employed, which can perform the data dimensionality reduction in an automated manner. For the classification of our data we used the Spectral Angle Mapper algorithm.

The Spectral Angle Mapper (SAM) is a physically-based spectral classifier that determines the spectral similarity between the measured and the reference spectra. The spectra are treated as vectors in a space with dimensionality equal to the number of bands and the angle that is formed between these vectors is used as a metric of the spectral similarity (figure below). Smaller angles represent closer matches to the reference spectrum. SAM has also been used as a feature selection method for selecting an optimal subset of spectral bands.

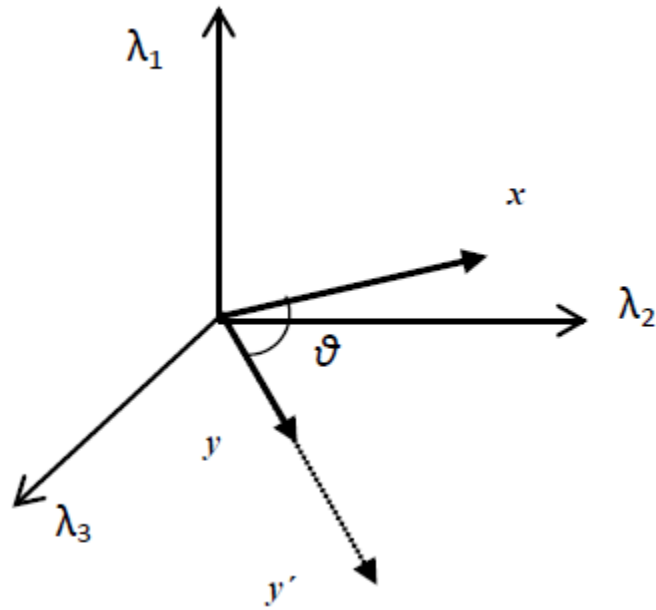


Figure 16. Vector representation of x, y pixels in a 3 dimensional orthonormal space corresponding to 3 different wavelengths.

SAM essentially calculates the angle θ between them. The angle (ϑ) between pixel vectors as a discrimination measure is given by the formula:

$$SAM(\mathbf{x}, \mathbf{y}) = \cos^{-1} \left(\frac{\langle \mathbf{x}, \mathbf{y} \rangle}{\|\mathbf{x}\| \|\mathbf{y}\|} \right) = \cos^{-1} \left(\frac{\sum_{i=1}^M x_i y_i}{\sqrt{\sum_{i=1}^M x_i^2} \sqrt{\sum_{i=1}^M y_i^2}} \right)$$

where \mathbf{x}, \mathbf{y} are two M-dimensional spectra in comparison.

This technique, when used on calibrated reference data, is relative intensive to illumination and albedo effects. This is illustrated in figure above, where an increase in the illumination has the effect of increasing the magnitude of the vector

$$\mathbf{y}' (\|\mathbf{y}'\| > \|\mathbf{y}\|),$$

but it has no effect to the angle formed between \mathbf{y}' (dashed line) and \mathbf{x} , so that $SAM(\mathbf{x}, \mathbf{y}) = SAM(\mathbf{x}, \mathbf{y}')$. The main advantage of the SAM is that is not affected from the light intensity differences between the spectral bands images of a spectral cube. For the processing of the data we developed an applet in Matlab where we applied SAM and several other known classification algorithms, such as K-means, C-means and Otsu Thresholding. Our ultimate goal is to provide quantitative diagnostic criteria for the pathologies of the endometrium, many of whom have been

categorized from the clinical findings until now. Below we will demonstrate cases where the color images are alike but the outcome of our analysis demonstrates great differences.

1. Normal endometrium versus endometriosis.

The images on the left are of an area of normal, healthy endometrium and the images on the right are of an area with endometriosis. The color images are not different except to as an expert physician whether the pseudo color images have clear differences.

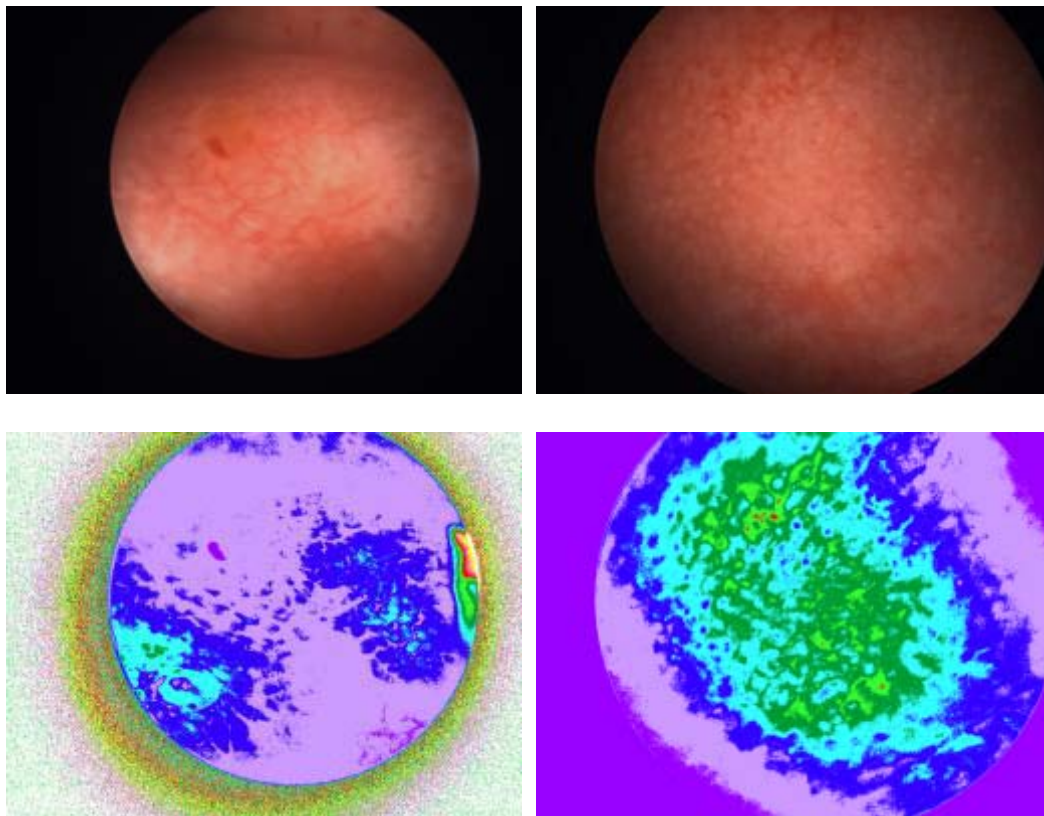


Figure 17. Normal Endometrium vs Endometriosis

2. Polyps versus Polyps

Polyps of the endometrium are treated as potentially neoplastic findings and are removed with no exceptions, although not all are dangerous. Gynecologists haven't yet found criteria for the potential of polyps. The color images show two different polyps from different patients that look alike. The pseudo color images created from our processing have different results in each case, signaling the different nature of each case.

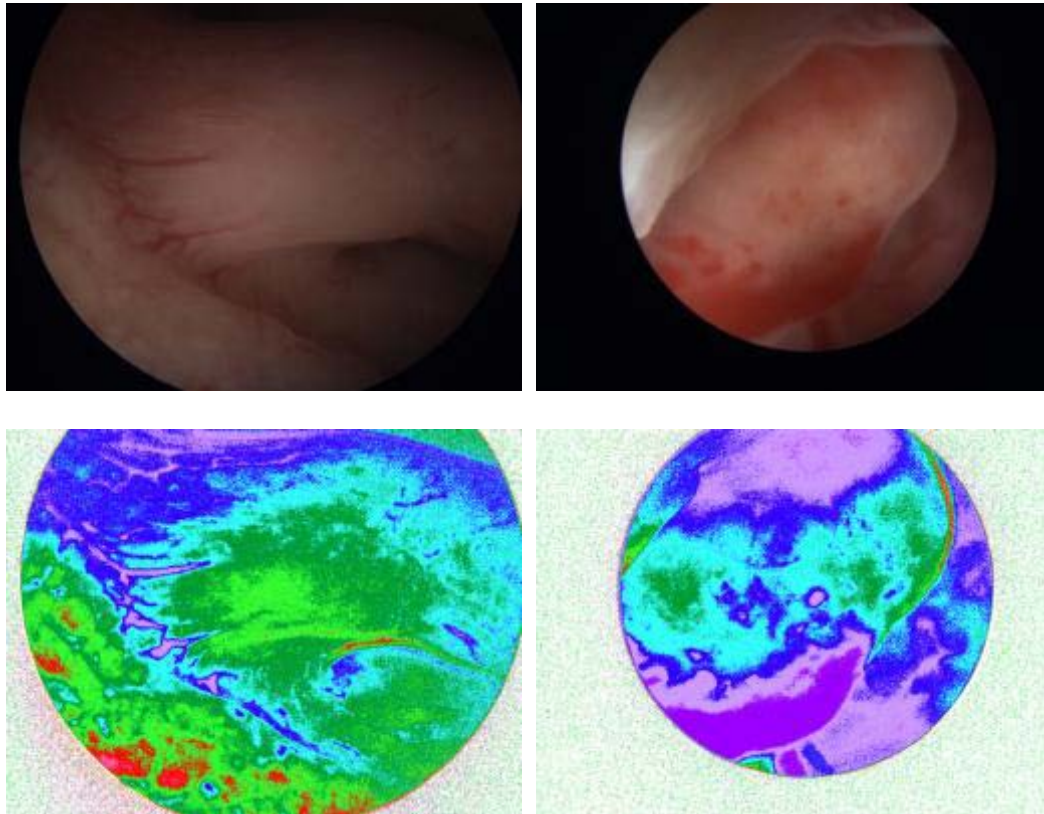


Figure 18. Different Polyps.

3. Polyps versus Polyps #2

The same case as previously with different polyps.

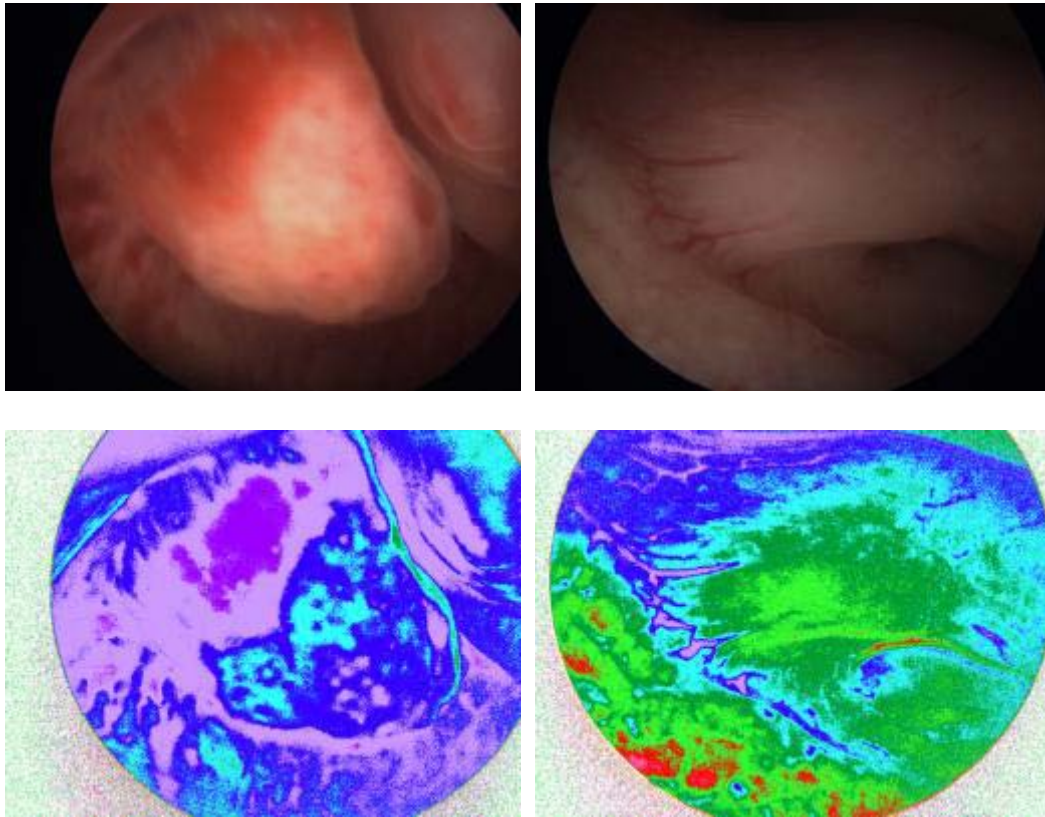


Figure 19. Different Polyps.

4. Polyps versus Polyps #3

The same case as previously with different polyps.

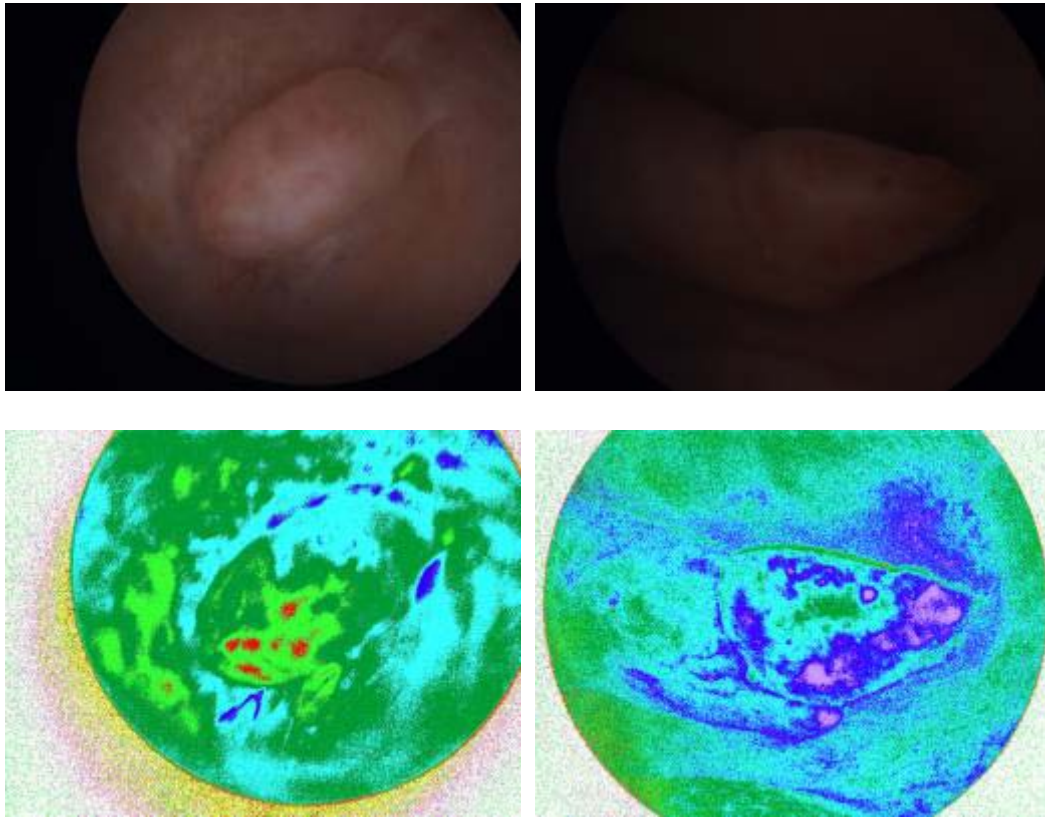


Figure 20. Different Polyps.

5. Normal endometrium versus undernourished endometrium

The normal endometrium on the left is very similar to the undernourished endometrium in naked eye. After processing, the pseudo color images offer rapid discrimination of the two.

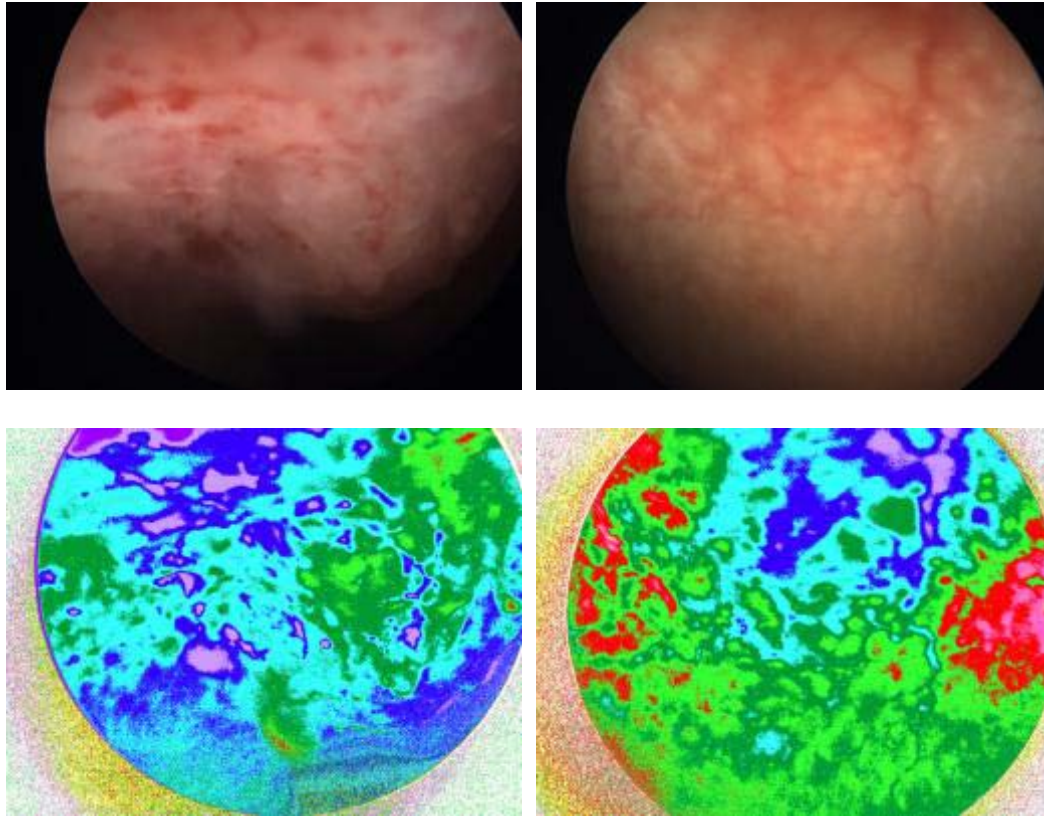


Figure 21. Normal versus undernourished endometrium

6. Undernourished endometrium versus hyperplasia of the endometrium

The undernourished endometrium resembles hyperplasia of the endometrium in white light endoscopy. The resulting pseudo color images state the difference clearly.

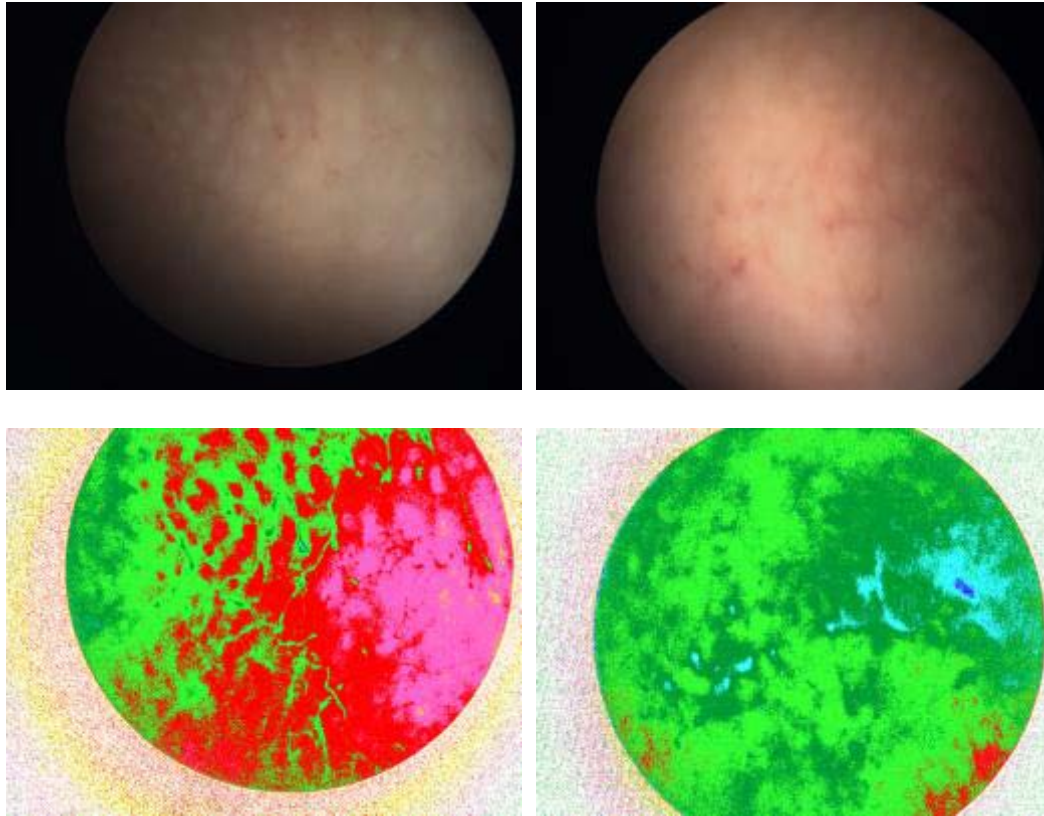


Figure 22. Undernourished endometrium versus hyperplasia.

Results – Future work

The ultimate purpose of this study is to provide quantified, objective identification of the abnormalities of the endometrium. There are a number of medical problems in the certain area that have not been addressed. The identification of precancerous lesions, the understanding the causes of DUB, the classification of the polyps in high risk and low risk and the mapping of infertility/fertility of the endometrium hope to find answer in the future and improve the lives and health of millions of women worldwide.

After the initial spectral classification and analysis was made, expert doctors of the area of gynecology and hysteroscopy that conducted the clinical trial and we discussed our results and data. The total number of spectral cubes acquired is not enough so that we can proceed to any generalization or quantification. Although, the classification was successful and categorized all spectral cubes according to pathology. The expert doctors agreed with our results in 99%. Figure 1 below show the total number of the results. Also, the users found the visualization of the pseudo color map very informative and comprehensive. The spectral bands visualization also enhanced various features as capillary vessels, surface morphological features, deep blood vessels and more.

As future work, more data have to be acquired in order to have a more sufficient sample for training and for validation of the classification algorithms. The classification itself has lot of room for improvement and more sophisticated classifiers such as the Spectral Correlation Mapper (SCM) need to be evaluated. The endoscopic system can be improved as well, with greater spectral range and even faster spectral cube acquisition rate.

Another approach would be to utilized algorithms for optimum spectral bands selection, reduce the total number of acquired spectra and develop simultaneous spectral imaging modalities for real time spectral cube display and classification.

Finally, the analysis of all data would possibly provide a quantitate characterization of endometrium abnormalities and new diagnostic tools will be created, providing objective noninvasive diagnosis, not subjective to the human errors.

Epithelium type (Cases)	Total cases Classified	Cases Doctor Agreed.
Normal Endometrium	21	21
Hyperplastic Endometrium	6	6
Endometriosis	6	5
Dysfunctional Uterus Bleeding	2	2
Polyps	20	20
Undeveloped Endometrium	5	5
Various Pathologies	14	14

Figure 1. Total Results.

References

1. Berci G, Brooks PG, Paz-Partlow M (1986) TV laparoscopy--a new dimension in visualization and documentation of pelvic pathology. *J Reprod Med* 31:585-588
2. Berci G, Cuschieri A (1986) *Practical laparoscopy*. Bailliere Tindall, London
3. Berci G, Davids J (1962) Endoscopy and television. *Br Med J* 1: 1610-1613
4. Berci G, Kont LA (1969) A new optical system in endoscopy with special reference to cystoscopy. *Br J Urol* 41:564
5. Berci G, Panish J, Morgenstern L (1973) Diagnostic colonoscopy and colonoscopic polypectomy. *Arch Surg* 106:818-819
6. Berci G, Schulman AG, Morgenstern L, Paz-Partlow M, Cuschieri A, Wood RA (1985) Television choledochoscopy. *Surg Gynecol Obstet* 160:176--177
7. Bevan JA (1868) Oesophagoscope. *Lancet* h 471
8. Bozzini PH (1806) Lichtleiter, eine Erfindung zur Anschauung innerer Teile und Krankheiten. *J Prak Heilk* 24:107
9. Classen M, Demling L (1974) Endoskopische Sphinkterotomie der Papilla Vateri and Steinextraktion aus dem Ductus choledochus. *Dtsch Med Wochenschr* 99:496
10. Cotton PB (1972) Cannulation of the papilla of Vater by endoscopy and retrograde cholangiopancreatography (ERCP). *Gut* 13:1014
11. Cuschieri A, Berci G (1990) *Laparoscopic biliary surgery*. Blackwell Scientific, London
12. Cuschieri A, Hall AW, Clark K (1978) Value of laparoscopy in diagnosis and management of pancreatic carcinoma. *Gut* 19:672
13. Dean AC, Shearman DJ (1970) Clinical evaluation of a new fiberoptic colonoscope. *Lancet* h 550
14. Desormeaux AJ (1865) *De l'endoscope et' des sos applications an diagnostic des affections de l'urethre et de la vessie*. Bailliere, Paris
15. Dubois F, Berthelots G, Levard H (1989) Choiecystectomy par coelioscopie. *Presse Med* 18:980
16. Fourestier M, Gladu A, Vulmiere J (1952) Perfectionnements a l'endoscopie medicale. *Press Med* 60:1292

17. Frangenheim H (1958) Die Bedeutung der Laparoskopie für die Gynekologische Diagnostik. Fortschr Med 76:451
18. Galsford WD (1976) Endoscopy of the small bowel. In: Berci G (ed) Endoscopy. Appleton-Century-Crofts, New York, pp 450--452
19. Grunfeld X (1879) Geschichte der Endoskopie und der endoskopischen Apparate. Mediz Jahrbuch, Wien, pp 237-291
20. Heel AS (1954) A new method of transporting optical images without aberrations. Nature 173:39
21. Henning N, Keilhack H (1938) Farbenphotography der Magenhöhle. Dtsch Med Wochenschr 64:1328
22. HLrschowitz BI, Curtis LE, Peters CW, et al. (1958) The fiberscope. Gastroenterology 35:50
23. Hoff HC (1928) Retrograde intubation of the cecum. Am J Roentg 20: 226
24. Holinger P, Brubaker PH (1941) The larynx, bronchi and esophagus in Kodachrome. J Biol Photogr Assoc 10:83
25. Hopkins HH, Kapany NS (1954) A flexible fiberscope. Nature 173:39
26. Jacobeus HC (19XX) Über die Möglichkeit die Zystoskopie bei
27. Kalk H, Bruhl W (1951) Leitfaden der Lapaxoskopie und Gastroskopie. Thieme, Stuttgart
28. Kelling G (1898) Gegliedertes, Winklig streckbares Gastroskope mit rotierbarem Sehprisma. Munch Med Wochenschr 49:1556
29. Kelling G (1902) Ueber Oesophagoskopie Gastroskopie and Kolioskopie. Munch Med Wochenschr 49:21-24
30. Killian G (1898) Über direkte Bronchoskopie. Munch Med Wochenschr 27:845
31. Koch H (1975) Endoscopic papillotomy. Endoscopy 7:89
32. Kussmaul J (1870) Über Magenspiegelung. Verb Naturforsch Ges Freiburg 5:112
33. Larnm H (1930) Biegsame Optische Geräte. Z Instr 50:579
34. Lunge F, Meltzing X (1898) Die Photography des Magininnerr. Munch Med Wochenschr 50:1585

35. Lewis BS, Waye JD (1985) Gastrointestinal endoscopy. 33:435-438
36. McCune WS, Shorb PE, Moscovitz H (1968) Endoscopic cannulation of the ampulla of Vater: a preliminary report. *Ann Surg* 167:752
37. Mikulicz J (1881) *Über Gastroskopie und Ösophagoskopie*. Wien Med Presse 45:1405
38. Milne JS (1970) *Surgical instruments in Greek and Roman times*. August M. Kelley, New York
39. Muhe E (1986) Die Erste Cholecystectomy durch das Laparoscope. *Langenbecks Arch* 369:804
40. Nitze M (1893) Zur Photographie der menschlichen Harnblase. *Meal Wochenschr* 2:744
41. Feng L, Wu YL, Zhu Q, Zhong J. Argon plasma coagulator in the endoscopic treatment of 78 patients with gastrointestinal polyps. *Shijie Huaren Xiaohua Zazhi* 2000; 8: 1336-1338
42. Cheng YS, Shang KZ. Gastrointestinal imageology in China: a 50 year evolution. *Shijie Huaren Xiaohua Zazhi* 2000; 8: 1225-1232
43. Feng L, Wu YL, Zhong J, Zhu Q. Argon plasma coagulation in the endoscopic treatment of verrucosal gastritis. *Shijie Huaren Xiaohua Zazhi* 2000; 8: 1332-1335
44. Li CZ, Cheng LF, Gu Y, Wang ZQ, Yang YS, Liu QS, Linghu EQ. Obliteration effect of photodynamic therapy on small veins: an experimental study. *Zhongguo Jiguang Yixue Zazhi* 2003; 12: 5-8
45. Wan XQ, Wang CP, Cheng K, Li LL, Xu SZ, Li CS, Yang ZQ. Study on the killing effect of in vitro photodynamic therapy using delta-aminolevulinic acid on HEP-2 cells. *Zhongguo Jiguang Yixue Zazhi* 2000; 9: 102-104
46. ChenWH, Yu JX, Yao JZ, ShenWD, Liu JF, Xu DY. Pharmacokinetic studies on hematoporphyrin monomethyl ether: A new promising drug for photodynamic therapy of tumors. *Zhongguo Jiguang Yixue Zazhi* 2000; 9: 105-108
47. Liu FG, Gu Y, Fu QT, Pan YM, Li JH. Absorptive characteristics of HMME and HpD in chicken comb skin and vascular endothelial cells. *Zhongguo Jiguang Yixue Zazhi* 2001; 10: 9-12

48. Ritz JP, Roggan A, Isbert C, Müller G, Buhr HJ, Germer CT. Optical properties of native and coagulated porcine liver tissue between 400 and 2400nm. *Lasers Surg Med* 2001; 29: 205-212
49. Qu J, MacAulay C, Lam S, Palcic B. Optical properties of normal and carcinomatous bronchial tissue. *Appl Opt* 1994; 33: 7397-7405
50. Liu G, Xing D, Wang HM, Wu J. Study of protein in human gallstones by fourier transform infrared spectroscopy and surface-enhanced Raman spectroscopy. *Guangxue Xuebao* 2002; 22: 441-446
51. Sankaran V, Everett MJ, Maitland DJ, Walsh JT Jr. Comparison of polarized-light propagation in biological tissue and phantoms. *Opt Lett* 1999; 24: 1044-1046
52. Kim AD, Ishimaru A. Optical diffusion of continuous-wave, pulsed, and density waves in scattering media and comparisons with radiative transfer. *Appl Opt* 1998; 37: 5313-5319
53. Li J, Li SR, Cao JB, Gao G. Laser-induced fluorescence spectrum of colon cancer in vivo. *Shijie Huaren Xiaohua Zazhi* 1999; 7: 164-165
54. Liao XH, Chen ZL, Tang JM, Luo YS. An experimental study on optical properties of rat viscera. *Jiguang Zazhi* 2002; 23: 74
55. Li BH, Xie SS, Lu ZK. Time-resolved spectroscopy for human esophageal and breast tissues in vitro. *Guangdianzi Jiguang* 2002;13: 1071-1073
56. Gorti S, Tone H, Imokawa G. Triangulation method for determining capillary blood flow and physical characteristics of the skin. *Appl Opt* 1999; 38: 4914-4929
57. Van der Putten WJM, Van Gemert MJC. A modelling approach to the detection of subcutaneous tumours by haematoporphyrinderivative fluorescence. *Phys Med Biol* 1983; 28: 639-645
58. Chen R, Xie SS, Chen YJ, Wang HP. Transmission properties of ray in blood in laser irradiation blood therapy. *Guangdianzi Jiguang* 2001; 12: 1310-1312
59. Wu GL, Luo QM, Zeng SQ, Mu CP, Liu XD. Photon diffusion theory and its application in biomedicine. *Guangdianzi Jiguang* 2001; 12: 323-328
60. Cheng SY, Huang JH, Lin WX, Zhang G, Huang XJ, Huang CH, Shen HY. Problems in measuring attenuation coefficient μ_t of blood by direct measurement method. *Guangzi Xuebao* 2001; 30: 1045-1049

61. Delpy D.T., Cope M., Van der Zee P., Arridge S.R., Wray S., Wyatt J.S. (1988) 'Estimation of optical path length through tissue from direct time of flight measurement', *Physics in Medicine and Biology*, 33, 1433-1442.
62. Delpy D.T., Arridge S.R., Cope M., Edwards A.D., Reynolds E.O.R., Richardson C.E., Wray S., Wyatt J.S., Van der Zee P. (1989) 'Quantitation of path length in optical spectroscopy', *Advances in Experimental Medicine and Biology*, 247, 41-46.
63. Gaushouse, Non-linear least squares fit (Dec. 1965) Univ. of Wisconsin Computing Centre.
64. Groenhuis, R.A.J., Ferwerda, H.A., Ten Bosch, J.J. (1984a) 'Scattering and absorption of turbid materials determined from reflection measurements. 1: theory', *Applied Optics*, 22, 2456-2462.
65. Groenhuis, R.A.J., Ferwerda, H.A., Ten Bosch, J.J. (1984b) 'Scattering and absorption of turbid materials determined from reflection measurements. 2: Measuring method and calibration', *Applied Optics*, 22, 2463-2467.
66. Van der Zee P., Delpy D.T. (1987) 'Simulation of the point spread function for light in tissue by a Monte Carlo method' in: *Advances in Experimental Medicine and Biology*, Eds. Silver I A, Silver A, New York, Plenum Press, 215, 179-192.
67. Van der Zee P., Delpy D.T. (1988a) 'Computed point spread functions for light in tissue using a measured volume scattering function' in: *Advances in Experimental Medicine and Biology*, Eds. Mochizuki M, Honig C R, Koyama T, Goldstick T K, Bruley T F, New York, Plenum Press, 222, 191-197.
68. Van der Zee, P., Nalder, C., Delpy, D.T., Arridge, S.R., Cope, M. (1988b) 'Optical characterisation of tissue for near infrared light', *International conference on PDT and Medical Laser Applications*, London July 19-21, *Lasers in Medical Science*, Abstract Supplement, 194.
69. Van der Zee, P., Arridge, S.R., Cope, M., Delpy, D.T. (1990) 'The effect of optode positioning on optical pathlength in near infrared spectroscopy of brain', in: *Advances in Experimental Medicine and Biology*, Piiper, J., Goldstick, T.K., Meyer, M., Eds., Plenum Press, New York, 277, 79-84.
70. Wyatt J.S., Cope M., Delpy D.T., Van der Zee P., Arridge S.R., Edwards A.D., Reynolds E.O.R. (1990) 'Measurement of optical path length for cerebral near-infrared spectroscopy in newborn infants', *Developmental Neuroscience*, 12, 140-144.

81. US Patent 5647368 - Imaging system for detecting diseased tissue using native fluorescence in the gastrointestinal and respiratory tract (July 1997)
82. Medscape www.medscape.com
83. From Nature Clinical Practice Gastroenterology & Hepatology "What is the Value of Early Endoscopy in Upper Gastrointestinal Bleeding?" Posted 10/13/2006
84. Endoscopy. From Dekker E, van den Broek EJ, Reitsma JB, et al. Narrow-band imaging compared with conventional colonoscopy for the detection of dysplasia in patients with longstanding ulcerative colitis 2007;39:216-221. Republished with permission of Thieme Publishers.
85. Journal of Minimally Invasive Gynecology (2007) 14, 393-394 "Narrow band Imaging in Endometriosis"
86. Journal of Minimally Invasive Gynecology (2007) 14, 393-394 "Narrow band Imaging in Endometriosis" pictures are From the East Kent Hospitals NHS Trust, London, United Kingdom
87. Nakayoshi T, Tajiri H, Matsuda K, Kaise M, Ikegami M, Sasaki H. Magnifying endoscopy combined with narrow band imaging system for early gastric cancer: correlation of vascular pattern with histopathology. Endoscopy. 2004;36: L080-1084.
88. Machida H, Sano Y, Hamamoto Y, et al. Narrow-band imaging in the diagnosis of colorectal mucosal lesions: a pilot study. Endoscopy. 2004; 36:1094-1098.
89. Gono K, Obi T, Yamaguchi M, Ohyama N, Machida H, Sano Y, et al . Appearance of enhanced tissue features in narrow-band endoscopic imaging. J Biomed Opt 2004;9:568-77.
90. Gono K, Yamazaki K, Doguchi N. Endoscopic observation of tissue by narrowband illumination. Optical Rev 2003;10:1-5.
91. Gono K, Yamaguchi M, Ohyama N. Improvement of image quality of the electroendoscope by narrowing spectral shapes of observation light. Proc Int Congress Imaging Sci 2002;5:399-400.
92. Lambert R. Diagnosis of esophagogastric tumors. Endoscopy 2002;34:12938 [PUBMED]
93. Gono K, Obi T, Yamaguchi M, Ohyama N, Machida H, Sano Y, et al . Appearance of enhanced tissue features in narrow-band endoscopic imaging. J Biomed Opt 2004;9:568-77.

94. Gono K, Yamazaki K, Doguchi N. Endoscopic observation of tissue by narrowband illumination. *Optical Rev* 2003;10:1-5.
95. Gono K, Yamaguchi M, Ohyama N. Improvement of image quality of the electroendoscope by narrowing spectral shapes of observation light. *Proc Int Congress Imaging Sci* 2002;5:399-400.
96. Sambongi M, Igarashi M, Obi T. Analysis of spectral reflectance of mucous membrane for endoscopic diagnosis. *Med Physics* 2000;27:1396.
97. http://www.medscape.com/viewarticle/568371_4
98. IEEE JOURNAL OF SELECTED TOPICS IN QUANTUM ELECTRONICS, VOL. 14, NO. 1, JANUARY/FEBRUARY 2008 "Multifunctional Endoscopic Imaging System for Support of Early Cancer Diagnosis" K. Gono
99. DaCosta RS, Wilson BC, Marcon NE. Optical techniques for the endoscopic detection of dysplastic colonic lesions. *Curr Opin Gastroenterol* 2005; 21:70-79.
100. Department of Endoscopy, Hiroshima University Hospital. Y. Sano, Y. Saito, K. I. Fu, T. Matsuda, T. Uraoka, N. Kobayashi, H. Ito, H. Machida, J. Iwasaki, F. Emura, M. Hanafusa, T. Yoshino, S. Kato, and T. Fujii, "Efficacy of magnifying chromoendoscopy for the differential diagnosis of colorectal lesions," *Dig. Endosc.*, vol. 17, pp. 105–116

Appendix A

```

// USER Definitions
.EQU VERSION_M1='1'
.EQU VERSION_M2='0'
.EQU VERSION_M3='0'
.EQU VERSION_M4='2'
#define MY_IDENT(X) .db #X, '\r',0
#define DEVICE_HAS_BREAK
#define DEVICE_HAS_CONT_BREAK
#ifdef DEVICE_IS_IN_TEST
#define F_CPU 16000000
#else
#define F_CPU 16000000
#endif
#define U_BAUD 19200
#define Motor_p_us 33000
#define v_tccrlb 0x1
#define v_TCNT1H 0xe9
.listmac
// Definitions for RS232 functions
#define U_UBRR (F_CPU/(16*U_BAUD))-1
// Definitions for waiting functions
#define W_1MILLISEC ((F_CPU/1000)-402)/403+1
#define W_1MILLISECA ((int((F_CPU/1000)-(403*(int(W_1MILLISEC)-1)+414)))-2)/3+1
#define W_10USEC int(((F_CPU/100000)-11)/13)
#define W_10USECNop ((F_CPU/100000)-11)%13
.INCLUDE "m162def.inc"
.EQU nYBYTE1 = 0B00000101
.EQU nYBYTE2 = 0B00000100
.EQU nYBYTE3 = 0B00000110
.EQU nYBYTE4 = 0B00000010
.EQU nYBYTE5 = 0B00001010
.EQU nYBYTE6 = 0B00001000
.EQU nYBYTE7 = 0B00001001
.EQU nYBYTE8 = 0B00000001
.EQU PALMOI_PLH = 8
/****Leds *****/
.EQU LED1_PORT = PORTB
.EQU LED1_DIR = DDRB
.EQU LED1_BIT = 0
.EQU LED2_PORT = PORTB
.EQU LED2_DIR = DDRB
.EQU LED2_BIT = 1
/****Motor*****/
.EQU MOTOR1_ENABLE_PORT = PORTA
.EQU MOTOR1_ENABLE_DIR = DDRA
.EQU MOTOR1_ENABLE_PIN = 4
.EQU MOTOR1_PORT = PORTA
.EQU MOTOR1_DIR = DDRA
.EQU MOTOR2_ENABLE_PORT = PORTC
.EQU MOTOR2_ENABLE_DIR = DDRC
.EQU MOTOR2_ENABLE_PIN = 4
.EQU MOTOR2_PORT = PORTC
.EQU MOTOR2_DIR = DDRC
//κοινά και στα δύο μωτέρ
.EQU MOTOR_MASK = 0B11110000
.EQU MOTOR_DDR = 0B00001111
/**** Terminators *****/
.EQU MOTOR1_CHK_LEFTPORT = PORTd
.EQU MOTOR1_CHK_LEFTDIR = DDRd
.EQU MOTOR1_CHK_LEFTPIN = PIND
.EQU MOTOR1_CHK_LEFTBIT = 4
.EQU MOTOR1_CHK_RIGHT_PORT = PORTd
.EQU MOTOR1_CHK_RIGHT_DIR = DDRd
.EQU MOTOR1_CHK_RIGHT_PIN = PIND
.EQU MOTOR1_CHK_RIGHT_BIT = 5
.EQU MOTOR2_CHK_LEFTPORT = PORTd
.EQU MOTOR2_CHK_LEFTDIR = DDRd
.EQU MOTOR2_CHK_RIGHTPIN = PIND
.EQU MOTOR2_CHK_RIGHTBIT = 7
//Check is 5V unpressed and goes to 0
when pressed
;Bit in Count_Step for Direction
.EQU BIT_DIRECTION1 = 4
.EQU BIT_DIRECTION2 = 5
.DEF PLHUOS_SER_DATA = R6
.DEF TVRA_MOVE_LOW = R9
.DEF TVRA_MOVE_high = R10
.DEF FRENO1_COUNT = R11
.DEF FRENO2_COUNT = R12
.DEF SPEED_TIMERH = R14
.DEF G_ACC1 = R16
.DEF G_ACC2 = R17
.DEF I_ACC1 = R18
.DEF G_ACC3 = R19
.DEF COUNT1_STEP = R20
.DEF COUNT2_STEP = R21
.DEF BITFIELD1 = R22
.DEF BITFIELD2 = R23
/* bits in BITFIELD1 */
.EQU Bit_In_Serial = 0
Bit_From_Serial= 1
Bit_Error_drive= 2
.EQU bit_phga = 3
.EQU einai_se_freno = 4
.EQU Bit_drive_mot1= 0
.EQU Bit_drive_mot2= 1
;*****
; MACRO :__WAIT_MILLISECONDS
; Description:Wait # milliseconds
; e.x __WAIT_MILLISECONDS 10
; Input : No of Milliseconds as parameter
; Output :NONE
; use Registers :G_ACC2
; Modify Registers :NONE
; Modify CPU :NONE
; Modify Ports :NONE
;*****
.MACRO __WAIT_MILLISECONDS
push G_ACC2
LDI G_ACC2,LOW(@)
__WAIT_MILLISECONDS_LOOP:
rcall Wait1millisec
DEC G_ACC2
BRNE __WAIT_MILLISECONDS_LOOP
pop G_ACC2
.ENDMACRO
;*****
; MACRO :__WAIT_SECONDS
; Description:Wait # seconds
; e.x __WAIT_SECONDS 10
; max number of seconds 30
; Input : No of seconds as parameter
; Output :NONE
; use Registers :G_ACC2,XL,XH,r0,r1,R21,R22
; Modify Registers :NONE
; Modify CPU :NONE
; Modify Ports :NONE
;*****
.MACRO __WAIT_SECONDS
push G_ACC2
push XL
push XH

```

```

        push r0
        push r1
        PUSH R21
        PUSH R22
        LDI G_ACC2,LOW(@0)
        LDI r21,3
        LDI r22,0xe8
        MUL G_ACC2,r22
        push r0
        push r1
        MUL G_ACC2,r21
        pop xh
        add xh,r0
        pop xl
__WAIT_SECONDS_LOOP:
        rcall Wait1millisec
        SBIW XL,1
        BRNE __WAIT_SECONDS_LOOP
        POP R22
        POP r21
        pop r1
        pop r0
        pop xh
        pop xl
        pop G_ACC2
.ENDMACRO
.MACRO mac_KANE_PALMO
        PUSH YL ; used in
GetByteFromMemory
        PUSH YH
        PUSH G_ACC3
        PUSH G_ACC1
        MOV G_ACC3,Count@0_Step
        ANDI G_ACC3,0b00000111
        PUSH G_ACC3
// GetByteFromMemory
        LDI
YL,Low(MOTOR@0_Pulses_Memory)
        LDI
YH,High(MOTOR@0_Pulses_Memory)
        ADD YL,G_ACC3
        LD G_ACC3,Y
// GetByteFromMemory
// dLedg_Change
        IN G_ACC1,MOTOR@0_PORT
        ANDI G_ACC1,MOTOR_MASK
        sts LAST_MOTOR@0_VALUE,G_ACC3
        OR G_ACC1,G_ACC3
        OUT MOTOR@0_PORT,G_ACC1
        POP G_ACC3
        NOP
        NOP
        SBRS COUNT@0_STEP,BIT_DIRECTION@0
        RJMP KanePalmo_r
KanePalmo_L:
        INC G_ACC3
        CPI G_ACC3,Palmoi_plh
        BRNE KanePalmo_Telos_e
        CLR G_ACC3
        RJMP KanePalmo_Telos_e
KanePalmo_r:
        TST G_ACC3
        BREQ KanePalmo_Ra
        DEC G_ACC3
        RJMP KanePalmo_Telos_e
KanePalmo_Ra:
        LDI G_ACC3,Palmoi_Plh-1
KanePalmo_Telos_e:
        ANDI
COUNT@0_STEP,(1<<BIT_DIRECTION@0) //
0b00001000
        OR Count@0_Step,G_ACC3
        RCALL Wait10usec
        POP G_ACC1
        POP G_ACC3
        POP YH
        POP YL
.ENDMACRO
.MACRO INITMOTORMEMORY
        LDI
YL,low(MOTOR@0_Pulses_Memory)
        LDI
YH,high(MOTOR@0_Pulses_Memory)
        LDI G_ACC3,nYBYTE1
        ST Y+,G_ACC3
        LDI G_ACC3,nYBYTE2
        ST Y+,G_ACC3
        LDI G_ACC3,nYBYTE3
        ST Y+,G_ACC3
        LDI G_ACC3,nYBYTE4
        ST Y+,G_ACC3
        LDI G_ACC3,nYBYTE5
        ST Y+,G_ACC3
        LDI G_ACC3,nYBYTE6
        ST Y+,G_ACC3
        LDI G_ACC3,nYBYTE7
        ST Y+,G_ACC3
        LDI G_ACC3,nYBYTE8
        ST Y+,G_ACC3
        LDI
YL,Low(Current@0_Count_high)
        LDI
YH,High(Current@0_Count_high)
        CLR G_ACC1
        ST Y+,G_ACC1
        .EndMACRO
.MACRO INTERRUPT_PROLOG
        push i_accl
        push G_ACC1
        push G_ACC2
        in i_accl,sreg
        push i_accl
.ENDMACRO
.MACRO INTERRUPT_EPILOG
        pop i_accl
        out sreg,i_accl
        pop G_ACC2
        pop G_ACC1
        pop i_accl
.ENDMACRO
/*****
macro Moter_right
Moter_left
Ledr_On Ledr_Off
Ledg_On Ledg_Off
input -
output -
change REGISTERS -
*****/
.MACRO send_rs232
        push g_accl
        ldi g_accl,@0
        rcall send_char
        pop g_accl
.ENDMACRO
.MACRO Moter1_right
// rcall send_right
        SBRS Count1_Step,BIT_DIRECTION1
        rjmp motor1_right_a
        CBR
Count1_Step,EXP2(BIT_DIRECTION1)
        cpi Count1_Step,1
        breq motrol_is_1
        cpi Count1_Step,0
        breq motrol_is_0

```

```

        dec Count1_Step
        dec Count1_Step
        rjmp motor1_right_a
motrol_is_1:
        ldi Count1_Step,7
        rjmp motor1_right_a
motrol_is_0:
        ldi Count1_Step,6
motor1_right_a:
        nop
.ENDMACRO
.MACRO      Moter1_left
//          rcall send_left
        SBRc   Count1_Step,BIT_DIRECTION1
        rjmp  motor1_left_exit
        inc Count1_Step
        inc Count1_Step
        cpi Count1_Step,8
        brlo motor1_left_a
        push g_accl
        ldi g_accl,8
        sub Count1_Step,g_accl
        pop g_accl
motor1_left_a:
        SBR
Count1_Step,EXP2(BIT_DIRECTION1)
motor1_left_exit:
.ENDMACRO
.MACRO      Moter2_right
        SBRs   Count2_Step,BIT_DIRECTION1
        rjmp  motor2_right_exit
        CBR
Count2_Step,EXP2(BIT_DIRECTION2)
        cpi Count2_Step,1
        breq motro2_is_1
        cpi Count2_Step,0
        breq motro2_is_0
        dec Count2_Step
        dec Count2_Step
        rjmp  motor2_right_a
motro2_is_1:
        ldi Count2_Step,7
        rjmp  motor2_right_a
motro2_is_0:
        ldi Count2_Step,6
motor2_right_a:
motor2_right_exit:
.ENDMACRO
.MACRO      Moter2_left
        SBRc   Count2_Step,BIT_DIRECTION1
        rjmp  motor2_left_exit
        inc Count2_Step
        inc Count2_Step
        cpi Count2_Step,8
        brlo motor2_left_a
        push g_accl
        ldi g_accl,8
        sub Count2_Step,g_accl
        pop g_accl
motor2_left_a:
        SBR
Count2_Step,EXP2(BIT_DIRECTION2)
motor2_left_exit:
.ENDMACRO
.MACRO      dLed_Change
        SBIC   Led@0_Port ,Led@0_bit
        rjmp  led_is_off
        SBI    Led@0_Port ,Led@0_bit
        rjmp  end_g_c
led_is_off:
        CBI    Led@0_Port ,Led@0_bit
end_g_c:
.ENDMACRO
.MACRO      dLed1_Change
        SBIC   Led1_Port ,Led1_bit
        rjmp  led1_is_off
        SBI    Led1_Port ,Led1_bit
led1_is_off:
        CBI    Led1_Port ,Led1_bit
end_g_c:
.ENDMACRO
.MACRO      dLed2_Change
        SBIC   Led2_Port ,Led2_bit
        rjmp  led2_is_off
        SBI    Led2_Port ,Led2_bit
        rjmp  end_g_c
led2_is_off:
        CBI    Led2_Port ,Led2_bit
end_g_c:
.ENDMACRO
.MACRO      Led1_On
        SBI    Led1_Port ,Led1_bit
.ENDMACRO
.MACRO      Led1_Off
        CBI    Led1_Port ,Led1_bit
.ENDMACRO
;*****
; macro          :WaitUs
; Description: waits # usec #>10
;              the waiting time is less
;              than # (0 ... 12) Cycles
; Input         :@0
; Output        :NONE
; use Registers :G_ACC1
; Modify Registers :NONE
; Modify CPU    :NONE
; Modify Ports  :NONE
;*****
.MACRO      WaitUs
#undef W_aUSEC
#undef W_aUSECmod
#define W_aUSEC
int(((F_CPU*@0/4000000)-1)/4)
#define W_aUSECmod
(((F_CPU*@0/4000000)-1)%4)
        PUSH   G_ACC1
        LDI    G_ACC1,W_aUSEC
Pointu_c:
        RCALL  Wait10
        nop
        nop
        nop
        DEC    G_ACC1
        BRNE   Pointu_c
        POP    G_ACC1
#undef W_aUSEC
#undef W_aUSECmod
.ENDMACRO
.CSEG
.org 0x0000
rjmp inRESET
.if DEFINED INT0addr
.ORG INT0addr
LABELb:
        reti
.endif
.if DEFINED INT1addr
.ORG INT1addr
        reti
.endif
.if DEFINED ICPLADDR
.ORG ICPLADDR
        RETI
.endif
.if DEFINED OC1AADDR
.ORG OC1AADDR
        RETI
.endif
.if DEFINED OVFLADDR
.ORG OVFLADDR
        RJMP  inOVFLADDR
.endif
.if DEFINED OVFOADDR

```

```

.ORG OVFOADDR
    RJMP    inOVFOADDR
.endif
.if DEFINED URXC0ADDR
.ORG URXC0ADDR
    RJMP    inURXCADDR
.endif
.if DEFINED UDRE0ADDR
.ORG UDRE0ADDR
    reti
.endif
.if DEFINED UTXC0ADDR
.ORG UTXC0ADDR
    reti
.endif
.if DEFINED URXCADDR
.ORG URXCADDR
    RJMP    inURXCADDR
.endif
.if DEFINED UDREADDR
.ORG UDREADDR
    reti
.endif
.if DEFINED UTXCADDR
.ORG UTXCADDR
    reti
.endif
.if DEFINED ACIADDR
.ORG ACIADDR
    reti
.endif
.if DEFINED PCIaddr
.ORG PCIaddr
    reti
.endif
.if DEFINED OC1Baddr
.ORG OC1Baddr
    RETI
.endif
.if DEFINED OC0Aaddr
.ORG OC0Aaddr
    RETI
.endif
.if DEFINED OC0Baddr
.ORG OC0Baddr
    RETI
.endif
.if DEFINED USI_STARTaddr
.ORG USI_STARTaddr
    RETI
.endif
.if DEFINED USI_OVFaddr
.ORG USI_OVFaddr
    RETI
.endif
.if DEFINED ERDYaddr
.ORG ERDYaddr
    RETI
.endif
.if DEFINED WDTaddr
.ORG WDTaddr
    RETI
.endif
.if DEFINED FAULT_PROTaddr
.org FAULT_PROTaddr
    RETI
.endif
.if DEFINED INT2addr
.org INT2addr
    RETI
.endif
.if DEFINED INT3addr
.org INT3addr
    RETI
.endif
.if DEFINED INT4addr
.org INT4addr
    RETI
.endif
    RETI
.endif
.if DEFINED INT5addr
.org INT5addr
    RETI
.endif
.if DEFINED INT6addr
.org INT6addr
    RETI
.endif
.if DEFINED INT7addr
.org INT7addr
    RETI
.endif
.if DEFINED PCI0addr
.org PCI0addr
    RETI
.endif
.if DEFINED PCI1addr
.org PCI1addr
    RETI
.endif
.if DEFINED PCI2addr
.org PCI2addr
    RETI
.endif
.if DEFINED PCI3addr
.org PCI3addr
    RETI
.endif
.if DEFINED OC2Aaddr
.org OC2Aaddr
    RETI
.endif
.if DEFINED OC2Baddr
.org OC2Baddr
    RETI
.endif
.if DEFINED OV2addr
.org OV2addr
    RETI
.endif
.if DEFINED SPIaddr
.org SPIaddr
    RETI
.endif
.if DEFINED ADCCaddr
.org ADCCaddr
    RETI
.endif
.if DEFINED TWIaddr
.org TWIaddr
    RETI
.endif
.if DEFINED SPMRaddr
.org SPMRaddr
    RETI
.endif
.if DEFINED OC0addr
.org OC0addr
    RETI
.endif
.if DEFINED OC1Caddr
.org OC1Caddr
    RETI
.endif
.if DEFINED ICP3addr
.org ICP3addr
    RETI
.endif
.if DEFINED OC3Aaddr
.org OC3Aaddr
    RETI
.endif
.if DEFINED OC3Baddr
.org OC3Baddr
    RETI

```

```

.endif
.if DEFINED OC3Caddr
.org OC3Caddr
    RETI
.endif
.if DEFINED OVf3addr
.org OVf3addr
    RETI
.endif
.if DEFINED URXC1addr
.org URXC1addr
    RETI
.endif
.if DEFINED UDRE1addr
.org UDRE1addr
    RETI
.endif
.if DEFINED UTXC1addr
.org UTXC1addr
LABELa:
    RETI
.endif
.if DEFINED INT_VECTORS_SIZE
.org INT_VECTORS_SIZE
.endif
inRESET:
    CLI
    CLR    ZL
    OUT    EECR,ZL
; INTERRUPT VECTORS ARE PLACED
; AT THE START OF FLASH
    LDI    ZH,1
    OUT    GICR,ZH
    OUT    GICR,ZL
    OUT    MCUCR,ZL
.if DEFINED EMCUCR
    OUT    EMCUCR,ZL
.endif
; DISABLE WATCHDOG
    LDI    ZH,0x18
    OUT    WDTCR,ZH
    OUT    WDTCR,ZL
; CLEAR R2-R14
    LDI    R24,13
    LDI    R26,2
    CLR    R27
__CLEAR_REG:
    ST    X+,ZL
    DEC    R24
    BRNE  __CLEAR_REG
; CLEAR SRAM
    LDI    R24,LOW(SRAM_SIZE)
    LDI    R25,HIGH(SRAM_SIZE)
    LDI    XL,LOW(SRAM_START)
    LDI    XH,HIGH(SRAM_START)
__CLEAR_SRAM:
    ST    X+,ZL
    SBIW  R24,1
    BRNE  __CLEAR_SRAM
; STACK POINTER INITIALIZATION
    LDI    ZL,LOW(RamEnd)
    OUT    SPL,ZL
    LDI    ZL,HIGH(RamEnd)
    OUT    SPH,ZL
//Crystal Oscillator division factor: 1
.if DEFINED CLKPR
    LDI    ZL,LOW(128)
    STS    CLKPR,R30
    LDI    ZL,LOW(0)
    STS    CLKPR,R30
.endif
    ldi    zh,High(2*flash_Positions)
    ldi    zl,low(2*flash_Positions)
    lpm    xl,z+
    cpi    xl,0xff
    brne  is_ok
    lpm    xl,z+
    cpi    xl,0xff
    brne  is_ok
    jmp    LARGEBOOTSTART
is_ok:
;OSCCAL INITIALIZATION
    clr    xh
    clr    xl
    rcall  EEPROM_Read_byte
    cpi    z1,4
    brne  set_eeeprom_osc
    clr    xh
    ldi    xl,1
    rcall  EEPROM_Read_byte
    mov    g_accl,z1
    rjmp  set_osc

set_eeeprom_osc:
    clr    xh
    clr    xl
    LDI    z1,4
    rcall  EEPROM_write_Byte
    clr    xh
    ldi    xl,1
    LDI    z1,LOW(0X56)
    rcall  EEPROM_write_Byte
    mov    g_accl,z1
set_osc:
    OUT    OSCCAL,G_ACC1
    sts    OSCCAL,G_ACC1
    rjmp  inReset1
;*****
; function :Wait10
; Description:Wait 10 cycles
; Input :NONE
; Output :NONE
; use Registers :NONE
; Modify Registers :NONE
; Modify CPU :NONE
; Modify Ports :NONE
;*****
Wait10:
    nop
    nop
    nop
    RET
;*****
; function :Wait20
; Description:Wait 20 cycles
; Input :NONE
; Output :NONE
; use Registers :G_ACC1
; Modify Registers :NONE
; Modify CPU :NONE
; Modify Ports :NONE
;*****
Wait20:
    PUSH    G_ACC1
    LDI    G_ACC1,0X3
Wait20_1:
    DEC    G_ACC1
    BRNE  Wait20_1
    POP    G_ACC1
    RET
;*****
; function :Wait400
; Description:Wait 400 cycles
; Input :NONE
; Output :NONE
; use Registers :G_ACC1
; Modify Registers :NONE
; Modify CPU :NONE
; Modify Ports :NONE
;*****
Wait400:
    PUSH    G_ACC1
    LDI    G_ACC1,0X81

```



```

.endif
sbi LED1_DIR,LED1_BIT
sbi LED2_DIR,LED2_BIT
sbi
MOTOR1_ENABLE_DIR,MOTOR1_ENABLE_PIN
sbi
MOTOR1_ENABLE_PORT,MOTOR1_ENABLE_PIN
sbi
MOTOR2_ENABLE_DIR,MOTOR2_ENABLE_PIN
sbi
MOTOR2_ENABLE_PORT,MOTOR2_ENABLE_PIN
in g_acc1,MOTOR1_DIR
ori g_acc1,MOTOR_DDR
out MOTOR1_DIR,g_acc1
in g_acc1,MOTOR2_DIR
ori g_acc1,MOTOR_DDR
out MOTOR2_DIR,g_acc1
//pullups for buttons
sbi
MOTOR1_CHK_LEFTPORT,MOTOR1_CHK_LEFTBIT
sbi
MOTOR1_CHK_RIGHT_PORT,MOTOR1_CHK_RIGHT_
BIT
sbi
MOTOR2_CHK_LEFTPORT,MOTOR2_CHK_LEFTBIT
sbi
MOTOR2_CHK_RIGHT_PORT,MOTOR2_CHK_RIGHT_
BIT
pop G_ACC1
ret
;*****
; function :init_232
; Description: Initilize RS232
; Input :None
; Output :None
; use Registers :G_ACC1
; Modify Registers :NONE
; Modify CPU :UCSRA,UCSRB,UCSRC,
; UBRRH,UBRRL
; Modify Ports : None
;*****
init_232:
push G_ACC1
.if DEFINED UCSR0A
LDI G_ACC1,0
OUT UCSR0A,G_ACC1
LDI
G_ACC1,(1<<RXICIE)|(1<<RXEN)|(1<<TXEN)
OUT UCSR0B,G_ACC1
// U_BAUD_ASYNC_NORMAL
LDI G_ACC1,(1<<UCSZ01)|(1<<UCSZ00)
OUT UCSR0C,G_ACC1
LDI G_ACC1,HIGH(U_UBRR)
OUT UBRR0H,G_ACC1

LDI G_ACC1,Low(U_UBRR)
OUT UBRR0L,G_ACC1
.else
LDI G_ACC1,0
OUT UCSRA,G_ACC1
LDI
G_ACC1,(1<<RXICIE)|(1<<RXEN)|(1<<TXEN)
OUT UCSRB,G_ACC1
// U_BAUD_ASYNC_NORMAL
LDI G_ACC1,(1<<UCSZ1)|(1<<UCSZ0)
OUT UCSRC,G_ACC1
LDI G_ACC1,HIGH(U_UBRR)
OUT UBRRH,G_ACC1
LDI G_ACC1,Low(U_UBRR)
OUT UBRL,G_ACC1
.endif
pop G_ACC1
ret
;*****
; function : KanePalmo1
; Description: one pulse on motor1
; Input :None
; Output :None
; use Registers :G_ACC1,COUNT_S1
;*****
; function : KanePalmo2
; Description: one pulse on motor2
; Input :None
; Output :None
; use Registers :G_ACC1,YH,YL,G_ACC3
; Modify Registers :Count1_Step
; Modify CPU :None
; Modify Ports :MOTOR_PORT
;*****
KanePalmo1:
mac_KANE_PALMO 1
ret
;*****
**
; function : KanePalmo2
; Description: one pulse on motor2
; Input :None
; Output :None
; use Registers :G_ACC1,YH,YL,G_ACC3
; Modify Registers :Count2_Step
; Modify CPU :None
; Modify Ports :MOTOR_PORT
;*****
KanePalmo2:
mac_KANE_PALMO 2
ret
;*****
; function :StopMoter
; Description:Stops the Motor and
; Set break
; On MOTOR_PORT=0B00001000
(if defined DEVICE_HAS_BREAK)
; or Off MOTOR_PORT=0 (if
not defined DEVICE_HAS_BREAK)
; Input :None
; Output :None
; use Registers :FRENO_COUNT,G_ACC1
; Modify Registers
:FRENO_COUNT,Bitfield1,einai_se_freno
; Modify CPU : NONE
; Modify Ports : MOTOR_PORT
;*****
StopMoter1:
#ifdef DEVICE_HAS_BREAK
SBR Bitfield1 ,EXP2
(einai_se_freno)
CLR FRENO1_COUNT
ret
#else
PUSH G_ACC1
IN G_ACC1,MOTOR1_PORT
ANDI G_ACC1,MOTOR_MASK

OUT MOTOR1_PORT,G_ACC1

POP G_ACC1
RET
#endif
StopMoter2:
#ifdef DEVICE_HAS_BREAK
SBR Bitfield2 ,EXP2
(einai_se_freno)
CLR FRENO2_COUNT
ret
#else
PUSH G_ACC1
IN G_ACC1,MOTOR2_PORT
ANDI G_ACC1,MOTOR_MASK
OUT MOTOR2_PORT,G_ACC1
POP G_ACC1
RET
#endif
;*****
; function :StartMoter
; Description:
; Input :NONE
; Output :NONE
; use Registers :G_ACC1,COUNT_S1

```

```

;          Modify          Registers
:Bitfield1.einai_se_freno
; Modify CPU          :NONE
; Modify Ports       :MOTOR_PORT
;*****
StartMoter1:
    PUSH    G_ACC1
    PUSH    G_ACC3
    IN      G_ACC1,MOTOR1_PORT
    ANDI    G_ACC1,MOTOR_MASK
    LDS     G_ACC3,LAST_MOTOR1_VALUE
//the last output in motor port
    OR      G_ACC1,G_ACC3
    OUT     MOTOR1_PORT,G_ACC1
    CBR     Bitfield1      ,EXP2
(einai_se_freno)
    POP     G_ACC3
    POP     G_ACC1
    RET
StartMoter2:
    PUSH    G_ACC1
    PUSH    G_ACC3
    IN      G_ACC1,MOTOR1_PORT
    ANDI    G_ACC1,MOTOR_MASK
    LDS     G_ACC3,LAST_MOTOR2_VALUE
//the last output in motor port
    OR      G_ACC1,G_ACC3
    OUT     MOTOR2_PORT,G_ACC1
    CBR     Bitfield2      ,EXP2
(einai_se_freno)
    POP     G_ACC3
    POP     G_ACC1
    RET
;*****
; function      : KaneReset_SERIAL
; Description:  SELECTS THE MOTOR FROM
;              AND CALLS THE
KaneReset1 OR KaneReset2
; Input        :NONE
; Output       :NONE
; use Registers :G_ACC1,ZH,ZL
; Modify Registers :NODE
; Modify CPU     :NONE
; Modify Ports   :MOTOR_PORT
;*****
KaneReset_SERIAL:
    PUSH G_ACC1
    LDS  G_ACC1,MEM_MOTOTR_VALUE
    TST g_accl
    BREQ IS_MOTOR1
    RCALL KaneReset2
    RJMP EXIT_KANER
IS_MOTOR1:
    RCALL KaneReset1
EXIT_KANER:
    POP G_ACC1
RET
;*****
; function      : KaneReset1
; Description:  Drives the motor1 until
event
;              from a Terminator
; Input        :NONE
; Output       :NONE
; use Registers :G_ACC1,ZH,ZL
; Modify Registers :NODE
; Modify CPU     :NONE
; Modify Ports   :MOTOR_PORT
;*****
KaneReset1:
//          SBIS
MOTOR1_CHK_LEFTPIN,MOTOR1_CHK_LEFTBIT
// rjmp is_in_reset_pl
    rcall StartMoter1
    Moter1_right
    push xh
    push xl
    push zh
    push zl
    ldi zh,0
    sts Steps_Count1_low,zh
    sts Steps_Count1_High,zh
    cbr bitfield1,EXP2(Bit_Error_drive)
#ifdef DEVICE_IS_IN_TEST
    ldi xh,HIGH(2104)
    ldi xl,LOW(2104)
    rjmp KaneReset_end_pl
#endif
    ldi zh,high(4000)
    ldi zl,low(4000)
KaneReset_l_pl:
    SBIS
MOTOR1_CHK_RIGHT_PIN,MOTOR1_CHK_RIGHT_B
IT
    rjmp KaneReset_ea_pl //CHK_LEFT_PIN->
>0
    rcall KanePalmol
    rcall Wait255usec
    rcall Wait255usec
    sbiw zl,1
    breq ExitReset_error_pl
    rjmp KaneReset_l_pl
ExitReset_error_pl:
    jmp ExitReset_errorX_pl
KaneReset_ea_pl:
    push zh
    ldi zh,0
    sts Steps_Count1_low,zh
    sts Steps_Count1_High,zh
    pop zh
    rcall Wait400
    SBIS
MOTOR1_CHK_RIGHT_PIN,MOTOR1_CHK_RIGHT_B
IT
    rjmp KaneReset_e_pl //CHK_LEFT_PIN->
    rjmp KaneReset_l_pl
KaneReset_e_pl:
    clr xh
    clr xl
    ldi zh,high(4000)
    ldi zl,low(4000)
    Moter1_left
KaneReset_r_pl:
    SBIS
MOTOR1_CHK_LEFTPIN,MOTOR1_CHK_LEFTBIT
    rjmp KaneReset_endl_pl
//CHK_RIGHT_PIN->0
    rcall KanePalmol
    rcall Wait255usec
    rcall Wait255usec
    adiw xl,1
    sbiw zl,1
    breq ExitReset_error_pl
    rjmp KaneReset_r_pl
KaneReset_endl_pl:
    rcall Wait400
    SBIS
MOTOR1_CHK_LEFTPIN,MOTOR1_CHK_LEFTBIT
    rjmp KaneReset_end_pl
//CHK_RIGHT_PIN->0
    rjmp KaneReset_r_pl
KaneReset_end_pl:
    mov zl,xl
    mov zh,xh
    sts Max1_Count_high,zh
    sts Max1_Count_low,zl
is_in_reset_pl:
    clr zh
    clr zl
    sts MOTOR1_MEM_EIMAI_high,zl
    sts MOTOR1_MEM_EIMAI_low,zl
    sts Current1_Count_high,zh
    sts Current1_Count_low,zl
    Moter1_right

```

```

    push g_acc1
    ldi g_acc1,0
kai_allo1:
    SBIC
MOTOR1_CHK_LEFTPIN,MOTOR1_CHK_LEFTBIT
    rjmp kai_allo2
    __WAIT_MILLISECONDS 1
    rcall Wait255usec
    rcall Wait255usec
    rcall KanePalmo1
// __WAIT_MILLISECONDS 30
    inc g_acc1
    cpi g_acc1,95
    brne kai_allo1
kai_allo2:
    sts Current1_Count_low,g_acc1
    SBIS
MOTOR1_CHK_LEFTPIN,MOTOR1_CHK_LEFTBIT
    Sbr bitfield1,EXP2(Bit_Error_drive)
    rcall Apantsh1
    pop g_acc1
    Moter1_left
ExitReset_p1:
    rcall StopMoter1
    pop z1
    pop zh
    pop xl
    pop xh
ret
ExitReset_errorX_p1:
    sbr bitfield1,EXP2(Bit_Error_drive)
    rcall Apantsh1
rjmp ExitReset_p1
;*****
; function      : KaneReset2
; Description:  Drives the motor2 until
event
;
;           from a Terminator
; Input       :NONE
; Output      :NONE
; use Registers :G_ACC1,ZH,ZL
; Modify Registers :NODE
; Modify CPU   :NONE
; Modify Ports :MOTOR_PORT
;*****
KaneReset2:
function_Motor_Reset2:
    rcall StartMoter2
    Moter2_right
    push xh
    push xl
    push zh
    push zl
    ldi zh,0
    sts Steps_Count2_low,zh
    sts Steps_Count2_High,zh
    cbr bitfield2,EXP2(Bit_Error_drive)
#ifdef DEVICE_IS_IN_TEST
    ldi xh,HIGH(2104)
    ldi xl,LOW(2104)
    rjmp KaneReset_end_p2
#endif
    ldi zh,high(4000)
    ldi zl,low(4000)
KaneReset_l_p2:
    SBIS
MOTOR2_CHK_RIGHT_PIN,MOTOR2_CHK_RIGHT_B
IT
    rjmp KaneReset_ea_p2 //CHK_LEFT_PIN->0
    rcall KanePalmo2
    rcall Wait255usec
    rcall Wait255usec
    sbiw zl,1
    breq ExitReset_error_p2
    rjmp KaneReset_l_p2
ExitReset_error_p2:
    jmp ExitReset_errorX_p2
KaneReset_ea_p2:
    push zh
    ldi zh,0
    sts Steps_Count2_low,zh
    sts Steps_Count2_High,zh
    pop zh
    rcall Wait400
    SBIS
MOTOR2_CHK_RIGHT_PIN,MOTOR2_CHK_RIGHT_B
IT
    rjmp KaneReset_e_p2 //CHK_LEFT_PIN->0
    rjmp KaneReset_l_p2
KaneReset_e_p2:
    clr xh
    clr xl
    ldi zh,high(4000)
    ldi zl,low(4000)
    Moter2_left
KaneReset_r_p2:
    SBIS
MOTOR2_CHK_LEFTPIN,MOTOR2_CHK_LEFTBIT
    rjmp KaneReset_end1_p2 //CHK_RIGHT_PIN->0
    rcall KanePalmo2
    rcall Wait255usec
    rcall Wait255usec
    adiw xl,1
    sbiw zl,1
    breq ExitReset_error_p2
    rjmp KaneReset_r_p2
KaneReset_end1_p2:
    rcall Wait400
    SBIS
MOTOR2_CHK_LEFTPIN,MOTOR2_CHK_LEFTBIT
    rjmp KaneReset_end_p2 //CHK_RIGHT_PIN->0
    rjmp KaneReset_r_p2
KaneReset_end_p2:
    mov z1,xl
    mov zh,xh
    sts Max2_Count_high,zh
    sts Max2_Count_low,zl
    clr zh
    clr zl
    sts MOTOR2_MEM_EIMAI_high,zl
    sts MOTOR2_MEM_EIMAI_low,zl
    sts Current2_Count_high,zh
    sts Current2_Count_low,zl
    Moter2_left
    rcall KanePalmo2
    rcall Apantsh1
ExitReset_p2:
    rcall StopMoter2
    pop z1
    pop zh
    pop xl
    pop xh
ret
ExitReset_errorX_p2:
    sbr bitfield2,EXP2(Bit_Error_drive)
    rcall Apantsh1
rjmp ExitReset_p2
start_timer:
    PUSH G_ACC1
    LDS G_ACC1,MEM_MOTOTR_VALUE
    TST g_acc1
    BREQ stt_IS_MOTOR1
    SBR BITFIELD2,EXP2(Bit_drive_mot2)
    RJMP stt_EXIT
stt_IS_MOTOR1:
    SBR BITFIELD2,EXP2(Bit_drive_mot1)
stt_EXIT:
    CLR G_ACC1
    out TCNT1L,g_Acc1
    mov G_ACC1,SPEED_TIMERH
    out TCNT1H,g_Acc1

```

```

    in G_ACC1,TIMSK
    ORI G_ACC1 ,(1<<TOIE1)
    out TIMSK,G_ACC1
    POP G_ACC1
ret
stop_timer1:
    push G_ACC1
    in G_ACC1,TIMSK
    ANDI G_ACC1 ,0xff^(1<<TOIE1)
    out TIMSK,G_ACC1
    POP G_ACC1
ret
inOVFlADDR:
INTERRUPT_PROLOG
    SBRc BITFIELD2,Bit_drive_mot2
    RJMP function_DRIVE_MOTOR2
function_DRIVE_MOTOR1:
    dLed1_Change
    push zh
    push zl
    rcall KanePalmo1
    SBIC
MOTOR1_CHK_LEFTPIN,MOTOR1_CHK_LEFTBIT
    rjmp Left_is_ok_p1 //CHK_LEFT_PIN->5
    RJMP EXIT_cont_go_error_p1
Left_is_ok_p1:
    SBIC
MOTOR1_CHK_RIGHT_PIN,MOTOR1_CHK_RIGHT_B
IT
    rjmp Right_is_ok_p1 //CHK_LEFT_PIN->5
    RJMP EXIT_cont_go_error_p1
Right_is_ok_p1:
    lds zh,Count1_to_go_high
    lds zl,Count1_to_go_low
    sbiw zl,1
    brne cont_go_p1
    rcall stop_timer1
    rcall StopMoter1
    SBR BITFIELD1,EXP2(bit_phga)
    lds i_acc1,tmp_Current1_high
    sts Current1_Count_high,i_acc1
    lds i_acc1,tmp_Current1_low
    sts Current1_Count_low,i_acc1
cont_go_p1:
    sts Count1_to_go_high ,zh
    sts Count1_to_go_low,zl
EXIT_cont_go_p1:
    pop zl
    pop zh
inOVFlADDR_exit_p1:
    CLR G_ACC1
    out TCNT1L,g_Acc1
    mov G_ACC1,SPEED_TIMERH
    out TCNT1H,g_Acc1
INTERRUPT_EPILOG
RETI
EXIT_cont_go_error_p1:
    rcall stop_timer1
    rcall StopMoter1
    SBR BITFIELD1,EXP2(bit_phga)
    SBR BITFIELD1,EXP2(Bit_Error_drive)
    rjmp EXIT_cont_go_p1
function_DRIVE_MOTOR2:
    dLed1_Change
    push zh
    push zl
    SBIC
MOTOR2_CHK_LEFTPIN,MOTOR2_CHK_LEFTBIT
    rjmp Left_is_ok_p2 //CHK_LEFT_PIN->5
    RJMP EXIT_cont_go_error_p2
Left_is_ok_p2:
    SBIC
MOTOR2_CHK_RIGHT_PIN,MOTOR2_CHK_RIGHT_B
IT
    rjmp Right_is_ok_p2 //CHK_LEFT_PIN->5
    RJMP EXIT_cont_go_error_p2
Right_is_ok_p2:
    rcall KanePalmo2
    lds zh,Count2_to_go_high
    lds zl,Count2_to_go_low
    sbiw zl,1
    brne cont_go_p2
    rcall stop_timer1
    rcall StopMoter2
    SBR BITFIELD2,EXP2(bit_phga)
    lds i_acc1,tmp_Current2_high
    sts Current2_Count_high,i_acc1
    lds i_acc1,tmp_Current2_low
    sts Current2_Count_low,i_acc1
cont_go_p2:
    sts Count2_to_go_high ,zh
    sts Count2_to_go_low,zl
EXIT_cont_go_p2:
    pop zl
    pop zh
inOVFlADDR_exit_p2:
    CLR G_ACC1
    out TCNT1L,g_Acc1
    mov G_ACC1,SPEED_TIMERH
    out TCNT1H,g_Acc1
INTERRUPT_EPILOG
RETI
EXIT_cont_go_error_p2:
    rcall stop_timer1
    rcall StopMoter2
    SBR BITFIELD2,EXP2(bit_phga)
    SBR BITFIELD2,EXP2(Bit_Error_drive)
    rjmp EXIT_cont_go_p2
inOVf0ADDR:
INTERRUPT_PROLOG
INTERRUPT_EPILOG
RETI
inURXCADDR:
    IN I_ACC1,UDR
Uart_RxcA:
#ifdef RS232_PROT
    CPI I_ACC1,0X02
    BREQ Start_Receive
    SBRS BITFIELD1,bit_in_serial
    RJMP Exit_Receive
    CPI I_ACC1,0X03
    BREQ Stop_Receive
#else
    CPI I_ACC1,'Q'
    BREQ Exit_Receive
    CPI I_ACC1,10
    BREQ Stop_Receive
    CPI I_ACC1,13
    BREQ Stop_Receive
#endif
    CPI I_ACC1,'d' ;0X64
    BREQ Posible_Reset
Continue:
    LDI YL,Low(MEM_SERIAL_IN)
    LDI YH,High(MEM_SERIAL_IN)
    ADD YL,PLHUOS_SER_DATA
    ST Y+,I_ACC1
    INC PLHUOS_SER_DATA
    LDI I_ACC1,0X00
    ST Y+,I_ACC1
Exit_Receive:
    RETI
Posible_Reset:
    PUSH I_ACC1
    MOV I_ACC1,PLHUOS_SER_DATA
    CPI I_ACC1,0X02
    POP I_ACC1
    BRNE Continue
    RJMP Make_Reset
Start_Receive:
    CLR PLHUOS_SER_DATA
    SBR Bitfield1 ,EXP2
(bit_In_Serial)

```

```

        CBR          Bitfield1          ,EXP2          OUT   MCUCSR,ZL
(bit_From_Serial)
        RETI
        Stop_Receive:
#ifdef RS232_PROT
        CBR          Bitfield1          ,EXP2
(bit_In_Serial)
        SBR          Bitfield1          ,EXP2
(bit_From_Serial)
#else
        tst   PLHUOS_SER_DATA
        breq  Stop_Receive1
        LDI   YL,Low(MEM_SERIAL_IN)
        LDI   YH,High(MEM_SERIAL_IN)
        ADD   YL,PLHUOS_SER_DATA
                LDI   I_ACC1,0
        ST    Y+,I_ACC1
        CBR          Bitfield1          ,EXP2
(bit_In_Serial)
        SBR          Bitfield1          ,EXP2
(bit_From_Serial)
        Stop_Receive1:
#endif
        clr   PLHUOS_SER_DATA
        RETI
        Make_Reset:
        LDI   G_ACC1,0X08
        OUT   WDTCSR,G_ACC1
        Wait_Reset:
        RJMP  Wait_Reset
inReset1:
        ldi  g_accl,v_TCNT1H
        mov  SPEED_TIMERH,G_ACC1
        LDI   G_ACC1,'~';
        sts  LAST_COMMAND,G_ACC1
        rcall init_232
        rcall init_HW
        RJMP _main_A
        sbi  ddra,5
        sbi  porta,5
        sbi  ddra,6
        cbi  porta,6
        IN   ZL,MCUCSR
        SBRS ZL,WDRF
        RJMP _main_A
        rcall init_232
        ldi  g_accl,2
        rcall send_char
        ldi  g_accl,'^'
        rcall send_char
        ldi  g_accl,'^'
        rcall send_char
        ldi  g_accl,3
        rcall send_char
        sei
        rcall Wait1millisec
        LDI  G_ACC1,'b'
        rcall Send_Version
        clt
        ldi  g_accl,'p'
        rcall wait_char
        brts _main_a
        ldi  g_accl,'e'
        rcall wait_char
        brts _main_a
        cli

        ldi  g_accl,'B'
        rcall send_char
        jmp  LARGEBOOTSTART
_main_A:
        cli
        LDI  G_ACC1,'~';
        sts  LAST_COMMAND,G_ACC1
        clt
        IN   ZL,MCUCSR
        ANDI ZL,LOW(0xE0)
        OUT   MCUCSR,ZL
        LDI  G_ACC1,v_tccr1b
        out  TCCR1B,G_ACC1
_main:
        CBR          Bitfield1          ,EXP2
(einai_se_freno)
        CBR          Bitfield2          ,EXP2
(einai_se_freno)
        NOP
        MYBYTE1...MYBYTE4
        INITMOTORMEMORY 1
        INITMOTORMEMORY 2
        CLR   G_ACC3
        LDI   G_ACC1,0X19
        Point33:
        RCALL Wait255usec
        DEC   G_ACC1
        BRNE  Point33
        IN    G_ACC1,MOTOR1_PORT
        ANDI  G_ACC1,MOTOR_MASK
        ORI   G_ACC1,0X00
        OUT   MOTOR1_PORT,G_ACC1
        IN    G_ACC1,MOTOR2_PORT
        ANDI  G_ACC1,MOTOR_MASK
        ORI   G_ACC1,0X00
        OUT   MOTOR2_PORT,G_ACC1
        CLR   BITFIELD1
        CLR   BITFIELD1
        LDI  G_ACC1,0
        out  TIMSK,G_ACC1 //No timer enabled
        // __WAIT_SECONDS 31
        LDI  G_ACC1,'~';
        sts  LAST_COMMAND,G_ACC1
        sei
        rcall test_functions
        pantal:
        Panta:
        SBRC  BITFIELD1,bit_from_Serial
        RCALL Hrue_Serial
        SBRC  BITFIELD1,bit_phga
        RCALL send_phga
        SBRC  BITFIELD2,bit_phga
        RCALL send_phga
#ifdef DEVICE_HAS_BREAK
        SBRC  BITFIELD1,einai_se_freno
        RCALL ToogleFreno1
        SBRC  BITFIELD2,einai_se_freno
        RCALL ToogleFreno2
#endif
        RJMP  Panta
        RET
        ToogleFreno1:
        dec  FREN01_COUNT
        brne ToogleFrenola
        CBR
        BITFIELD1,EXP2(einai_se_freno)
        PUSH G_ACC1
        IN    G_ACC1,MOTOR1_PORT
        ANDI  G_ACC1,MOTOR_MASK
        OUT   MOTOR1_PORT,G_ACC1
        POP   G_ACC1
        ToogleFrenola:
        RET
        ret
        ToogleFreno2:
        ret
        send_phga:
        CBR  BITFIELD1,exp2(bit_phga)
        CBR  BITFIELD2,exp2(bit_phga)
        rcall Apanthsh1
        ret
        Steile_Wait1:
        .if  DEFINED UCSR0A
                SBIS UCSR0A,5
        .else
                SBIS UCSRA,5
        .endif

```

```

        RJMP    Steile_Wait1
        RET
;*****
; function :store_hex
; Description:Set G_ACC1 as HEX to XLXH
; Input :G_ACC1
; Output :XH,XL
; use Registers :G_ACC1,XH,XL
; Modify Registers :XH,XL
; Modify CPU :NONE
; Modify Ports :NONE
;*****
store_hex:
    PUSH    G_ACC1
    PUSH    G_ACC1
    ANDI    G_ACC1,0b11110000
    SWAP    G_ACC1
    CPI     G_ACC1,0X0A
    BRCS    store_hex_1
    SUBI    G_ACC1,0XF9
store_hex_1:
    SUBI    G_ACC1,0XD0
    ST      X+,G_ACC1
    POP     G_ACC1
    ANDI    G_ACC1,0X0F
    CPI     G_ACC1,0X0A
    BRCS    store_hex_2
    SUBI    G_ACC1,0XF9
store_hex_2:
    SUBI    G_ACC1,0XD0
    ST      X+,G_ACC1
    POP     G_ACC1
    RET
Hrue_Serial:
    push    g_accl
    push    xl
    push    xh
    CBR     Bitfield1 ,EXP2
(bit_From_Serial)
    LDI     XL,low(MEM_SERIAL_IN)
    LDI     XH,high(MEM_SERIAL_IN)
#ifdef RS232_PROT
    LD      G_ACC1,X+
    LD      G_ACC1,X+
#endif
    LD      G_ACC1,X+
    sts    LAST_COMMAND,G_ACC1
    CPI     G_ACC1,'?'
    BRNE    Label264b
    RCALL   Wait255msec
    LDI     G_ACC1,'a'
    RCALL   Send_Version
    RJMP    ExitComeSerial
Label264b:
    CPI     G_ACC1,'@'
    BRNE    Label264b1
    RCALL   Wait255msec
    LDI     G_ACC1,'a'
    RCALL   Send_info
    RJMP    ExitComeSerial
Label264b1:
    CPI     G_ACC1,'8'
    BRNE    Label20b
    RCALL   Wait255msec
    RCALL   Apanthsh1
    RJMP    ExitComeSerial
Label20b:
    CPI     G_ACC1,'5'
    BRNE    Label218
    LD      G_ACC1,X+
    SUBI    G_ACC1,'1'
    STS    MEM_MOTOTR_VALUE,G_ACC1
    rcall   read_hex2
    rcall   calc_count_to_go
    brts    Label20be
    rcall   start_timer
    RJMP    ExitComeSerial
Label20be:
    RCALL   Wait255msec
    RCALL   Apanthsh1
    RJMP    ExitComeSerial
Label218p:
    CPI     G_ACC1,'g'
    BRNE    Label218
    rcall   read_hex2
    lds    g_accl,MEM_HEX_VALUE_high
    sts    Count1_to_go_high,g_accl
    lds    g_accl,MEM_HEX_VALUE_low
    sts    Count1_to_go_low,g_accl
    rcall   read_hex2
    lds    g_accl,MEM_HEX_VALUE_high
    sts    tmp_Current1_high,g_accl
    lds    g_accl,MEM_HEX_VALUE_low
    sts    tmp_Current1_low,g_accl
    rcall   start_timer
    RJMP    ExitComeSerial
Label218:
    CPI     G_ACC1,'1'
    BRNE    Label21f
    LDi     G_ACC1,0
    STS    MEM_MOTOTR_VALUE,G_ACC1
    RCALL   Goto_Next
    RJMP    ExitComeSerial
Label21f:
    CPI     G_ACC1,'3'
    BRNE    Label22d
    LD      G_ACC1,X+
    SUBI    G_ACC1,'1'
    STS    MEM_MOTOTR_VALUE,G_ACC1
    RCALL   KaneReset_SERIAL
    RJMP    ExitComeSerial
Label22d:
    CPI     G_ACC1,'4'
    BRNE    Label22da
    LDi     G_ACC1,0
    STS    MEM_MOTOTR_VALUE,G_ACC1
    RCALL   Goto_First
    RJMP    ExitComeSerial
Label22da:
    CPI     G_ACC1,'2'
    BRNE    Label23ex
    LDi     G_ACC1,0
    STS    MEM_MOTOTR_VALUE,G_ACC1
    RCALL   Goto_Prev
    RJMP    ExitComeSerial
Label23ex:
    CPI     G_ACC1,'6'
    BRNE    Label23e
    LDi     G_ACC1,0
    STS    MEM_MOTOTR_VALUE,G_ACC1
    rcall   read_hex2
    RCALL   Goto_Filter
    RJMP    ExitComeSerial
Label23e:
    CPI     G_ACC1,'a'
    BRNE    Label243
    rcall   read_hex
    lds    g_accl,MEM_HEX_VALUE_Low
    mov    SPEED_TIMERH,g_accl
    RJMP    ExitComeSerial
Label243:
    CPI     G_ACC1,'b'
    BRNE    Label243a
    rcall   read_hex
    lds    g_accl,MEM_HEX_VALUE_low
    out    TCCR1B,G_ACC1
    RJMP    ExitComeSerial
Label243a:
    CPI     G_ACC1,'n'
    BRNE    Label244a
    LD      G_ACC1,X+
    cpi    g_accl,'l'

```

```

        breq Label243b
moter1_right
        rjmp Label243c
Label243b:
moter1_left
Label243c:
        RJMP    ExitComeSerial
Label244a:
        CPI     G_ACC1,'m'
        BRNE   Label245a
        rcall  read_hex
Label244b:
        rcall  Wait255usec
        rcall  Wait255usec
        rcall  KanePalmol
        dec   g_acc1
        brne  Label244b
        RJMP  ExitComeSerial
Label245a:
        CPI     G_ACC1,'o'
        BRNE   Label246a
        rcall  StartMoter1
        RJMP  ExitComeSerial
Label246a:
        CPI     G_ACC1,'p'
        BRNE   Label247a
        rcall  StopMoter1
        RJMP  ExitComeSerial
Label247a:
        CPI     G_ACC1,'*'
        BRNE   Label264e
        pop   xh
        pop   xl
        pop   g_acc1
        cli
        jmp   LARGEBOOTSTART
Label264e:
        RCALL  Wait255msec
        rcall  unknown_com
ExitComeSerial:
        POP   XH
        POP   XL
        POP   G_ACC1
        RET
unknown_com:
        push  g_acc1
        push  xl
        push  xh
        push  g_acc1
        RCALL Set_Serial_Out
        LDI   G_ACC1,'!'
        ST    X+,G_ACC1
        pop   g_acc1
        ST    X+,G_ACC1
        rcall Serial_out_end
        ST    X+,G_ACC1
        RJMP  Steile_Data
Goto_Next:
        lds   xh,MOTOR1_MEM_EIMAI_high
        lds   xl,MOTOR1_MEM_EIMAI_low
        adiw  xl,1
        rjmp  Goto_filterA
        ret
Goto_Prev:
        lds   xh,MOTOR1_MEM_EIMAI_high
        lds   xl,MOTOR1_MEM_EIMAI_low
        sbiw  xl,1
        breq  Label20xe
        rjmp  Goto_filterA
        ret
Label20xe1:
        pop   xl
        pop   xh
Label20xe:
        SBR  BITFIELD1,EXP2(bit_phga)
        ret
Goto_Filter:
        lds   xh,MEM_HEX_VALUE_High
        lds   xl,MEM_HEX_VALUE_Low
        rjmp  Goto_filterA
        ret
Goto_First:
        ldi   xh,0
        ldi   xl,0
        rjmp  Goto_filterA
        ret
Goto_filterA:
        push  xh
        push  xl
        rcall read_postion_count
        rcall calc_count_to_go
        brts  Label20xe1
        pop   xl
        pop   xh
        sts   MOTOR1_MEM_EIMAI_high,xh
        sts   MOTOR1_MEM_EIMAI_low,xl
        rcall start_timer
        ret
        ret
Send_info:
        push  g_acc1
        push  xl
        push  xh
        RCALL Set_Serial_Out
        LDI   G_ACC1,'I'
        ST    X+,G_ACC1
        LDI   G_ACC1,'n'
        ST    X+,G_ACC1
        LDI   G_ACC1,'f'
        ST    X+,G_ACC1
        LDS   G_ACC1,Steps_Count1_High
        rcall store_hex
        LDS   G_ACC1,Steps_Count1_Low
        rcall store_hex
        LDS   G_ACC1,Max1_Count_high
        rcall store_hex
        LDS   G_ACC1,Max1_Count_low
        rcall store_hex
        LDS   G_ACC1,Steps_Count2_High
        rcall store_hex
        LDS   G_ACC1,Steps_Count2_Low
        rcall store_hex
        LDS   G_ACC1,Max2_Count_high
        rcall store_hex
        LDS   G_ACC1,Max2_Count_low
        rcall store_hex
        mov   G_ACC1,SPEED_TIMERH
        rcall store_hex
        rcall Serial_out_end
        RJMP  Steile_Data
        ret
Send_Version:
        push  g_acc1
        push  xl
        push  xh
        push  g_acc1
        RCALL Set_Serial_Out
        LDI   G_ACC1,'V'
        ST    X+,G_ACC1
        LDI   G_ACC1,'E'
        ST    X+,G_ACC1
        pop   g_acc1
        ST    X+,G_ACC1
        LDI   G_ACC1,VERSION_M1
        ST    X+,G_ACC1
        LDI   G_ACC1,VERSION_M2
        ST    X+,G_ACC1
        LDI   G_ACC1,'.'
        ST    X+,G_ACC1
        LDI   G_ACC1,VERSION_M3
        ST    X+,G_ACC1
        LDI   G_ACC1,VERSION_M4
        ST    X+,G_ACC1
        rcall Serial_out_end

```

```

        RJMP    Steile_Data
        RET
Apanthsh1:
    push g_acc1
    push xl
    push xh
    RCALL    Set_Serial_Out
    LDI     G_ACC1,'g'    ;0X67
    ST      X+,G_ACC1
    RJMP    Steile_Eimai
Set_Serial_Out:
    LDI     XL,low(MEM_SERIAL_OUT)
    LDI     XH,high(MEM_SERIAL_OUT)
#ifdef RS232_PROT
    LDI     G_ACC1,0X02
    ST      X+,G_ACC1
    LDI     G_ACC1,0X2F
    ST      X+,G_ACC1
    LDS     G_ACC1,LAST_COMMAND
    ST      X+,G_ACC1
#endif
    LDI     G_ACC1,'~';
    sts    LAST_COMMAND,G_ACC1
    RET
Serial_out_end:
#ifdef RS232_PROT
    LDI     G_ACC1,0X03
#else
    LDI     G_ACC1,10
    ST      X+,G_ACC1
    LDI     G_ACC1,13
    ST      X+,G_ACC1
    LDI     G_ACC1,0X03
#endif
    ST      X+,G_ACC1
ret
Steile_Eimai:
    LDI     G_ACC1,'t'
    ST      X+,G_ACC1
    LDI     G_ACC1,'0'
    sbrc    BITFIELD1,Bit_Error_drive
    sbr     G_ACC1,exp2(0)
    sbrc    BITFIELD2,Bit_Error_drive
    sbr     G_ACC1,exp2(1)
    ST      X+,G_ACC1
    LDS     G_ACC1,Current1_Count_High
    rcall   store_hex
    LDS     G_ACC1,Current1_Count_Low
    rcall   store_hex
    LDS     G_ACC1,Current2_Count_High
    rcall   store_hex
    LDS     G_ACC1,Current2_Count_Low
    rcall   store_hex
    LDS
G_ACC1,MOTOR1_MEM_EIMAI_High
    rcall   store_hex
    LDS     G_ACC1,MOTOR1_MEM_EIMAI_Low
    rcall   store_hex
rcall Serial_out_end
Steile_Data:
    LDI     XL,low(MEM_SERIAL_OUT)
    LDI     XH,high(MEM_SERIAL_OUT)
Steile_Pali:
    .if    DEFINED UCSR0A
        SBIS UCSR0A,5
    .else
        SBIS UCSRA,5
    .endif
    RJMP    Steile_Pali
    LD      G_ACC1,X+
#ifdef RS232_PROT
#else
    CPI     G_ACC1,0X03
    BREQ    End_Steile_Pali
#endif
    OUT    UDR,G_ACC1
    rcall   Wait1millisec
        CPI     G_ACC1,0X03
        BRNE    Steile_Pali
End_Steile_Pali:
    pop    xh
    pop    xl
    pop    g_acc1
    RET
send_char:
    .if    DEFINED UCSR0A
        SBIS UCSR0A,5
    .else
        SBIS UCSRA,5
    .endif
    RJMP    send_char
    OUT    UDR,G_ACC1
send_char1:
    .if    DEFINED UCSR0A
        SBIS UCSR0A,5
    .else
        SBIS UCSRA,5
    .endif
    RJMP    send_char1
ret
wait_char:
    push g_acc2
    ldi g_acc2,150
wait_char_pali:
    rcall   Wait1millisec
    SBRC    BITFIELD1,bit_from_Serial
    Rjmp    _has_data_Serial
    dec g_acc2
    brne wait_char_pali
    set
    rjmp   exit_wait_char
_has_data_Serial:
    lds g_acc2,MEM_SERIAL_IN
    cp g_acc2,g_acc1
    breq   exit_wait_char
    set
exit_wait_char:
    pop g_acc2
ret
/*****
function EEPROM_read_word
read a word from EEPROM
input  xh,xl->Epprom Address
output ZH ZL data of eeprom
modified registers ZL ZH
*****/
EEPROM_read_word:
    ADIW xl,1
    RCALL EEPROM_Read_byte
    MOV  ZH,ZL
    SBIW xl,1
/*****
function EEPROM_read_Byte
read a byte from EEPROM
input  xh,xl->Epprom Address
output ZL data of eeprom
modified registers ZL
*****/
EEPROM_Read_byte:
    SBIC  EECR,EWE
    RJMP  EEPROM_Read_byte
    PUSH ZH
    IN   ZH,SREG
    CLI
    .if  DEFINED EEARH
        OUT  EEARH,xh
    .endif
    OUT  EEARL,xl
    SBI  EECR,EERE
    IN   ZL,EEDR
    OUT  SREG,ZH
    POP  ZH
    sei
    nop

```

```

        RET
/*****
function EEPROM_write_word
writes a word to EEPROM
input  xh,xl->Eeprom Address
input  ZH ZL data of eeprom
modified registers ZL ZH
*****/
EEPROM_write_Word:
        RCALL EEPROM_write_Byte
        ADIW xl,1
        PUSH ZL
        MOV  ZL,ZH
        RCALL EEPROM_write_Byte
        POP  ZL
        SBIW xl,1
        RET
/*****
function EEPROM_write_Byte
writes a byte to EEPROM
input  xh,xl->Eeprom Address
input  ZL data of eeprom
modified registers ZL
*****/
EEPROM_write_Byte:
        SBIC EECR,EWE
        RJMP EEPROM_write_Byte
        IN   R25,SREG
        CLI
.if DEFINED EEARH
        OUT  EEARH,xh
.endif
        OUT  EEARL,xl
        SBI  EECR,EERE
        IN   R24,EEDR
        CP   ZL,R24
        BREQ __EEPROMWRB0
        OUT  EEDR,ZL
        SBI  EECR,EEMWE
        SBI  EECR,EWE
__EEPROMWRB0:
        OUT  SREG,R25
        sei
        nop
        RET
conv_hex:
        subi G_ACC1,0x30
        subi G_ACC2,0x30
        cpi  G_ACC1,0XA
        brlo con_hex1
        subi G_ACC1,7
con_hex1:
        cpi  G_ACC2,0XA
        brlo con_hex2
        subi G_ACC2,7
con_hex2:
        swap g_acc1
        add  g_acc1,g_acc2
ret
read_hex:
        push g_acc2
        LD   G_ACC1,X+
        LD   G_ACC2,X+
        rcall conv_hex
        sts  MEM_HEX_VALUE_low,g_acc1
pop  g_acc2
ret
read_hex2:
        push g_acc2
        LD   G_ACC1,X+
        LD   G_ACC2,X+
        rcall conv_hex
        sts  MEM_HEX_VALUE_High,g_acc1
        LD   G_ACC1,X+
        LD   G_ACC2,X+
        rcall conv_hex
        sts  MEM_HEX_VALUE_low,g_acc1

pop  g_acc2
ret
/*****
in xl:xh the wavelength-300
out xh:xl the counts for this
and MEM_HEX_VALUE (high low) the
counts
*****/
read_postion_count:
        push zh
        push zl
        push g_acc1
        ldi  zl,low(flash_positions*2)
        ldi  zh,high(flash_positions*2)
        lsl  xl
        Ror  xh
        add  zl,xl
        adc  zh,xh
        lpm  g_acc1,z+
        mov  xl,g_acc1
        lpm  g_acc1,z
        mov  xh,g_acc1
        pop  g_acc1
        pop  zl
        pop  zh
        sts  MEM_HEX_VALUE_High,xh
        sts  MEM_HEX_VALUE_low,xl
ret
calc_count_to_go:
        clt
        PUSH G_ACC1
        LDS  G_ACC1,MEM_MOTOTR_VALUE
        TST  g_acc1
        BREQ ctg_IS_MOTOR1
        RCALL calc_count_to_go2
        RJMP ctg_EXIT
ctg_IS_MOTOR1:
        RCALL calc_count_to_go1
ctg_EXIT:
        POP  G_ACC1
RET
calc_count_to_go1:
        sbrs BITFIELD1,Bit_Error_drive
        rjmp calc_count_to_go_OK_pl
        set
        rjmp exit_error_calc_pl
calc_count_to_go_OK_pl:
        push xl
        push xh
        lds  xH,MEM_HEX_VALUE_high
        lds  xL,MEM_HEX_VALUE_low
        push zh
        push zl
        lds  zl,Current1_Count_low
        lds  zh,Current1_Count_high
        sts  tmp_Current1_high,xh
        sts  tmp_Current1_low,xl
        sub  xl,zl
        sbc  xh,zh
        brcc _no_neg_pl
        tst  xl
        brne next_a1
        neg  xh
        rjmp next_aa9
next_a1:
        neg  xl
        com  xh
next_aa9:
        push xl
        push xh
        moter1_left
        rjmp exit_calc_pl
_no_neg_pl:
        push xl
        push xh
        moter1_right
        exit_calc_pl:

```

```

    pop xh
    pop xl
    adiw xl,1
    sbiw xl,1
    brne is_ok1
    set
is_ok1:
    sts Count1_to_go_high,xh
    sts Count1_to_go_low,xl
    pop zl
    pop zh
    pop xh
    pop xl
#ifdef DEVICE_IS_IN_TEST
#endif
exit_error_calc_p1:
    nop
    RET
calc_count_to_go2:
    sbrs BITFIELD2,Bit_Error_drive
    rjmp calc_count_to_go_OK_p2
    set
    rjmp exit_error_calc_p2
calc_count_to_go_OK_p2:
    push xl
    push xh
    lds xH,MEM_HEX_VALUE_high
    lds xL,MEM_HEX_VALUE_low
    push zh
    push zl
    lds zl,Current2_Count_low
    lds zh,Current2_Count_high
    sts tmp_Current2_high,xh
    sts tmp_Current2_low,xl
    sub xl,zl
    sbc xh,zh
    brcc _no_neg_p2
    neg xl
    com xh
    moter2_right
    rjmp exit_calc_p2
_no_neg_p2:
    moter2_left
exit_calc_p2:
    sts Count2_to_go_high,xh
    sts Count2_to_go_low,xl
    pop zl
    pop zh
    pop xh
    pop xl
#ifdef DEVICE_IS_IN_TEST
    rcall SendInfoToGo
#endif
exit_error_calc_p2:
    nop
    RET
test_functions:
    ret
    CBR BITFIELD1,EXP2(Bit_Error_drive)
    CBR BITFIELD2,EXP2(Bit_Error_drive)
    ldi xh,2
    ldi xl,0
    ldi zh,0
    ldi zl,0x10
    sts MEM_HEX_VALUE_high,xh
    sts MEM_HEX_VALUE_low,xl
    //rcall send_hex_hh_xl
    sts Current1_Count_low,zl
    sts Current1_Count_high,zh
    rcall calc_count_to_go1
    rcall start_timer
    ret
ret
Label20Ze:
RJMP Label20Be
SendInfoToGo:
    push g_accl
    push xl
    push xh
    RCALL Set_Serial_Out
    LDI G_ACC1,'c'
    ST X+,G_ACC1
    clr g_ACC1
    SBRs Count1_Step,BIT_DIRECTION1
    rjmp SendInfoToGo1
    ori g_accl,1
SendInfoToGo1:
    SBRs Count2_Step,BIT_DIRECTION2
    rjmp SendInfoToGo2
    ori g_accl,2
SendInfoToGo2:
    rcall store_hex
    LDS G_ACC1,Count1_to_go_high
    rcall store_hex
    LDS G_ACC1,Count1_to_go_low
    rcall store_hex
    LDS G_ACC1,Count2_to_go_high
    rcall store_hex
    LDS G_ACC1,Count2_to_go_high
    rcall store_hex
    LDS G_ACC1,tmp_Current1_high
    rcall store_hex
    LDS G_ACC1,tmp_Current1_low
    rcall store_hex
    LDS G_ACC1,tmp_Current2_high
    rcall store_hex
    LDS G_ACC1,tmp_Current2_high
    rcall store_hex
    rcall Serial_out_end
    RJMP Steile_Data
    ldi g_accl,0xa
    rcall send_char
    pop g_accl
ret
.org LARGEBOOTSTART-128*8
//128*8=1024 words so flash_Positions
starts on a new
// Flash Page this is important for
bootloader to fill
//only the flash_Positions
// 1024 words in flash (2048 bytes)
// 700 nm *2 bytes each 1400 bytes
flash_Positions:
.db
0x0a,0x00,0x0e,0x00,0x12,0x00,0x16,0x00
,0x1a,0x00,0x1e,0x00,0x22,0x00,0x26,0x00
0,0x2a,0x00,0x2e,0x00,0x32,0x00,0x36,0x00
0,0x3a,0x00,0x3e,0x00,0x42,0x00,0x46,0x00
0,0x4a,0x00,0x4e,0x00,0x52,0x00,0x56,0x00
0,0x5a,0x00 ; Data 0 - 20
.db
0x5e,0x00,0x62,0x00,0x66,0x00,0x6a,0x00
,0x6e,0x00,0x72,0x00,0x76,0x00,0x7a,0x00
0,0x7e,0x00,0x82,0x00,0x86,0x00,0x8a,0x00
0,0x8e,0x00,0x92,0x00,0x96,0x00,0x9a,0x00
0,0x9e,0x00,0xa2,0x00,0xa6,0x00,0xaa,0x00
0,0xae,0x00 ; Data 21 - 41
.db
0xb2,0x00,0xb6,0x00,0xba,0x00,0xbe,0x00
,0xc2,0x00,0xc6,0x00,0xca,0x00,0xce,0x00
0,0xd2,0x00,0xd6,0x00,0xda,0x00,0xde,0x00
0,0xe2,0x00,0xe6,0x00,0xea,0x00,0xee,0x00
0,0xf2,0x00,0xf6,0x00,0xfa,0x00,0xfe,0x00
0,0x02,0x01 ; Data 42 - 62
.db
0x06,0x01,0x0a,0x01,0x0e,0x01,0x12,0x01
,0x16,0x01,0x1a,0x01,0x1e,0x01,0x22,0x01
1,0x26,0x01,0x2a,0x01,0x2e,0x01,0x32,0x01
1,0x36,0x01,0x3a,0x01,0x3e,0x01,0x42,0x01
1,0x46,0x01,0x4a,0x01,0x4e,0x01,0x52,0x01
1,0x56,0x01 ; Data 63 - 83
.db
0x5a,0x01,0x5e,0x01,0x62,0x01,0x66,0x01
,0x6a,0x01,0x6e,0x01,0x72,0x01,0x76,0x01

```

1, 0x7a, 0x01, 0x7e, 0x01, 0x82, 0x01, 0x86, 0x01, 0x8a, 0x01, 0x8e, 0x01, 0x92, 0x01, 0x96, 0x01, 0x9a, 0x01, 0x9e, 0x01, 0xa2, 0x01, 0xa6, 0x01, 0xaa, 0x01 ; Data 84 - 104
.db
0xae, 0x01, 0xb2, 0x01, 0xb6, 0x01, 0xba, 0x01, 0xbe, 0x01, 0xc2, 0x01, 0xc6, 0x01, 0xca, 0x01, 0xce, 0x01, 0xd2, 0x01, 0xd6, 0x01, 0xda, 0x01, 0xde, 0x01, 0xe2, 0x01, 0xe6, 0x01, 0xea, 0x01, 0xee, 0x01, 0xf2, 0x01, 0xf6, 0x01, 0xfa, 0x01, 0xfe, 0x01 ; Data 105 - 125
.db
0x02, 0x02, 0x06, 0x02, 0x0a, 0x02, 0x0e, 0x02, 0x12, 0x02, 0x16, 0x02, 0x1a, 0x02, 0x1e, 0x02, 0x22, 0x02, 0x26, 0x02, 0x2a, 0x02, 0x2e, 0x02, 0x32, 0x02, 0x36, 0x02, 0x3a, 0x02, 0x3e, 0x02, 0x42, 0x02, 0x46, 0x02, 0x4a, 0x02, 0x4e, 0x02, 0x52, 0x02 ; Data 126 - 146
.db
0x56, 0x02, 0x5a, 0x02, 0x5e, 0x02, 0x62, 0x02, 0x66, 0x02, 0x6a, 0x02, 0x6e, 0x02, 0x72, 0x02, 0x76, 0x02, 0x7a, 0x02, 0x7e, 0x02, 0x82, 0x02, 0x86, 0x02, 0x8a, 0x02, 0x8e, 0x02, 0x92, 0x02, 0x96, 0x02, 0x9a, 0x02, 0x9e, 0x02, 0xa2, 0x02, 0xa6, 0x02 ; Data 147 - 167
.db
0xaa, 0x02, 0xae, 0x02, 0xb2, 0x02, 0xb6, 0x02, 0xba, 0x02, 0xbe, 0x02, 0xc2, 0x02, 0xc6, 0x02, 0xca, 0x02, 0xce, 0x02, 0xd2, 0x02, 0xd6, 0x02, 0xda, 0x02, 0xde, 0x02, 0xe2, 0x02, 0xe6, 0x02, 0xea, 0x02, 0xee, 0x02, 0xf2, 0x02, 0xf6, 0x02, 0xfa, 0x02 ; Data 168 - 188
.db
0xfe, 0x02, 0x02, 0x03, 0x06, 0x03, 0x0a, 0x03, 0x0e, 0x03, 0x12, 0x03, 0x16, 0x03, 0x1a, 0x03, 0x1e, 0x03, 0x22, 0x03, 0x26, 0x03, 0x2a, 0x03, 0x2e, 0x03, 0x32, 0x03, 0x36, 0x03, 0x3a, 0x03, 0x3e, 0x03, 0x42, 0x03, 0x46, 0x03, 0x4a, 0x03, 0x4e, 0x03 ; Data 189 - 209
.db
0x52, 0x03, 0x56, 0x03, 0x5a, 0x03, 0x5e, 0x03, 0x62, 0x03, 0x66, 0x03, 0x6a, 0x03, 0x6e, 0x03, 0x72, 0x03, 0x76, 0x03, 0x7a, 0x03, 0x7e, 0x03, 0x82, 0x03, 0x86, 0x03, 0x8a, 0x03, 0x8e, 0x03, 0x92, 0x03, 0x96, 0x03, 0x9a, 0x03, 0x9e, 0x03, 0xa2, 0x03 ; Data 210 - 230
.db
0xa6, 0x03, 0xaa, 0x03, 0xae, 0x03, 0xb2, 0x03, 0xb6, 0x03, 0xba, 0x03, 0xbe, 0x03, 0xc2, 0x03, 0xc6, 0x03, 0xca, 0x03, 0xce, 0x03, 0xd2, 0x03, 0xd6, 0x03, 0xda, 0x03, 0xde, 0x03, 0xe2, 0x03, 0xe6, 0x03, 0xea, 0x03, 0xee, 0x03, 0xf2, 0x03, 0xf6, 0x03 ; Data 231 - 251
.db
0xfa, 0x03, 0xfe, 0x03, 0x02, 0x04, 0x06, 0x04, 0x0a, 0x04, 0x0e, 0x04, 0x12, 0x04, 0x16, 0x04, 0x1a, 0x04, 0x1e, 0x04, 0x22, 0x04, 0x26, 0x04, 0x2a, 0x04, 0x2e, 0x04, 0x32, 0x04, 0x36, 0x04, 0x3a, 0x04, 0x3e, 0x04, 0x42, 0x04, 0x46, 0x04, 0x4a, 0x04 ; Data 252 - 272
.db
0x4e, 0x04, 0x52, 0x04, 0x56, 0x04, 0x5a, 0x04, 0x5e, 0x04, 0x62, 0x04, 0x66, 0x04, 0x6a, 0x04, 0x6e, 0x04, 0x72, 0x04, 0x76, 0x04, 0x7a, 0x04, 0x7e, 0x04, 0x82, 0x04, 0x86, 0x04, 0x8a, 0x04, 0x8e, 0x04, 0x92, 0x04, 0x96, 0x04, 0x9a, 0x04, 0x9e, 0x04 ; Data 273 - 293
.db
0xa2, 0x04, 0xa6, 0x04, 0xaa, 0x04, 0xae, 0x04, 0xb2, 0x04, 0xb6, 0x04, 0xba, 0x04, 0xbe, 0x04, 0xc2, 0x04, 0xc6, 0x04, 0xca, 0x04, 0xce, 0x04, 0xd2, 0x04, 0xd6, 0x04, 0xda, 0x04, 0xde, 0x04, 0xe2, 0x04, 0xe6, 0x04, 0xea, 0x04, 0xee, 0x04, 0xf2, 0x04 ; Data 294 - 314
.db
0xf6, 0x04, 0xfa, 0x04, 0xfe, 0x04, 0x02, 0x05, 0x06, 0x05, 0x0a, 0x05, 0x0e, 0x05, 0x12, 0x05,

5, 0x16, 0x05, 0x1a, 0x05, 0x1e, 0x05, 0x22, 0x05, 0x26, 0x05, 0x2a, 0x05, 0x2e, 0x05, 0x32, 0x05, 0x36, 0x05, 0x3a, 0x05, 0x3e, 0x05, 0x42, 0x05, 0x46, 0x05 ; Data 315 - 335
.db
0x4a, 0x05, 0x4e, 0x05, 0x52, 0x05, 0x56, 0x05, 0x5a, 0x05, 0x5e, 0x05, 0x62, 0x05, 0x66, 0x05, 0x6a, 0x05, 0x6e, 0x05, 0x72, 0x05, 0x76, 0x05, 0x7a, 0x05, 0x7e, 0x05, 0x82, 0x05, 0x86, 0x05, 0x8a, 0x05, 0x8e, 0x05, 0x92, 0x05, 0x96, 0x05, 0x9a, 0x05 ; Data 336 - 356
.db
0x9e, 0x05, 0xa2, 0x05, 0xa6, 0x05, 0xaa, 0x05, 0xae, 0x05, 0xb2, 0x05, 0xb6, 0x05, 0xba, 0x05, 0xbe, 0x05, 0xc2, 0x05, 0xc6, 0x05, 0xca, 0x05, 0xce, 0x05, 0xd2, 0x05, 0xd6, 0x05, 0xda, 0x05, 0xde, 0x05, 0xe2, 0x05, 0xe6, 0x05, 0xea, 0x05, 0xee, 0x05 ; Data 357 - 377
.db
0xf2, 0x05, 0xf6, 0x05, 0xfa, 0x05, 0xfe, 0x05, 0x02, 0x06, 0x06, 0x06, 0x0a, 0x06, 0x0e, 0x06, 0x12, 0x06, 0x16, 0x06, 0x1a, 0x06, 0x1e, 0x06, 0x22, 0x06, 0x26, 0x06, 0x2a, 0x06, 0x2e, 0x06, 0x32, 0x06, 0x36, 0x06, 0x3a, 0x06, 0x3e, 0x06, 0x42, 0x06 ; Data 378 - 398
.db
0x46, 0x06, 0x4a, 0x06, 0x4e, 0x06, 0x52, 0x06, 0x56, 0x06, 0x5a, 0x06, 0x5e, 0x06, 0x62, 0x06, 0x66, 0x06, 0x6a, 0x06, 0x6e, 0x06, 0x72, 0x06, 0x76, 0x06, 0x7a, 0x06, 0x7e, 0x06, 0x82, 0x06, 0x86, 0x06, 0x8a, 0x06, 0x8e, 0x06, 0x92, 0x06, 0x96, 0x06 ; Data 399 - 419
.db
0x9a, 0x06, 0x9e, 0x06, 0xa2, 0x06, 0xa6, 0x06, 0xaa, 0x06, 0xae, 0x06, 0xb2, 0x06, 0xb6, 0x06, 0xba, 0x06, 0xbe, 0x06, 0xc2, 0x06, 0xc6, 0x06, 0xca, 0x06, 0xce, 0x06, 0xd2, 0x06, 0xd6, 0x06, 0xda, 0x06, 0xde, 0x06, 0xe2, 0x06, 0xe6, 0x06, 0xea, 0x06 ; Data 420 - 440
.db
0xee, 0x06, 0xf2, 0x06, 0xf6, 0x06, 0xfa, 0x06, 0xfe, 0x06, 0x02, 0x07, 0x06, 0x07, 0x0a, 0x07, 0x0e, 0x07, 0x12, 0x07, 0x16, 0x07, 0x1a, 0x07, 0x1e, 0x07, 0x22, 0x07, 0x26, 0x07, 0x2a, 0x07, 0x2e, 0x07, 0x32, 0x07, 0x36, 0x07, 0x3a, 0x07, 0x3e, 0x07 ; Data 441 - 461
.db
0x42, 0x07, 0x46, 0x07, 0x4a, 0x07, 0x4e, 0x07, 0x52, 0x07, 0x56, 0x07, 0x5a, 0x07, 0x5e, 0x07, 0x62, 0x07, 0x66, 0x07, 0x6a, 0x07, 0x6e, 0x07, 0x72, 0x07, 0x76, 0x07, 0x7a, 0x07, 0x7e, 0x07, 0x82, 0x07, 0x86, 0x07, 0x8a, 0x07, 0x8e, 0x07, 0x92, 0x07 ; Data 462 - 482
.db
0x96, 0x07, 0x9a, 0x07, 0x9e, 0x07, 0xa2, 0x07, 0xa6, 0x07, 0xaa, 0x07, 0xae, 0x07, 0xb2, 0x07, 0xb6, 0x07, 0xba, 0x07, 0xbe, 0x07, 0xc2, 0x07, 0xc6, 0x07, 0xca, 0x07, 0xce, 0x07, 0xd2, 0x07, 0xd6, 0x07, 0xda, 0x07, 0xde, 0x07, 0xe2, 0x07, 0xe6, 0x07 ; Data 483 - 503
.db
0xea, 0x07, 0xee, 0x07, 0xf2, 0x07, 0xf6, 0x07, 0xfa, 0x07, 0xfe, 0x07, 0x02, 0x08, 0x06, 0x08, 0x0a, 0x08, 0x0e, 0x08, 0x12, 0x08, 0x16, 0x08, 0x1a, 0x08, 0x1e, 0x08, 0x22, 0x08, 0x26, 0x08, 0x2a, 0x08, 0x2e, 0x08, 0x32, 0x08, 0x36, 0x08, 0x3a, 0x08 ; Data 504 - 524
.db
0x3e, 0x08, 0x42, 0x08, 0x46, 0x08, 0x4a, 0x08, 0x4e, 0x08, 0x52, 0x08, 0x56, 0x08, 0x5a, 0x08, 0x5e, 0x08, 0x62, 0x08, 0x66, 0x08, 0x6a, 0x08, 0x6e, 0x08, 0x72, 0x08, 0x76, 0x08, 0x7a, 0x08, 0x7e, 0x08, 0x82, 0x08, 0x86, 0x08, 0x8a, 0x08, 0x8e, 0x08 ; Data 525 - 545
.db
0x92, 0x08, 0x96, 0x08, 0x9a, 0x08, 0x9e, 0x08, 0xa2, 0x08, 0xa6, 0x08, 0xaa, 0x08, 0xae, 0x08,

Appendix B

```
//-----
#include <vcl.h>
#pragma hdrstop
//-----
USEFORM("GetNameFrm.cpp",
GetNameForm);
USEFORM("KeyboardForm.cpp", KeyboardFrm);
USEFORM("MainUnit.cpp", mainform);
USEFORM("Unit1.cpp", Form1);
USEFORM("Unit2.cpp", Form2);
USEFORM("Unit4.cpp", Form4);
USEFORM("Unit3.cpp", Form3);
USEFORM("Unit6.cpp", Form6);
USEFORM("Unit7.cpp", Form7);
USEFORM("Unit8.cpp", Form8);
USEFORM("VideoPlayerUnit.cpp", FormVp);
USEFORM("Unit9.cpp", Form9);
USEFORM("Unit10.cpp", Form10);
USEFORM("Unit11.cpp", Form11);
//-----
WINAPI WinMain(HINSTANCE, HINSTANCE,
LPSTR, int)
{
    try
    {
        Application->Initialize();
        Application-
>CreateForm(__classid(Tmainform),
&mainform);
        Application->Run();
    }
    catch (Exception &exception)
    {
        Application-
>ShowException(&exception);
    }
    catch (...)
    {
        try
        {
            throw
Exception("");
        }
        catch (Exception
&exception)
        {
            Application-
>ShowException(&exception);
        }
    }
    return 0;
}
//-----
```

```
//-----
#include <vcl.h>
#pragma hdrstop
#include "GetNameFrm.h"
//-----
#pragma package(smart_init)
#pragma link "PI_MultiMask"
#pragma resource "*.dfm"
TGetNameForm *GetNameForm;
//-----
AnsiString __fastcall RemoveSpaces(char *fg)
{
    int i=0;
    int j=0;
    AnsiString ret;
    char buf[300];
    while (fg[i]!=0) {
        if (fg[i]!=' ') buf[j++]=fg[i];
        i++;
    }
    buf[j]=0;
    ret=buf;
    return(ret);
}
__fastcall
TGetNameForm::TGetNameForm(TComponent
t* Owner)
    : TForm(Owner)
{
    forms=0;
    TSL=new TStringList;
    TSL->Sorted=true;
    int fd=FileOpen(DataFile,fmOpenRead);
    AnsiString cc;
    if (fd>=0) {
        int x,i,j=FileSeek(fd,0,2);
        j/=sizeof(pi_folderInfo);
        FileSeek(fd,0,0);
        pi_folderInfo pp;
        for (i = 0; i <j; i++) {
            FileSeek(fd,(int)(i*sizeof(pi_folderInfo)),0);
            FileRead(fd,&pp,sizeof(pi_folderInfo));
            cc=RemoveSpaces(pp.fName);
            cc+=" ";
            cc+=i;
            TSL->Add(cc);
        }
        for (i = 0; i <j; i++) {
            cc=TSL->ValueFromIndex[i];
            x=cc.ToInt();
        }
    }
}
```

```

FileSeek(fd,(int)(x*sizeof(pi_folderInfo)),0);

FileRead(fd,&pp,sizeof(pi_folderInfo));
    x=LB1->Items->Add(pp.fName);
    SendMessage(LB1-
>Handle,LB_SETITEMDATA,x,i);
    }
    FileClose(fd);
}
}
__fastcall TGetNameForm::~TGetNameForm()
{
    delete TSL;
}
//-----
void __fastcall
TGetNameForm::PrepareForm(int
id,pi_folderInfo *folder)
{
    Id=id;
    fFolder=folder;
    if (id==-10) {
        Panel1->Visible=false;
        LB1->Align=alClient;
        Caption="Please      Select
Folder";
        return;
    }
    forms=1;
    if (Id<0) {
        pi1->MText="";
    }
    else {
        pi1->MText=fFolder->fName;
    }
}
int __fastcall TGetNameForm::GetSelection()
{
    if (Panel1->Visible) {
        return(Id);
    }
    int i=LB1->ItemIndex;
    int      x=SendMessage(LB1-
>Handle,LB_GETITEMDATA,i,0);
    AnsiString cc=TSL->ValueFromIndex[x];
    i=cc.ToInt();
    return(i);
}
void __fastcall
TGetNameForm::BitBtn1Click(TObject
*Sender)
{
    if (!Panel1->Visible) {
        int i=LB1->ItemIndex;
        if (i<0) {
            LB1->SetFocus();
                return;
            }
        i=GetSelection();
        if (i<0) {
            LB1->SetFocus();
            return;
        }
        int
fd=FileOpen(DataFile,fmOpenReadWrite);
        if (fd>=0) {
            FileSeek(fd,(int)(i*sizeof(pi_folderInfo)),0);
            FileRead(fd,fFolder,sizeof(pi_folderInfo));
            FileClose(fd);
        }
        ModalResult=mrOk;
        return;
    }
    AnsiString cc=pi1->MText;
    if (cc.IsEmpty()) {
        pi1->SetFocus();
        return;
    }
    cc=RemoveSpaces(cc.c_str());
    int x,i=TSL->IndexOfName(cc);
    if (i>=0) {
        if (Id<0) {
            LB1->ItemIndex=i;
            pi1->SetFocus();
            return;
        }
        cc=TSL->ValueFromIndex[i];
        x=cc.ToInt();
        if (x!=Id) {
            LB1->ItemIndex=i;
            pi1->SetFocus();
            return;
        }
    }
    int fd=FileOpen(DataFile,fmOpenReadWrite);
    if (fd<0) fd=FileCreate(DataFile);
    if (Id>=0) {
        FileSeek(fd,(int)(Id*sizeof(pi_folderIn
fo)),0);
        FileRead(fd,fFolder,sizeof(pi_folderIn
fo));
    }
    else {
        Id=FileSeek(fd,0,2);
        Id/=sizeof(pi_folderInfo);
        fFolder->NumOfDynamic=0;
        fFolder->NumOfKinetics=0;
        fFolder->NumOfVideos=0;
        fFolder->id=Id;
        fFolder->creationdate=Date()+Time();
    }
}

```

```

strcpy(fFolder->fPrevName,fFolder->fName);
strcpy(fFolder->fName,pi1->MText.c_str());
fFolder->modifydate=Date()+Time();
FileSeek(fd,(int)(ld*sizeof(pi_folderInfo)),0);
FileWrite(fd,fFolder,sizeof(pi_folderInfo));
FileClose(fd);
ModalResult=mrOk;
}
//-----
void __fastcall
TGetNameForm::FormShow(TObject *Sender)
{
if (forms==1) {
Left=MainMonitorLeft;
Top=MainMonitorTop;
}
else {
Top=MainMonitorTop;
}
}
//-----
void __fastcall
TGetNameForm::LB1DbClick(TObject
*Sender)
{
if (!Panel1->Visible) {
BitBtn1Click(BitBtn1);
}
}
//-----
void __fastcall
TGetNameForm::pi1Enter(TObject *Sender)
{
TPoint pt;
pt.x=Panel1->Left;
pt.y=Top+Height;//Panel1->Height;
pt=ClientToScreen(pt);
ShowKeyboard(this,0,pt.y,"");
}
//-----
void __fastcall
TGetNameForm::pi1Exit(TObject *Sender)
{
HideKeyboard();
}
//-----
void __fastcall
TGetNameForm::FormClose(TObject *Sender,
TCloseAction &Action)
{
HideKeyboard();
}
//-----
void __fastcall
TGetNameForm::Panel2Resize(TObject
*Sender)
{
int w=(Panel2->ClientWidth-(BitBtn1-
>Width*2)-20)/2;
BitBtn1->Left=w;
w+=20+BitBtn1->Width;
BitBtn2->Left=w;
}
//-----
void __fastcall
TGetNameForm::Panel4Click(TObject
*Sender)
{
if (!Panel1->Visible) {
int i=LB1->ItemIndex;
i++;
LB1->ItemIndex=i;
}
}
//-----
void __fastcall
TGetNameForm::Panel3Click(TObject
*Sender)
{
if (!Panel1->Visible) {
int i=LB1->ItemIndex;
i--;
if (i<0) i=0;
LB1->ItemIndex=i;
}
}
//-----
//-----
#include <vcl.h>
#pragma hdrstop
#include "MainUnit.h"
#include "RegistrationDllInterface.h"
#include "Unit10.h"
#include "Unit11.h"
#include "Unit1.h"
#include "Unit6.h"
#include "vars.h"
//-----
#pragma package(smart_init)
#pragma link "PI_GIECamera"
#pragma link "PI_Serial"
#pragma link "VrControls"
#pragma link "VrSlider"
#pragma link "VrRotarySwitch"
#pragma link "PI_WinXP"
#pragma resource "*.dfm"
Tmainform *mainform;
//-----
AnsiString IniFileName;
AnsiString DeviceDataFileName;
AnsiString DataFile;
AnsiString DynamicDataFile;

```

```

AnsiString TmpFile;
bool has_registration;
__fastcall
Tmainform::Tmainform(TComponent* Owner)
    : TForm(Owner)
{
    come_buffer=new char[1000];
    come_buffer_pos=0;
    Label3->Caption="Disconnected";
    Label4->Caption="Uknown";
    IniFileName=ChangeFileExt(Application-
>ExeName, ".ini");

    DeviceDataFileName=ChangeFileExt(Applicati
on->ExeName, ".dat");
    DataFile=ExtractFilePath(Application-
>ExeName)+"Endoscope_data.dat";

    DynamicDataFile=ExtractFilePath(Application-
>ExeName)+"Dynamic_data.dat";
    TmpFile=ExtractFilePath(Application-
>ExeName)+"tmp_image.bmp";
    theCamera->IniName=IniFileName;
    theCamera->IniSection="Camera";
    theCamera-
>DefaultPropertiesFileName=ChangeFileExt(A
pplication->ExeName, ".pro");
    CamerasCount=0;
    has_registration=InitRegistrationDll();
    BitBtn1->Visible=true;
    BitBtn1->Enabled=(CamerasCount>0);
    theCamera->init();
    StartSerial();
    OnSerialRead=mOnSerialRead;
    TimerToStart->Tag=0;
}
//-----
void __fastcall
Tmainform::theCameraCameraAdded(TObject
*Sender)
{
    CamerasCount++;
    if (CamerasCount>0) {
        TimerToStart->Enabled=true;
        BitBtn1->Enabled=true;
    }
}
//-----
void __fastcall
Tmainform::theCameraCameraRemoved(TObj
ect *Sender)
{
    CamerasCount--;
    if (CamerasCount<0) CamerasCount=0;
    if (CamerasCount==0) {
        if (Form1!=0) {
            Form1->Close();
        }
        TimerToStart->Enabled=false;
        BitBtn1->Enabled=false;
    }
}
//-----
void __fastcall
Tmainform::WndProc(TMessage &msg)
{
    if (msg.Msg==(WM_USER+1000)) {
        msg.Result=(int)theCamera;
    }
    else if (msg.Msg==(WM_USER+1001)) {
        msg.Result=(int)PIS;
    }
    else if (msg.Msg==(WM_USER+1002)) {
        OnSerialRead=mOnSerialRead;
        Close();
    }
    else if (msg.Msg==(WM_USER+1003)) {
        StartSerial();
    }
    else if (msg.Msg==(WM_USER+1004)) {
        char *buf=(char *)msg.LParam;
        strcpy(buf,Label4->Caption.c_str());
    }
    else if (msg.Msg==(WM_USER+1005)) {
        char *buf=(char *)msg.LParam;
        SendString(buf);
    }
    else TForm::WndProc(msg);
}
void __fastcall
Tmainform::BitBtn1Click(TObject *Sender)
{
    if (PIS-
>SerialHandle!=INVALID_HANDLE_VALUE){
        if (Form1!=0) {
            Form1->Close();
        }
        Form1=new TForm1(this);
        Form1->Show();
        OnSerialRead=Form1-
>aOnSerialRead;
        /*
        AnsiString cca="aF0\0a";
        SendString(cca);
        */
        Form1->BitBtn15->Click();
        //
        AnsiString cc="31\0a";
        //
        SendString(cc);
        Visible=false;
    }
}
//-----

```

```

void __fastcall
Tmainform::TimerToStartTimer(TObject
*Sender)
{
    if (TimerToStart->Tag==0) return;

    TimerToStart->Enabled=false;
    BitBtn1Click(BitBtn1);
}
//-----
void __fastcall Tmainform::StartSerial()
{
    int bd,bi,sb,pa;
    AnsiString dev;
    DeviceConnected=false;
    DevVersion="";
    TIniFile *mini=new TIniFile(IniFileName);
    bd=mini->ReadInteger("SERIAL","BAUD",8);
    bi=mini->ReadInteger("SERIAL","BITS",3);
    sb=mini->ReadInteger("SERIAL","STOP",0);
    pa=mini->ReadInteger("SERIAL","PARITY",0);
    dev=mini->ReadString("SERIAL","DEVICE","");
    delete mini;
    if (dev.IsEmpty()) {
        return;
    }
    PIS->DCBXoffChar=0;
    PIS->DCBXonChar=0;
    PIS->DCBXoffLim=0;
    PIS->DCBXonLim=0;
    PIS->DCBfInX=FALSE;
    PIS->DCBfOutX=FALSE;
    PIS->DCBfOutxCtsFlow=FALSE;
    PIS->DCBfOutxDsrFlow=FALSE;
    PIS-
>DCBDtrControl=(cpDTRFlowControl)DTR_CO
NTROL_ENABLE;
    PIS-
>DCBRtsControl=(cpRTSFlowControl)RTS_CON
TROL_ENABLE;
    bool bb=false;
    PIS->ComPort=(cmComPorts)1;
    PIS->UseDevPath=dev;
    PIS->Parity=(cpComParity)pa;
    PIS->Bits=(cbComBits)bi;
    PIS->StopBits=(csComStopBits)sb;
    PIS->Baud=(crComBaud)bd;
    // PIS->IsOverlapped=false;
    int a=PIS->Connect();
    if (a!=0) bb=false;
    else bb=true;
    if (bb) {
        Label3->Caption=PIS->ConText;
        BitBtn3Click(BitBtn3);
    }
    else {

```

```

        Label3->Caption=PIS-
>ConText+AnsiString("\r\n")+PIS->ErrorText;
    }
}
void __fastcall
Tmainform::BitBtn2Click(TObject *Sender)
{
    if (PIS-
>SerialHandle!=INVALID_HANDLE_VALUE) {
        PIS->Disconnect();
        Label3->Caption="Disconnected";
        Label4->Caption="Uknown";
    }
    TForm6 *ff=new TForm6(this);
    ff->ShowModal();
    delete ff;
    StartSerial();
}
//-----
void __fastcall Tmainform::PISRead(TObject
*Sender, int bytes, char *rxBuffer)
{
    int i;
    AnsiString cc;
    int x=bytes ;
    for (i = 0; i <bytes; i++) {
        if (rxBuffer[i]==2) {
            if (come_buffer_pos>0) if
(FOnSerialRead!=0)
FOnSerialRead(PIS,come_buffer,come_buffer_
pos);
            come_buffer_pos=0;
        }
        else if (rxBuffer[i]==3 ||
rxBuffer[i]=='\r' || rxBuffer[i]=='\n') {
            if (come_buffer_pos>0) {
                if (come_buffer[0]=='V' &&
come_buffer[1]=='E') {
                    DeviceConnected=true;
                    DevVersion=come_buffer+2;
                    Label4-
>Caption=DevVersion;
                    TimerToStart-
>Tag++;
                    BitBtn3->Tag=0;
                }
            }
            else if (come_buffer[0]=='g'
&& come_buffer[1]=='t') {
                int
                AnsiString
                AnsiString
                c1="0x"+cc.SubString(1,4);
                int pos;

```



```

        z++;
        if (z==10) {
            z=0;
            Sleep(5);
        }
    }
}
//-----
void __fastcall
Tmainform::BitBtn4Click(TObject *Sender)
{
    StartSerial();
}
//-----
void __fastcall
Tmainform::Timer1Timer(TObject *Sender)
{
    Timer1->Enabled=false;
    if (BitBtn3->Tag==2) {
        return;
    }
}

```

```

    }
    BitBtn3Click(BitBtn3);
}
//-----
void __fastcall
Tmainform::BitBtn33Click(TObject *Sender)
{
    TForm10 *ff=new TForm10(this);
    ff->ShowModal();
    delete ff;
}
//-----
void __fastcall
Tmainform::BitBtn34Click(TObject *Sender)
{
    TForm11 *ff=new TForm11(this);
    ff->ShowModal();
    delete ff;
}
//-----

```